UNIVERSITAT POLITÈCNICA DE CATALUNYA
BARCELONATECH
Escola d'Enginyeria de Barcelona Est

amase
Advanced Materials Science and Engineering

MASTER THESIS

Advanced Materials Science and Engineering (AMASE)

COMBINATION OF SUPERELASTICITY AND SHAPE MEMORY ACTUATION IN A BISTABLE SHUTTER FOR VENUS EXPLORATION



Report and Appendices

Author: Lluc Rodó de Yebra
Supervisor: Dr. Antonio M. Mateo
Department Materials Science and Engineering
Company tutor: Gisbert Peter

Call: 2026, June

Acknowledgements

I firstly want to thank the German Aerospace Center, more specifically my supervisor, Gisbert Peter, for his trust in giving me this oppotunity, and my mentor, Patrick Dern, for his day-to-day technical guidance and valuable assistance throughout the project.

Secondly, I want to thank the Universitat Politècnica de Catalunya for making this stay abroad possible and straightforward. Thank you to my supervisor, Dr. Antonio M. Mateo, for accepting the supervision of this work and for providing me with practical feedback and useful advice.

My appreciation also goes to the friends I made during this master's program, with whom I share many great memories from Barcelona and Padova, and who made this journey more enjoyable.

Last but not least, I want to thank those who have always been with me and are inspiration to me every day. To my mom and my dad, for their unconditional care and affection. To my sister Aina, for her constant determination. To my brother Pau, for his extraordinary resilience, positivity, and strength of will. And to Antonia, for her happinness, warmth, and for being there through it all.

Abstract

Optical instruments on planetary missions require shielding mechanisms able to withstand corrosive, high-temperature atmospheres while remaining compact, reliable, and energy-efficient. The Venus Emissivity Mapper (VEM), aboard NASA's VERITAS and ESA's EnVision orbiters, is a spectrometer currently relying on a one-shot spring-loaded shutter that cannot reclose after firing, risking premature optics exposure and reducing mission control.

This thesis presents the design, optimization, and validation of a bidirectional, passively locking shutter actuated by shape memory alloys (SMAs). A structured ruled-chain design methodology was employed to systematically explore the design space, leading to the evaluation of three candidate concepts through a weighted decision matrix. The selected architecture combines a bistable mechanism with antagonistic SMA actuation, enabling bidirectional motion without countinuous power consumption.

Nonlinear finite element analyses were performed to compare Grade 5 titanium, a zirconium-based amorphous alloy, and superelastic nickel-titanium (NiTi) as candidate materials for the bistable flexures. The results demonstrate that the large recoverable strains provided by superelastic NiTi enable snap-through forces compatible with SMA actuation while remaining within its 8% recoverable strain limit, achieving displacements and safety factors unattainable with the alternative materials. PLA prototypes were subsequently used to validate the numerical model, with the refined simulations reproducing the force-displacement response within 5% deviation.

The resulting actuator satisfies the dimensional constraints of the VEM instrument while providing compact, bidirectional, and passively locking operation. Furthermore, this work demonstrates the feasibility of integrating superelastic bistable flexures with shape memory actuation into a unified actuator architecture, an approach that, to the best of our knowledge, has never been reported in the existing literature and offers a promising direction for future spaceborne smart-material mechanisms.

Resum

Els instruments òptics a bord de missions planetàries necessiten mecanismes de protecció capaços de resistir atmosferes corrosives i d'alta temperatura, mantenint-se alhora compactes, fiables i eficients energèticament. El *Venus Emissivity Mapper*, a bord dels orbitadors VERITAS (NASA) i EnVision (ESA), és un espectròmetre que actualment depèn d'un obturador d'un sol ús, accionat per molla, que no es pot tornar a tancar un cop actuat, fet que comporta el risc d'una exposició prematura de l'òptica i redueix el control de la missió.

Aquest Treball de Fi de Màster presenta el disseny, l'optimització i la validació d'un obturador bidireccional amb bloqueig passiu de posició, accionat mitjançant aliatges amb memòria de forma (*SMA*). Una metodologia estructurada, basada en el disseny en cadena, es va fer servir per explorar sistemàticament l'espai de disseny, la qual cosa va portar a l'avaluació de tres conceptes candidats mitjançant una matriu de decisió ponderada. L'arquitectura seleccionada combina un mecanisme biestable accionat per SMAs antagonistes, cosa que permet un moviment bidireccional sense consum continu d'energia.

Es van dur a terme anàlisis no lineals per elements finits per comparar titani Grau 5, un aliatge amorf a base de zirconi i níquel-titani (NiTi) superelàstic com a materials candidats per a les bigues biestables. Els resultats demostren que les grans deformacions reversibles proporcionades pel NiTi superelàstic permeten forces de transició entre posicions estables compatibles amb l'actuació de l'SMA, tot mantenint-se dins del seu límit de deformació reversible del 8% i aconseguint desplaçaments i factors de seguretat inassolibles amb els materials alternatius. Posteriorment, prototips de PLA van servir per validar el model numèric, i una versió refinada d'aquest va reproduir el comportament força-desplaçament amb una desviació inferior al 5%.

El disseny final de l'actuador s'ajusta a les restriccions dimensionals de l'instrument VEM, tot proporcionant un funcionament compacte, bidireccional i amb bloqueig de posició passiu. Aquest treball demostra la viabilitat d'integrar estructures biestables super-elàstiques actuades per l'efecte de memòria de forma en una arquitectura unificada, un enfocament que, segons el nostre coneixement, encara no s'ha reportat en la literatura existent i que ofereix una direcció prometedora per a futurs mecanismes espacials basats en materials intel·ligents.

Resumen

Los instrumentos ópticos a bordo de misiones planetarias requieren mecanismos de protección capaces de soportar atmósferas corrosivas y de alta temperatura sin dejar de ser compactos, fiables y eficientes desde el punto de vista energético. El *Venus Emissivity Mapper*, a bordo de los orbitadores VERITAS (NASA) y EnVision (ESA), es un espectrómetro que actualmente utiliza un obturador de un solo uso, accionado por resorte, que una vez activado no puede volver a cerrarse, lo que supone un riesgo de exposición óptica prematura y reduce el control de la misión.

Este Trabajo Final de Máster presenta el diseño, la optimización y la validación de un obturador bidireccional con bloqueo pasivo de posición, accionado por aleaciones con memoria de forma (SMA). Se utilizó una metodología estructurada, basada en el diseño en cadena, para explorar sistemáticamente el espacio de diseño, lo que condujo a la evaluación de tres conceptos candidatos mediante una matriz de decisión ponderada. La arquitectura seleccionada combina un mecanismo biestable accionado por aleaciones con memoria de forma (SMA) antagónicas, lo que permite un movimiento bidireccional sin un consumo continuo de energía.

Se llevaron a cabo análisis no lineales por elementos finitos para comparar titanio grado 5, una aleación amorfa a base de circonio y níquel-titanio (NiTi) superelástico como materiales candidatos para vigas biestables. Los resultados demuestran que las grandes deformaciones reversibles que proporciona el NiTi superelástico permiten fuerzas de transición entre posiciones estables compatibles con el accionamiento de la SMA, al tiempo que se mantiene dentro de su límite de deformación reversible del 8 % y obteniendo desplazamientos y factores de seguridad inalcanzables con los materiales alternativos. Posteriormente, se utilizaron prototipos de PLA para validar el modelo numérico, y una versión perfeccionada del mismo reprodujo el comportamiento fuerza-desplazamiento con una desviación inferior al 5 %.

El diseño final del actuador se ajusta a las restricciones dimensionales del instrumento VEM, al tiempo que proporciona un funcionamiento compacto y bidireccional con bloqueo de posición pasivo. Este trabajo demuestra la viabilidad de integrar estructuras superelásticas biestables accionadas por el efecto de memoria de forma en una arquitectura unificada, un enfoque que, según nuestro conocimiento, aún no se ha reportado en la literatura existente y que ofrece una dirección prometedora para futuros mecanismos espaciales basados en materiales inteligentes.

Table of contents

Chapter 1. Introduction **9**

1.1. Context, background and motivation 9

1.2. Approach plan and objectives 11

Chapter 2. State of the Art & Literature Review **13**

2.1. Shape Memory Materials (SMMs) 13

2.2. Shape Memory Effect (SME) 14

2.3. Superelasticity 16

2.4. Types of SMM and their applications 18

2.4.1. Shape Memory Alloys (SMAs) 18

2.4.2. Shape Memory Polymers (SMPs) 18

2.4.3. Shape Memory Ceramics (SMCs) 20

2.5. Types of bidirectional shape memory actuators 21

Chapter 3. Methodology **23**

3.1. Requirements and Constraints (RCs) 23

3.2. Design Rules (DRs) 24

3.3. Design Features (DFs) and candidate proposals 26

3.4. Evaluation and proposal selection 32

Chapter 4. Concept Development **35**

4.1. Compliant mechanisms and bistability 35

4.2. Early prototypes 37

4.3. Material candidates and selection 39

4.3.1. Material for the SMA 39

4.3.2. Material for the bistable mechanism 42

4.4. Finite element modelling of the bistable mechanism 45

4.4.1. Setup of the nonlinear numerical model 45

4.4.2 Material definition 47

4.4.3. Boundary conditions and loading 48

4.4.4. Design optimization criteria 48

Chapter 5. Results **51**

Chapter 6. Supplementary Design Proposal **65**

Chapter 7. Discussion and Conclusions **71**

Chapter 8. Ethical, Sustainable & Economical Analysis **75**

8.1. Sustainability and ethical considerations 75

8.2. Economic breakdown 76

Chapter 9. References **77**

Appendices **83**

Chapter 1.
Introduction

1.1. Context, background and motivation

In the framework of space exploration, efforts to find out more about the evolution of our sister planet Venus are being made. The similarity of Venus' physical characteristics with Earth's is the closest out of all other known planets, namely in size, mass, composition, and energy received from the Sun [40]. Previous missions to Venus, such as the Venus Express, were able to detect relevant amounts of water vapor in the lower atmosphere [41], leading to the thought of Venus' likely habitable past. However, the evolutionary paths of both celestial bodies diverged significantly; with Earth hosting abundant and diverse life, and Venus often being described as an inhospitable inferno [37]. The understanding of this drastic divergency in conditions and loss of life is the objective of NASA's "Venus Emissivity, Radio science, InSAR, Topography, And Spectroscopy" (VERITAS) and ESA's "EnVision" orbiter missions, which will scan and map the planet's surface to potentially help provide answers with the obtained scientific data.

To perform the observation of Venus, the Venus Emissivity Mapper (VEM), called VenSpec-M on EnVision, will be traveling onboard the VERITAS and EnVision orbiters. The VEM instrument is an infrared mapper designed and developed by the German Aerospace Center (DLR - Deutsches Zentrum für Luft- und Raumfahrt) at the Institute of Space Research, and it is a core scientific instrument for both missions [39]. It will have a surface coverage of over 70% of the planet and will be the first flight instrument allowing for global scale mapping of Venus [36].

The environmental conditions in which the materials constituting the aforementioned orbiters will be exposed to are significantly diverse than that of Earth. VERITAS and EnVision will use two phases of aerobraking (harnessing the atmosphere's drag to reduce the spacecraft's velocity) to lower the orbit into its final science setting [43]. This will involve direct exposure to Venus' extremely corrosive atmosphere, composed of a thick and dense layer of carbon dioxide (CO_2), nitrogen (N_2), and sulfuric acid clouds that contain caustic components such as sulfur dioxide (SO_2), hydrogen fluoride (HF), and hydrogen chloride (HCl) [20]. Additionally, spacecraft parts can fail due to the effects of atomic oxygen (AO), radiation (UV, cosmic rays, x-ray, particle-charged radiation), micrometeoroids and orbital debris, very high pressure (90 times Earth's), as well as extreme thermal cycling [20, 21]. This creates the need for having a shielding component that can protect the sensitive optics from the hostile external environment, especially during the periods of cruise, polar orbiting, and aerobraking, when the VEM is not in use. During science, the VEM's optics can be fully exposed to achieve maximum image resolution.

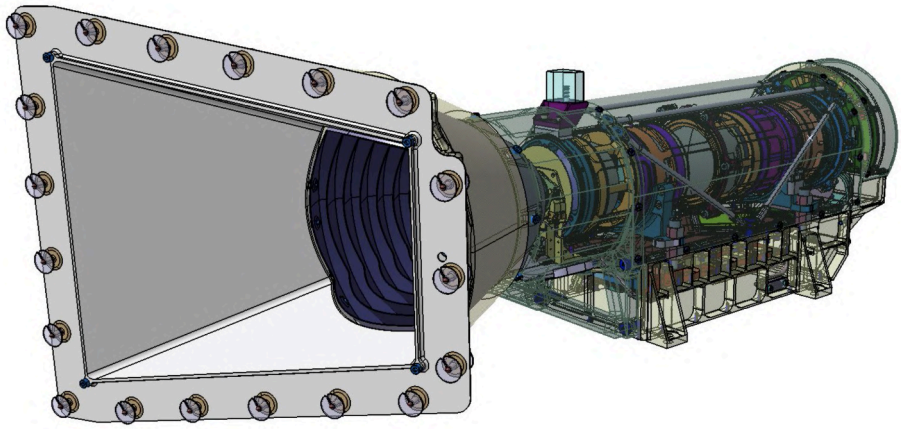


Fig. 1.1 | CAD model of the VEM instrument. Digital model of the Venus Emissivity Mapper, obtained from Hagelschuer et al. (2024).

To safeguard the optics, in accordance with what Hagelschuer et al. [36] report, the current design proposal of the VEM contains what is described as an optically transmissive turn window unit (TWU) made of fused silica, incorporating an antireflective (AR) coating optimized for the mission's operating bandwidth (NIR - Near Infrared). This highly transmissive window allows for scientific observation even when closed while withstanding environmental effects. Nevertheless, as significant degradation of the fused silica glass is still probable, to prevent visibility obstruction (and hence mission failure) a firing mechanism is incorporated to move the TWU out of the optical ray path. This mechanism is a one-shot, spring-loaded system that is based on the thermal knife principle.

Having an actuator performing a single-way motion has recently been identified as problematic, however, as sooner-than-expected degradation of the TWU could signify a premature exposure of the VEM optics to the environment, leading to a reduction in the

instrument's lifespan. Apart from improving protection, having bidirectional motion can allow for dark-frame calibration of the optics, obtaining cleaner images and eliminating the need for using a transmissive material, hence extending the range of material selection with the possibility to achieve slower degradation rates. Bidirectionality also gives more operation freedom and versatility, as the initial position can be regained on demand.

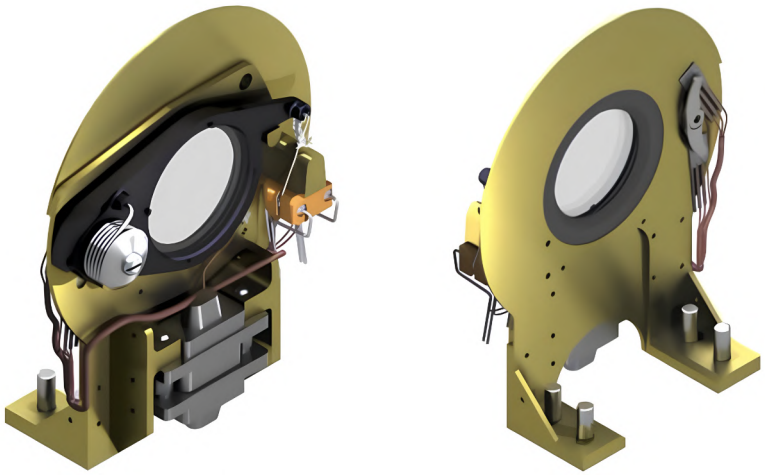


Fig. 1.2 | CAD model of the current TWU. Front (left) and rear (right) views of the Turn Window Unit, obtained from Hagelschuer et al. (2024).

The additional benefits offered by bidirectional actuation must nevertheless be balanced against the constraints imposed by spacecraft design, particularly the need for compactness, reliability, and minimal power consumption. This rules out conventional actuator systems that are motor-driven or incorporate complex transmission assemblies, often undesirable for spaceborne instrumentation, and motivate the exploration of alternative actuation principles. Among these, approaches that exploit unique material properties, such as the shape memory effect, have attracted increasing interest.

In this context, the present work investigates the applicability of shape memory materials for the actuation of a bidirectional window cover for the Venus Emissivity Mapper.

1.2. Approach plan and objectives

To have an organized and solid planning, this assignment will attempt to reach its objectives based on a ruled-chain design methodology adapted from the work of Yuan et al. [6]. The method begins by identifying Requirement Constraints (RCs), which are then reformulated as Design Rules (DRs). These rules represent constraints that can be

progressively combined or refined through inference or by restricting the set of possible choices when a specific design option is selected. Through this process, from the initial RCs a new and more specific set of constraints is obtained. The final step consists of the so-called embodiment phase, during which concrete Design Features (DFs) are proposed to satisfy the established constraints. By assembling the resulting DFs, a complete embodiment of the system can be defined. This methodology enables to explore the design space while maintaining a clear record of the design decisions and transformations applied during the process. As a result, the approach facilitates later modifications and helps identify where further exploration is required if no feasible solution is found.

The selection of a single design proposal will be carried out after assessing the three best candidates with an evaluation matrix. This assessment is performed based on engineering judgement, via a combination of personal intuition and academic knowledge, with the goal of obtaining a quantifiable justification of the choice made. The journey of this master thesis will then continue with the computational modeling of the selected candidate proposal, which will be sequentially optimized through the iteration of geometrical parameters and material properties in order to find the combination that gives the best results, i.e. that adapts the closest to the objective DFs. The validation of the computational model will represent the green light for physical prototyping. If, after testing, the tangible version of the design performs closely to the simulated variant, the proposal will be validated for use.

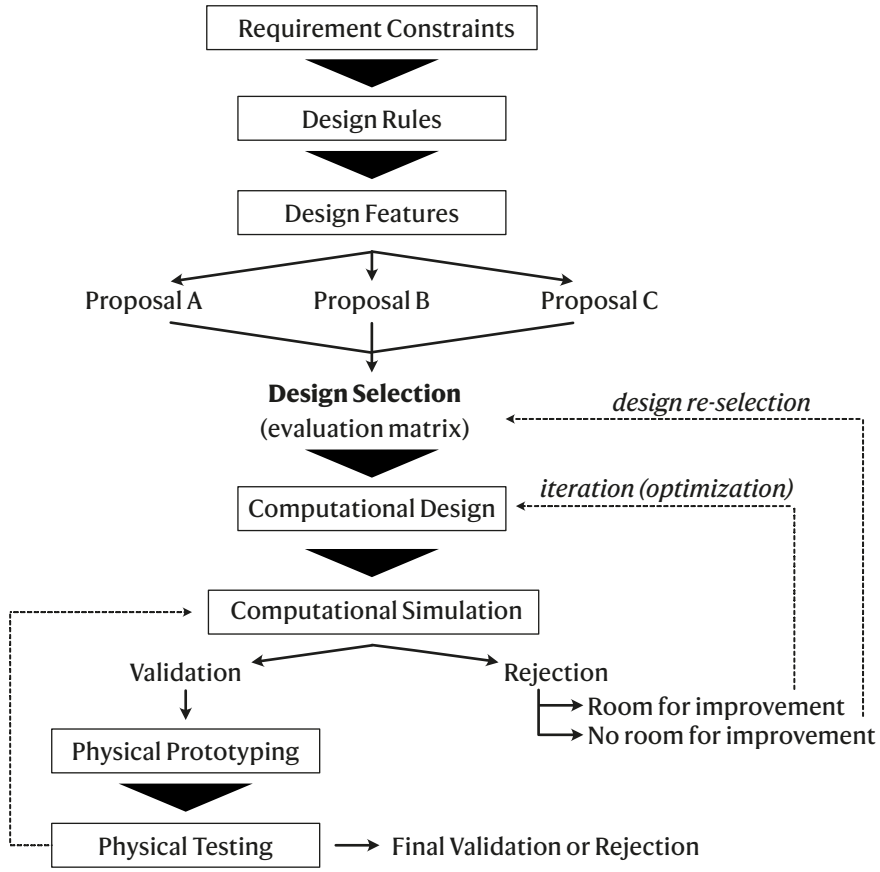


Fig. 1.3 | Approach map. Schematic of the planning and working path of this thesis.

Chapter 2.

State of the Art & Literature Review

2.1. Shape Memory Materials (SMMs)

Shape memory materials (SMMs) are a subclass of active [2] or "smart" [22] materials that can convert non-mechanical stimuli, most commonly temperature but also magnetic or electric fields, into large, recoverable mechanical strains via a reversible, diffusionless phase transformation [1]. In contrast to conventional materials, where functional properties are essentially passive, SMMs combine structural load-bearing capability with actuation, damping or sensing functions and thus belong to the broader family of multifunctional materials [1]. Depending on the material class and the nature of the driving field, SMMs exhibit one or both of two key phenomena: the shape memory effect (SME) and superelasticity (or pseudoelasticity) [1-19, 22-30].

At the microscopic level, the functional response of crystalline shape memory materials is governed by a thermoelastic martensitic transformation between a high-symmetry parent phase, known as austenite, and a low-symmetry martensite, which may occur thermally (SME) or stress-induced (superelasticity) [1, 16]. The transformation proceeds by shear-dominated lattice distortion without long-range diffusion [1], and is accompanied by large transformation strains of several percent up to more than 10% in some alloys and ceramics [22]. The martensitic phase typically forms in multiple crystallographic variants; under zero or low applied stress, these variants self-accommodate, leading to negligible macroscopic strain, whereas under external loading preferential variant selection (reorientation or "detwinning") produces large recoverable deformations that are observed macroscopically [16]. Depending on the process, these martensitic variants are respectively called "twinned" or "detwinned".

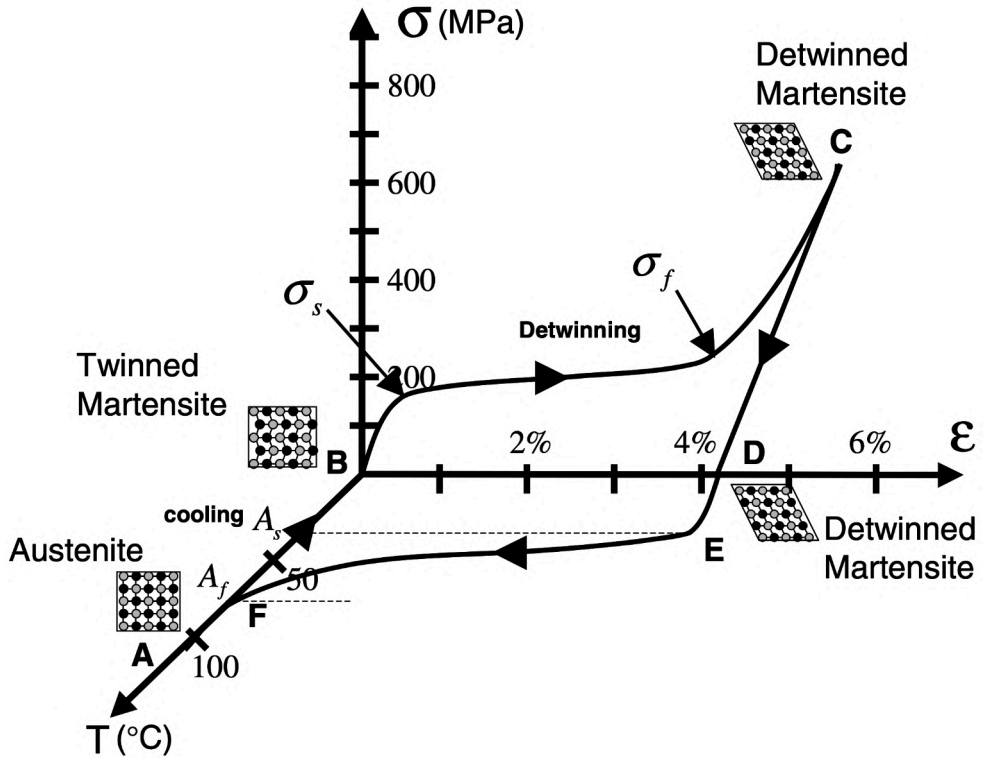


Fig. 2.1 | **Stress-strain-temperature diagram.** Phase transformation diagram of the shape memory effect typically exhibited by a shape memory alloy. [1]

From an applications standpoint, SMMs are attractive because they offer high specific work output compared to most active materials [2], simplified construction with solid-state operation and compatibility with Joule heating [16], and less risk of mechanical failure coupled with reduced weight due to the possibility of obtaining more compact assemblies [1].

SMMs can be broadly divided into three main classes: shape memory alloys (SMAs), shape memory polymers (SMPs), and shape memory ceramics (SMCs), each with distinct transformation mechanisms, property ranges, and application domains. The following sections first summarize the phenomenology of shape memory effect and superelasticity in SMAs, which are the most mature SMMs and the main focus of this work, and then review the different SMM classes and their applications, with emphasis on actuation and space-related uses.

2.2. Shape Memory Effect (SME)

The shape memory effect (SME) can present itself due to electrical, magnetic, or thermal exposure of the material [1]. The latter SME, which is this thesis' focus, denotes the ability of a material to recover a previously "memorized" shape upon heating after being

plastically deformed in a low-temperature state. For SMAs, the SME is based on the reversible austenite-martensite transformation and the reorientation of martensitic variants under stress.

A typical SME cycle in a nickel-titanium (NiTi) SMA can be described in a combined stress-strain-temperature space, as seen in Figure 2.1. This thermomechanical cycle is initiated at the austenitic state, at a temperature above the austenite finish temperature Af, where the material is fully austenitic and exhibits a relatively high Young's modulus EA. Upon cooling under negligible stress, austenite transforms to martensite between the martensite start Ms and martensite finish Mf temperatures. Multiple martensite variants form self-accommodated arrangements such that the macroscopic shape change is very small, oftentimes being referred to as twinned martensite [1, 15, 16].

When a mechanical load is applied at a temperature below M_f, martensitic variants reorient (or "detwin") once the stress exceeds the detwinning start stress σ_s, and detwinning saturates at the detwinning finish stress σ_f. This reorientation produces large and apparently plastic strains (typically up to 8% in NiTi [16]) at stress levels significantly lower than the conventional plastic yield stress.

After unloading, most of the macroscopic detwinning strain is retained, i.e. the deformed shape remains stable at low temperatures apart from small elastic recoveries. The cycle is completed upon subsequent heating above A_f, which triggers the reverse martensite-austenite transformation and the original ("trained") shape is recovered, leading to a macroscopic contraction under zero load. Cooling again below M_f re-forms twinned martensite without additional shape change, restarting the cycle and allowing for repetition.

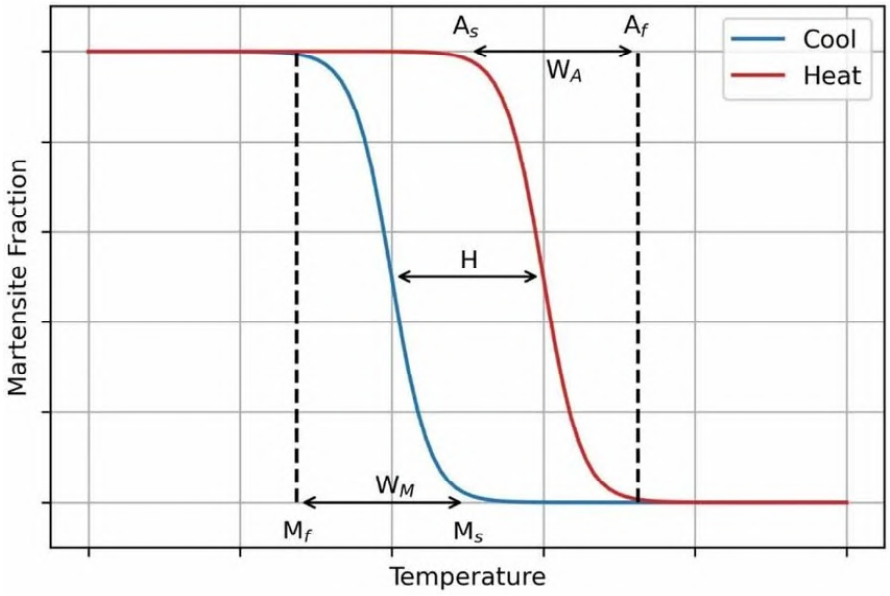


Fig. 2.2 | Hysteresis cycle of an ideal SMA. The path delay during a heating–cooling cycle can be observed. Hysteric behavior is indicated as H in the plot. [60]

This constitutes the classic one-way shape memory effect, where the material remembers only the high-temperature (austenitic) shape. The associated strain-temperature curve at constant stress exhibits a hysteresis loop [15]: during heating, transformation initiates at A_s and completes at A_f, while on cooling, transformation occurs between M_s and M_f.

In most commercial SMAs, the SME is intrinsically one-way. Two-way shape memory effect (TWSME) can be induced via thermomechanical training or constrained ageing such that the material exhibits two different shapes upon heating and cooling without externally applied bias forces [1, 2]. However, TWSME is generally less stable and offers smaller strain, and therefore many actuator designs rely instead on one-way SME combined with mechanical bias elements (springs, antagonistic SMAs, or external loads) to achieve bidirectional motion [1, 3, 9, 16].

From an engineering perspective, the SME enables thermally driven displacement under load, i.e. actuation, since transformation strain can be generated against substantial external stresses [16]. NiTi wire actuators, for instance, can provide up to ~5% recoverable SME strain at stresses on the order of 200-400 MPa [1], corresponding to actuation energy densities significantly higher than many electromagnetic or pneumatic actuators of similar scale [9].

2.3. Superelasticity

Superelasticity, also called pseudoelasticity [1], is the ability of a SMA to undergo large, reversible strains under purely mechanical loading-unloading cycles at a temperature above A_f, where the material is fully austenitic at zero stress. In this regime, a stress-induced martensitic transformation occurs during loading and reverts during unloading, resulting in a characteristic flag-shaped stress-strain hysteresis loop (see Figure 2.3).

The typical pseudoelastic loading path under stresses at constant temperature (where, as stated, $T > A_f$) begins with an initial austenitic microstructure that responds linear-elastically at low stresses. When stresses are high enough to reach the martensite start stress σ_{Ms}, stress-induced transformation of to detwinned martensite initiates and leads to a near-constant-stress plateau that lasts until the martensite finish stress σ_{Mf}, during which most of the transformation strain is accumulated. Beyond σ_{Mf}, the fully transformed martensite deforms elastically with a Young's modulus typically lower than when found in austenitic state.

Unloading at the martensite state back down to the austenite stress creates a reverse plateau during which the material reverts its microstructure and the macroscopic strain recovers. At this stage of the cycle, just as with the SME, residual strains are often present although often very small (<0.1-0.2%) in well-processed alloys [16].

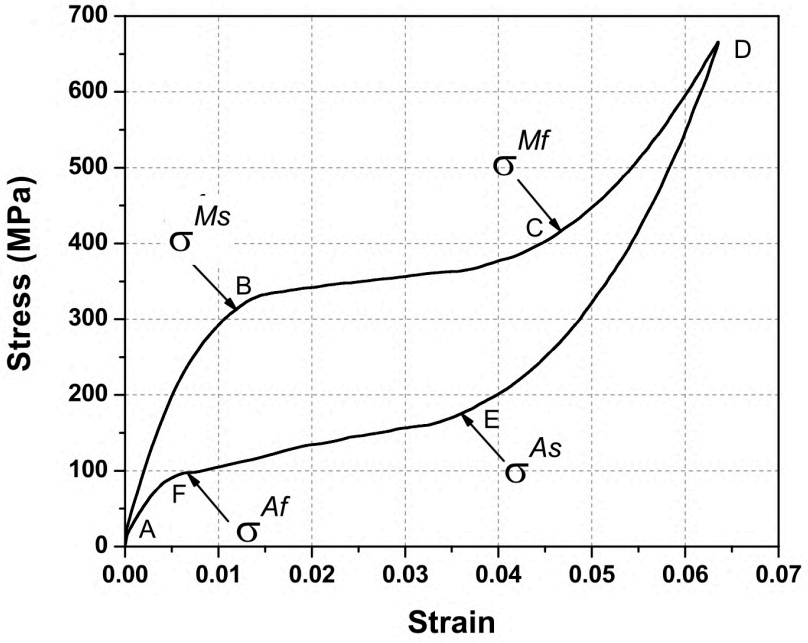


Fig. 2.3 | Typical superelastic loading cycle. Stresses at which phase transformations occur are indicated. Notice the plateaus between loading step B to C and unloading from E to F. [1]

The width of superelastic hysteresis, described as the difference between loading and unloading plateau stresses, represents the mechanical energy dissipated per cycle and demonstrates the excellent damping capabilities of SMAs [16, 19, 61]. The transformation stresses increase with temperature, someything that can be seen in phase diagrams plotting transformation boundaries in the stress-temperature space [1].

NiTi alloys in its superelastic form are widely used in medical device such as self expanding stents and guidewires [30], or in structural applications as energy dissipation devices in fields such as civil engineering [61]. In the context of actuators, superelasticity could be of interest for achieving high strokes thanks to the large allowable strains, however its uses in literature are significantly more limited compared to those harnessing the SME.

Although superelastic NiTi exhibits excellent recoverable strain capability, repeated transformation cycling may gradually alter its functional behavior. Cyclic loading can lead to shifts in transformation stresses, changes in hysteresis width, and the accumulation of small residual strains due to microstructural evolution and defect generation within the material [1, 16]. This phenomenon, commonly referred to as functional fatigue [16], differs from conventional structural fatigue and is often a critical consideration in applications involving large numbers of transformation cycles.

2.4. Types of SMM and their applications

2.4.1. Shape Memory Alloys (SMAs)

SMAs are the technologically most mature class of SMMs and form the backbone of current shape memory actuator technology [1, 24]. The most used and important systems are NiTi-based alloys, including ternaries such as NiTiCu, NiTiPd, or NiTiHf, and Cu-based alloys (Cu-Zn-Al, Cu-Al-Ni), with emerging Fe-, Co- and high-temperature SMA (HTSMA) systems for more specialized applications [62].

As mentioned by M. Jani, NiTi SMAs exhibit transformation strains of approximately 8% in tension, with even higher values achievable in compression for certain microstructural states. They can generate high actuation stresses, reaching several hundred megapascals, while maintaining good fatigue performance when operated within appropriately limited stress and strain ranges [1]. In addition, NiTi alloys offer excellent corrosion resistance [1-4, 21] and biocompatibility [30], which has enabled their extensive use in biomedical applications. A relevant characteristic, important for the development of this work, is the tunability of the transformation temperature. In standard compositions, it can be adjusted from below 0 °C to approximately 100-110 °C, while high-temperature SMAs (HTSMAs) extend this range beyond 200-300 °C through alloying additions such as Pd, Pt, Hf, or Zr [1, 62] although these are significantly more expensive and difficult to acquire.

The combination of having the SME and superelasticity places SMA at the high energy density, low frequency region of actuation maps [6, 7, 9].

Their applications span multiple sectors: from transportation, to energy, and to medicine [10, 18, 30]. In aerospace and space systems, SMAs enable morphing structures such as variable geometry airplane wings [35], and are employed in structure release and deployment mechanisms [11] and in folding systems for antenna or solar panel deployment [8].

2.4.2. Shape Memory Polymers (SMPs)

Shape memory polymers (SMPs), such as polyether ether ketone (PEEK), are polymeric materials that can be deformed into a temporary configuration and subsequently recover their original shape upon application of an external stimulus, most commonly heat. In contrast to shape memory alloys, where the SME is governed by a martensitic phase transformation, the SME in SMPs arises from either a thermal, magnetic, solvent, electrical, or light activated transition [28], such as a glass transition or the melting of a soft segment, combined with the elastic restoring force of the polymer network [24].

Compared with SMAs, SMPs exhibit significantly lower stiffness and strength, but they are capable of very large recoverable strains, often exceeding 100% [23, 24]. As polymers, they also benefit from lower density and considerable ease of processing through techniques such as casting, additive manufacturing, foaming, or even 3D printing. Their

transition temperatures can be tailored through the polymer's chemistry [32], allowing a high degree of design flexibility. However, for a given volume, SMPs generally display slower response times and lower force output compared to SMAs [16]. Their SME cycle is also different from SMAs in the sense that their elastic modulus changes inversely with temperature, meaning they soften when temperature increases and this allows for higher deformation under stress.

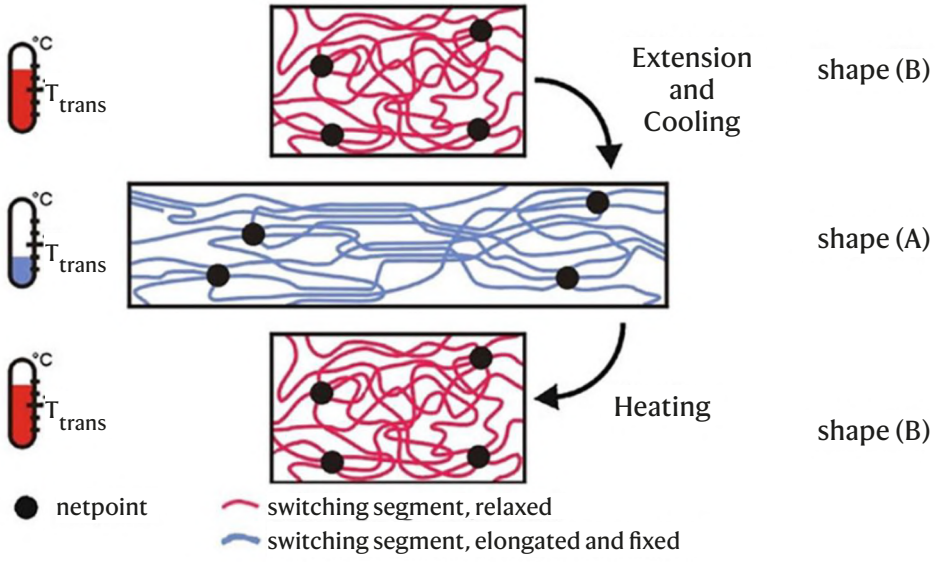


Fig. 2.4 | Molecular mechanism of the shape memory effect in a polymer. If the surrounding temperatue is above the polymer's transition temperature (usually the Tg), the switching segments gain flexibility. If the polymer is held under stress and let cool down, once the stress is released the shape is mantained. The recovery of the initial shape is obtained when the SMP reaches its transformation temperature a second time. [24]

A highly interesting property that is unique of SMPs is their position locking capability. When the temperature of a polymer is increased above its glass transition temperature (T_g), softening occurs due to enhanced chain mobility gained via thermal energy, which produces higher free volume and consequential chain sliding. If a SMP is deformed under this state and kept at the deformed position without removing the external stress, once the SMP cools back below the T_g and recovers its glassy state enabling chains to reaccommodate, the SMP will gain its original stiffness back with the polymeric chains "frozen" in that deformed configuration. If the SMP is then heated above T_g once again, the chains will "remember" their natural configuration, reversing at the molecular scale and exhibiting a macroscopic strain to return to its original shape [12].

Applications of SMPs in space include deployable structures [32] or sun-tracking solar panels for satellites [12] where large strains under modest stresses are advantageous. In the context of space actuators, SMPs could be particularly attractive for low-load, large-stroke deployment mechanisms and for scenarios where low-energy position locking is a requisite. Nevertheless, their limited load-bearing capacity and especially their sensitivi-

ty to radiation and environmental conditions [21] are big restriction to their use in space relative to metallic SMMs.

2.4.3. Shape Memory Ceramics (SMCs)

Shape memory ceramics (SMCs) represent a more recent class of SMMs in which the SME and superelasticity arise from martensitic transformations in ceramic systems, most notably doped zirconia (ZrO_2) and related oxides [19]. Historically, martensitic transformations in ceramics such as partially stabilized zirconia have been exploited for transformation toughening [22]. However, the manifestation of macroscopic shape memory behavior was previously prevented by the common brittle fracture and cracking at relatively low strains of ceramic materials, caused by large transformation-induced mismatch stresses between adjacent grains [22].

Recent studies, mainly led by MIT's Cristopher A. Schuh group, have demonstrated that appropriate size scaling and careful microstructural control can suppress transformation-induced cracking and enable robust SME and superelasticity in ceramic materials. This was achieved by fabricating single-crystalline or oligocrystalline micrometer-scale zirconia pillars. Lai et al. showed that fully recoverable superelastic strains of approximately 7–8% can be achieved under compression or bending at room temperature, with stable behavior over tens of loading cycles. The authors also demonstrated shape memory behavior in bending pillars, where a bent martensitic configuration is recovered upon heating above the austenite transformation temperature, which is around 500°C for certain compositions. In addition, the authors show how these materials exhibit very high transformation stresses on the order of gigapascals, leading to actuation work densities approaching 100 MJ/m^3. These values exceed those of many SMAs and are comparable, in terms of specific work, to hydraulic systems.

Because ceramics generally possess higher strength and superior elevated-temperature stability than metals, SMCs present opportunities for high-temperature, high-stress actuators and damping elements, as well as impact-resistant structural components that exhibit pseudo-ductile behavior through transformation mechanisms. At present, however, these behaviors have only been demonstrated at small scales and require stringent control of microstructural features such as grain size and dopant distribution, as claimed by Lai et al. Considerable research is still required to translate these effects into reliable macroscale components for real-world applications.

In the context of space systems, SMCs are of interest for high-temperature actuators or latching mechanisms capable of operating well beyond the conventional temperature limits of NiTi alloys, as well as for high-strength, high-energy damping elements in harsh thermal and radiation environments also due to their chemical inertness.

2.5. Types of bidirectional shape memory actuators

To achieve bidirectional motion using a shape memory material, four main approaches can be distinguished. Three of them rely on the one-way shape memory effect (OWSME), while the fourth uses the so-called two-way shape memory effect (TWSME).

When an actuator operates based on the OWSME, the shape memory material is only capable of generating force and displacement in one direction, this one being the recovery path from its deformed to memorized shape during phase transformation. Therefore, an external biasing element is required to bring the actuator back to its initially deformed position as soon as it has cooled, that is when the material transforms back to martensite and becomes significantly easier to deform.

The two most basic OWSME configurations employ either a bias spring or a bias weight [3, 16]. In both cases, the SMA actuator overcomes the opposing bias force during heating, producing the desired motion, and upon cooling, the decrease in stiffness associated with the martensitic phase allows the bias element to deform the SMA back to its original configuration, thus completing the actuation cycle and providing bidirectional movement. Although these systems are relatively simple and reliable, they come with an important limitation: the actuated position can only be maintained while the SMA remains heated. As a result, continuous electrical power is required whenever the mechanism must remain in its activated state, which leads to considerably high energy consumption levels whenever the activated position must be held for extended periods of time.

A third configuration replaces the passive biasing element with a second shape memory actuator. In this arrangement, the two SMA elements operate alternately. When one actuator is heated and transforms into austenite, it generates sufficient force to deform

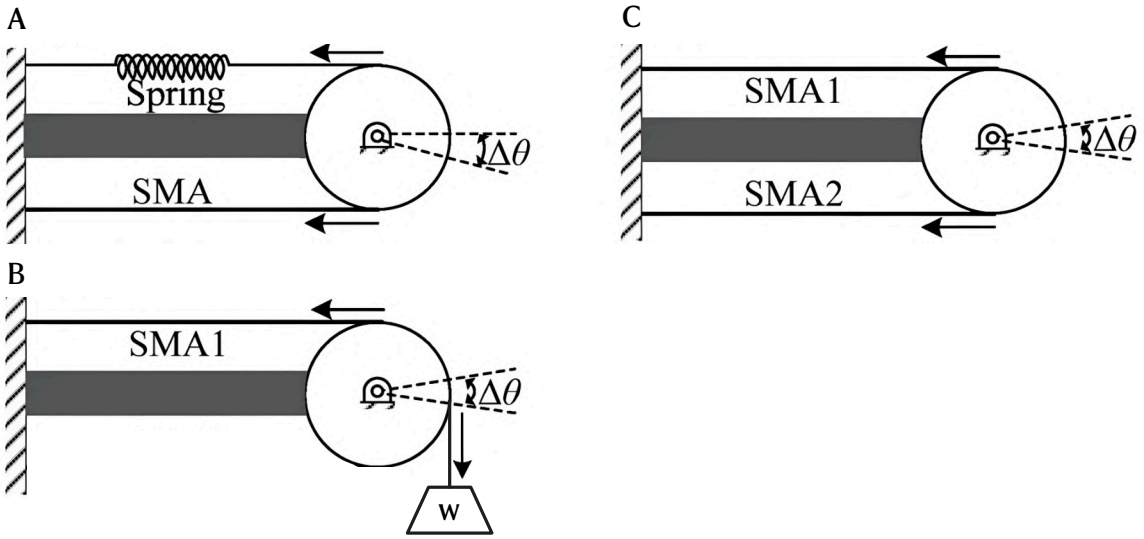


Fig. 2.5 | Bidirectional actuation systems for OWSME materials. Assemblies A and B depict the use of a bias force, while assembly C uses antagonist SMAs. Adapted from [26].

the second actuator, which remains in the softer martensitic state. During the subsequent actuation cycle, their roles are reversed. Since each actuator is capable of recovering its own memorized shape, no passive bias element is required, and both positions can be maintained without continuous power input provided that the system has reached the corresponding equilibrium configuration.

An alternative approach to the previous three consists of using the two-way shape memory effect (TWSME), in which the material is capable of remembering one shape at high temperature and a second shape at low temperature without requiring any external biasing element [1, 16, 26]. Unlike the one-way effect, this behavior is not an intrinsic property of the alloy and must be introduced through a training process [16]. Such training typically involves repeated thermal cycling while the material is constrained in its low-temperature configuration, creating internal defects within the martensitic microstructure that give a preferential variant reorientation during cooling [16]. Despite eliminating the need for a biasing element, TWSME generally produces significantly lower recoverable strains than OWSME [1, 3, 13, 16], and the training required to obtain stable two-way behavior are often complex [1, 16]. Consequently, its use in commercial actuator systems remains relatively limited [16].

Chapter 3
Methodology

The approach or procedure of this work is based on a ruled-chain design methodology adapted from Yuan et al. [6]. As explained earlier in the Chapter 1, it is a design research approach that is not linear and instead allows for the exploration of a wider space of possible solutions. It is specifically devised with the intent of adhering to the framework of the final application, therefore ensuring that all outcomes will unequivocally have a real potential for being a feasible solution.

3.1. Requirements and Constraints (RCs)

In this section, Requirements and Constraints (RCs) were expressed and examined to later derive Design Rules (DRs) and subsequently obtain Design Features (DFs). RCs –and in the following section DRs– are described in bullet points to provide a clearer visualization. Such constraints had been defined from the familiarization with the working conditions in regard to the VERITAS and EnVision missions, together with the boundaries and limitations of the design that were given by the DLR.

- **RC-1**: Bidirectional motion is sought. This is essential for performing shielding-exposure cycles as opposed to the current one-shot version. The possibility of exposing and covering with a full rotation (i.e. always rotating the window cover following the same path) is disregarded due to spatial limitations.
- **RC-2**: Passive position locking is strongly desirable. This requirement will help reduce the power consumption of the design, provided that locking is achieved without applying any external energy.

- **RC-3**: Compact actuator with preferred motion orthogonal to the frontal-rear axis, as the available space along this axis is the tightest with only 9 mm.
- **RC-4**: The full displacement of the cover must be equal or greater than the minimum aperture of 22 mm.
- **RC-5**: Phase transformation of the SMA must not be triggered unexpectedly, especially considering the mission's peak temperatures on exposed surfaces can go beyond 110°C during Sun calibration.

3.2. Design Rules (DRs)

A Design Rule (DR) is also a form of constraint. They are obtained from translating and breaking down RCs into a new set of requirements that are more specific and can help derive DFs. To balance the span of the design space, each RC was set to strictly provide three DRs. During the design process, the solution space is progressively reduced through "restrictive" selections, which funnel a single DR among many alternatives, or reframed through "interference" choices, which derive additional rules or refuse selected ones due to factors that may have not been initially considered. This iterative process ultimately leads to the definition of concrete DFs.

- From **RC-1: Bidirectional Motion** we could consider:
    - DR-1a: using a one-way memory effect SMA component in opposition with a bias spring.
    - DR-1b: using two one-way memory effect SMA components acting as antagonists.
    - DR-1c: using a two-way memory effect SMA.

In this first RC, DR-1c was considered as not being an option due to SMAs with a two-way memory effect having lower stroke amplitude, being more difficult to train, not being as commercially available, and having a significantly higher price [1, 6, 16]. Both DR-1a and DR-1b were considered to be feasible candidates for this first requirement.

- From **RC-2: Position Locking** we could consider:
    - DR-2a: using a shape memory polymer (SMP), which can be easily deformed above its glass transition temperature (T_g) and locked at that state as long as stress is maintained during cooling.
    - DR-2b: using the deformed martensitic states of two antagonist SMA elements.
    - DR-2c: using a compliant mechanism with at least two stable positions.

RC-2 requires having the possibility of "freezing" a certain position in place, ideally without the need for external power. Thus, there's an interference decision with DR-1a,

considered feasible on the previous evaluation, which must therefore be disregarded at this stage since it can only achieve stable position locking as long as the SMA is being heated (i.e. active position locking). Moreover, due to the realistic feasibility of the three options in this RC, DR-2a, DR-2b and DR-2c were deemed relevant.

- From **RC-3: Longitudinal Compactness** we could consider:
    - DR-3a: convert the action of SMA elements into rotational motion around the central axis.
    - DR-3b: use a compliant structure to minimize space and reduce the number of parts.
    - DR-3c: use the SMA element itself to be the shield, eliminating the necessity for having other components that could take up space.

In this case, once again, all proposals were considered relevant for the design. On the one hand, performing a rotation on the plane orthogonal to the frontal-rear axis does not affect the longitudinal volume during motion, which is the tightest, and it therefore complies with RC-3. In regard to DR-3b, making use of a compliant assembly is highly beneficial for compactness and miniaturization, as this kind of mechanisms have already been successfully manufactured at the nanoscale [53]. Lastly, option C offers a unique way of solving spatial constraints by eliminating all parts except for the SMA component.

- From **RC-4: Minimum Aperture** we could consider:
    - DR-4a: the direct stroke produced by the SMA element is equal or greater than the required aperture displacement.
    - DR-4b: combining multiple SMA elements acting sequentially to generate the required total displacement.
    - DR-4c: using a mechanical amplification system to convert the limited SMA strain into the required aperture displacement.

The minimum aperture of 22 mm could be feasibly achieved with a single SMA element if produced in a spring-like or folded configuration, hence DR-4a was an accepted option. Using multiple actuators is also a feasible option, however the higher values in electrical power and the complexity of assembling an increased number of parts made DR-4b to become disregarded, with the added cause that it interferes with requirement RC-3. The designing of a mechanism that can amplify the movement of the SMA component was thought to be an attractive solution to minimize the size of the SMA and the power required for the completion of a full stroke, hence DR-4c was deemed relevant.

- From **RC-5: Temperature Stability** we could consider:
    - DR-5a: applying an antireflective thermal coating to provide a layer of thermal isolation to the exposed SMA.
    - DR-5b: ensuring the SMA is outside the direct exposure region.

- DR-5c: using active or passive thermal management to cool the SMA when necessary.

From this fifth set of design rules, DR-5a and DR-5b were identified as good alternatives that also matched with all previous requirements (from RC-1 to RC-4). To reduce the risks of RC-5 even further, an additional DR-6 was suggested with the claim of selecting a SMA with a transformation temperature above the mission's peak ($M_s > 110°C$). The option of including a thermal management system was rejected, however, due to it consuming more electrical power and adding bulk mass and volume, something that was already been expressed as undesirable in RC-2 and RC-3 respectively.

An additional DR 7, introduced by interference, is the capability of the material exposed to the environment to withstand all external agents (radiation, corrosion, ductile-brittle transitions) without failure.

3.3. Design Features (DFs) and candidate proposals

Having defined more concrete restrictions for the design space, Design Features (DFs) could now be derived. These became the building blocks for the proposals by ensuring they could all satisfy the fundamental requirements defined in the beginning. Up until this point, a total of thirteen DRs were either obtained via restriction or added through interference.

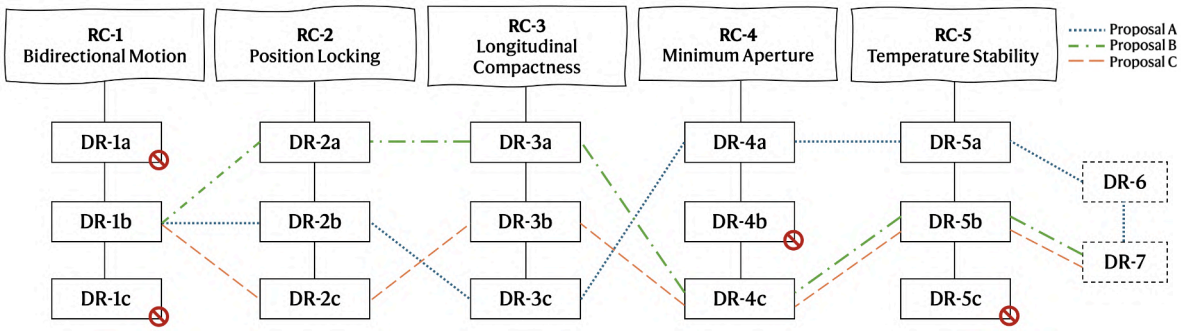


Fig. 3.1 | Mapping of the DR selection path. Irregular shapes correspond to RCs, solid-outline rectangles to restrictive DRs and dashed rectangles to interference DRs. DRs that were rejected during the evaluation process are marked with a stop sign.

Based on the previously defined DRs, several actuator architectures were considered as potential candidates capable of satisfying the set of constraints. Rather than focusing on a single configuration from the outset, different concepts were explored in order to evaluate alternative ways of achieving bidirectional motion, compact integration, passive position locking, temperature tolerance, and aperture displacement. This exploration led to the identification of three preliminary shutter concepts, each representing a distinct physical strategy for converting the actuation of SMA elements into the required shielded and exposed activity.

Starting with the first concept and following the DR path in Figure 3.1, Proposal A was clearly the most distinctive of the three, especially in regard to having a full-stroke shape memory actuation (DR-4a) and in managing the temperature fluctuations with the application of a thermal coating (DR-5a). Additionally, it was the only one requiring DR-6: a martensite to austenite transformation temperature above the mission's peak. This imperatively defines that Proposal A would incorporate the shape memory alloy in a completely exposed condition, both to the environment and to Sun radiation, with the choice of DR-3c explicitly mentioning it would be the shield itself. All previous characteristics, in particular the latter, imply that the SMA for Proposal A would need to be in the form of a foil or sheet in order to be able to cover the entire size of the aperture. Since the position locking is achieved via the deformation of an SMA element at its martensitic state (DR-2b), this brings us to the first DF of the design process: Proposal A is formed of two SMA foils, attached one on top of the other, that actuate alternately by following the basis of antagonist components. One element would be shape-set at a flat configuration, while the second antagonist SMA would keep a rolled profile when fully converted to austenite.

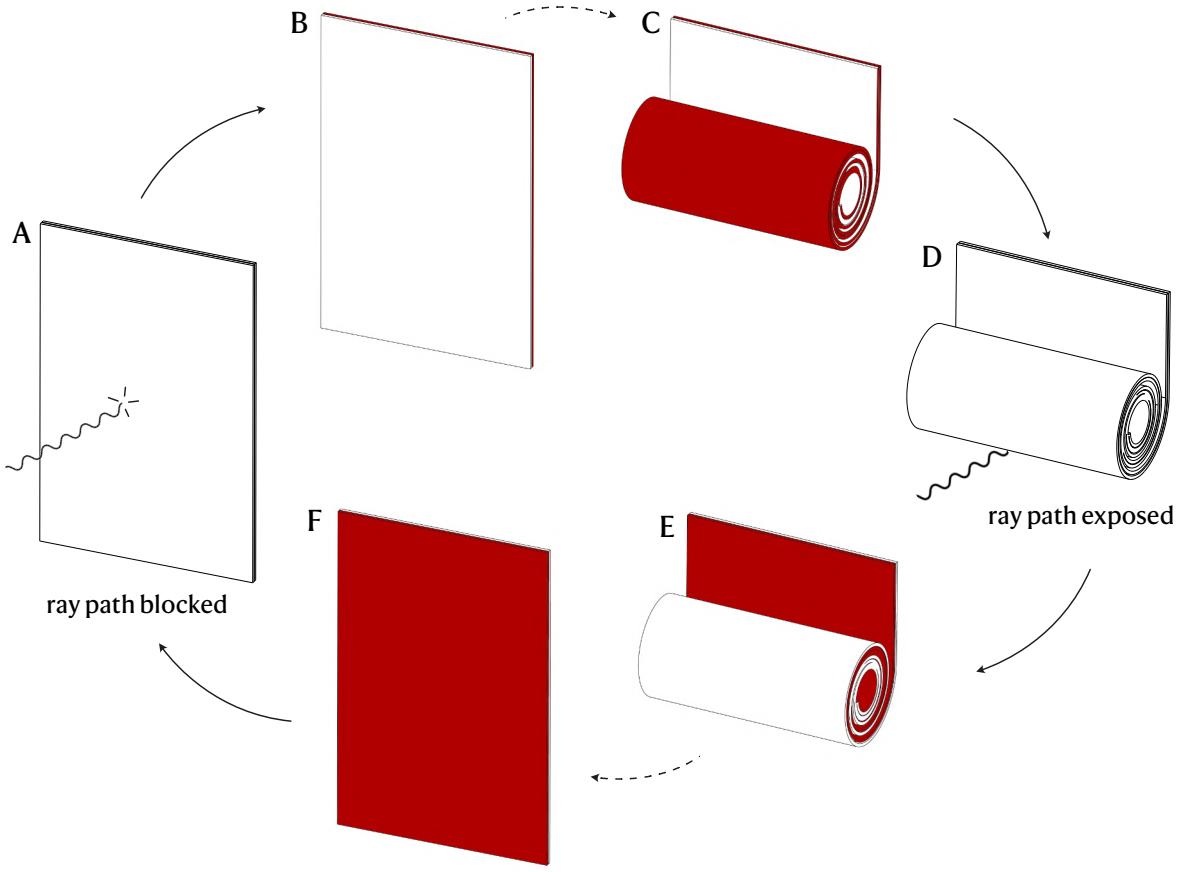


Fig. 3.2 | Actuation cycle of Proposal A. Steps A and D represent the two stable positions (closed and open shutter, respectively). The dashed arrows indicate there is a martensite to austenite transformation, while solid lines represent either a cooling or heating process. The preset shape of the front foil is flat while the back foil's is rolled, and they deform each other alternately.

There are two different conceived designs for the folding path of Proposal A. The design was initially thought to work by rolling, following the mechanics of a traditional window curtain. Nevertheless, this option was later found to be more unstable due to the potential torque generated from the asynchronous movement of the SMA, which goes from bottom to top. Another problem with the rolling design was the heating. For the foil to roll from bottom to top, it is essential that the martensite to austenite transformation also occurs in this same order. Otherwise, the SMA's microstructural transformation could bend the foil into a position that occupies the limited longitudinal space, as shown in Figure 3.3, hence failing to satisfy RC-3. This adds another obstacle into this design, since, given the fact that the electrical assembly requires current to flow from the top to prevent bending the wires, a way to make the foil be heated from below first adds extra hardware.

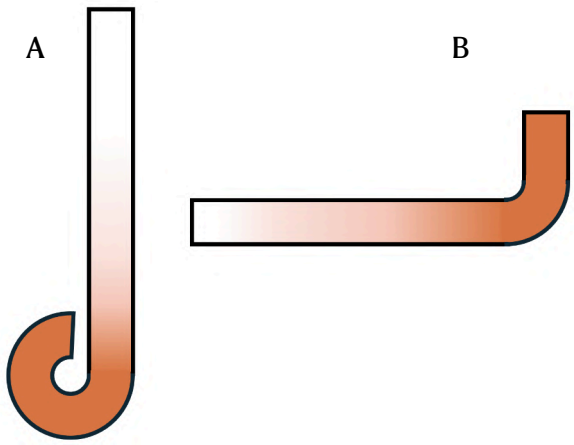


Fig. 3.3 | SMA transformation response accoring to starting point of heat flow. Illustrated lateral profile of the foil with the corresponding deformation path. In A, the martensite to austenite transformation starts at the bottom, while in B it starts from the top. Option A is preferred.

Because of these set of reasons, a more reliable design fulfilling the same DF-1 was proposed, in which instead of having rolling dynamics the SMA components would instead fold by following multiple creases on the foil. This layout removed the necessity of having bottom-to-top heating, as the position of austenite transformation on the foil does no longer matter. In fact, having joule heat flowing from top to bottom would be beneficial to reduce unwanted torque emerging from the foils moving at a point further away from the anchor point, thus finding a solution for directional heating was no longer a concern either.

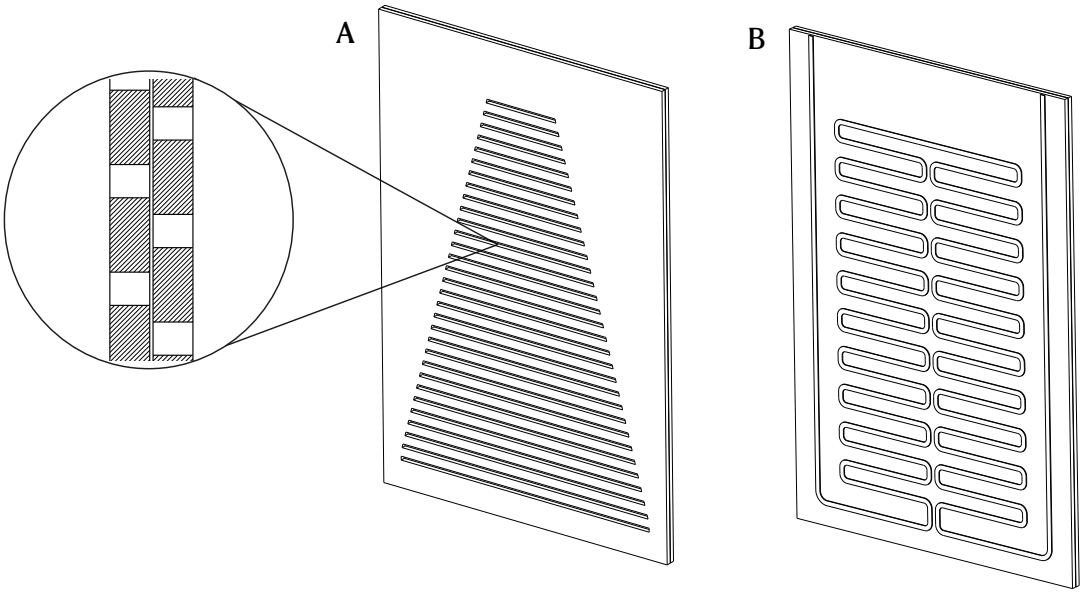


Fig. 3.4 | Possible solutions for a correct bottom-to-top rolling. In design A, slits are used to increase local resistance at the bottom by having less material. To prevent stray light or particles entering the optics, slits can be alternated as shown in the detailed drawing of the lateral section view. In design B, a serpentine path is used to direct and accumulate heat in the bottom first.

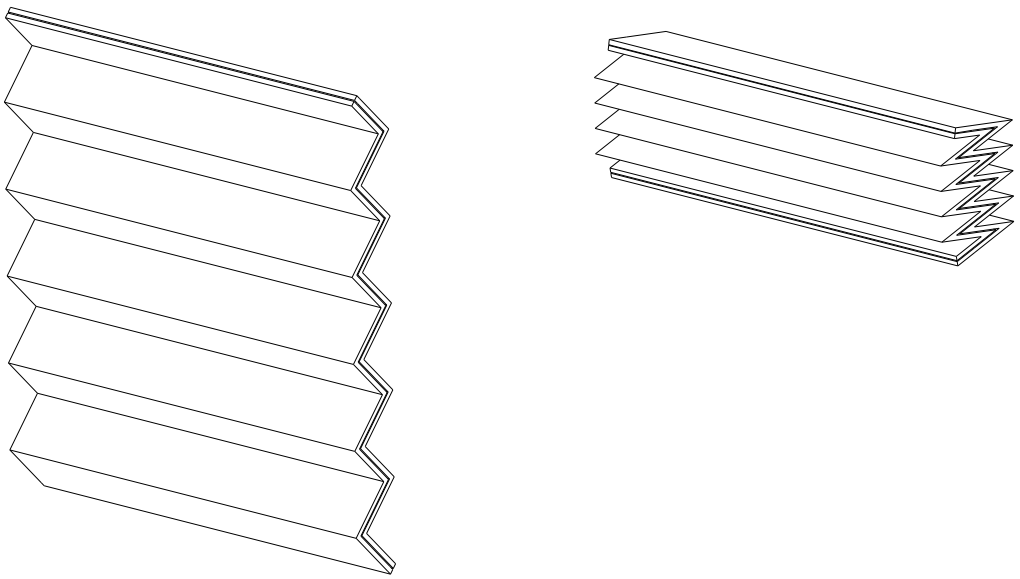


Fig. 3.5 | Improved concept of Proposal A. The inclusion of creases to force the foil into a folding shape eliminates the need for directional heating, reduces the torque of the rolling version and takes up less space in the frontal-real axis.

The second proposal uses a combination of two distinct shape memory materials, namely SMAs and SMPs. For this design, the defined DF is the following: Proposal B performs a rotary actuation and accomplishes position locking by embedding SMA wires into a SMP matrix. In Proposal B, the coupling of polymer and metal was investigated due to the fact of these having different shape-memory working principles. Taking advantage of the particularity that SMPs exhibit higher deformability with the increase of temperature while, on the other hand, SMAs become stiffer under the same conditions, this design harnesses the increase of temperature to exploit the capability of a high-stiffness austenitic SMA to deform a highly compliant, rubbery SMP that finds itself past its glass transition temperature.

This second concept uses the SMP as the exposed material to the environment, as it is used as the shielding part of the optics. The actuation cycle starts with the SMP covering the instrument's ray path and, when the shutter wants to be opened, the temperature on the SMA is risen by applying a high current –following the exact technique of Joule heating as in Proposal A. Since the SMA, this time in the shape of a wire instead of a foil, is embedded inside the SMP, the polymer gets heat transferred through conduction. A

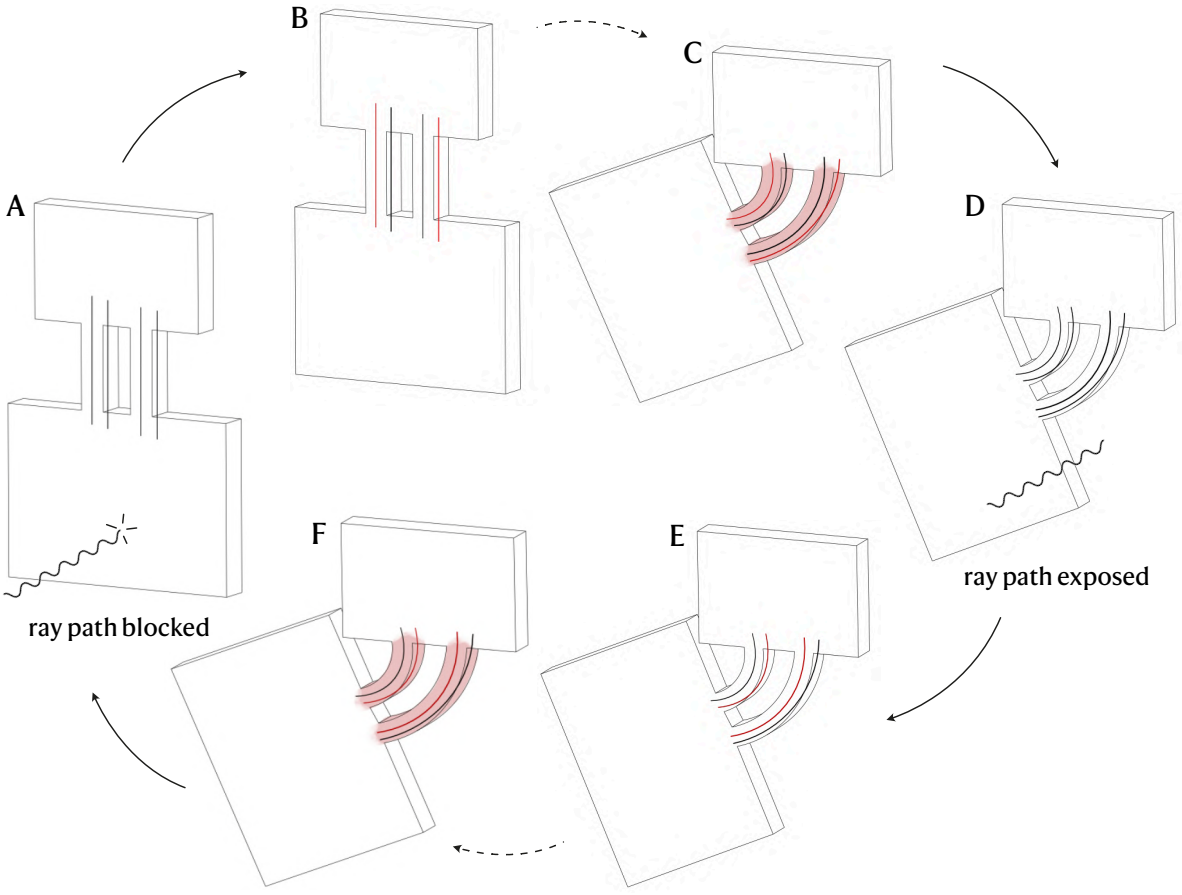


Fig. 3.6 | Actuation cycle of Proposal B. Steps A and D represent the two stable positions. Two SMAs are heated to open the shutter, while the other two close it. These are embedded inside the SMP matrix, which gets heated up to T_g to reach a rubbery state and exhibit the second SME.

lower cross section in the area of desired deformation allows the part of interest to reach the glass transition temperature reasonably fast, making it turn rubbery. The difference in elastic modulus from both materials is significantly increased as the one from the SMA rises while the SMP loses stiffness. Consecutively, the effort from the wires to return to their original austenitic shape apply a stress to the SMP, forcing it to follow the same path until the SMA achieves the memorized shape. Once at that position, the current can be removed, both materials cool down and the SMP recovers its stiffness while maintaining the deformed configuration.

In order to move back to its closed formation, the antagonist SMA is heated and the same principle is followed: the SMP absorbs the heat from the metal wire and is forced to go back to the closed position, with the only difference that this time the SMP also returns back to its initially memorized macromolecular layout and thus reduces the force requirements of the second SMA.

To complete the selection of candidates, the third design has the following DF: Proposal C takes advantage of compliant flexures to accomplish a shutter with two stable positions. This third concept is of considerably faster actuation than the previous due to solely depending on achieving a bending position high enough for producing a snap-through transition between the first and the second stable positions.

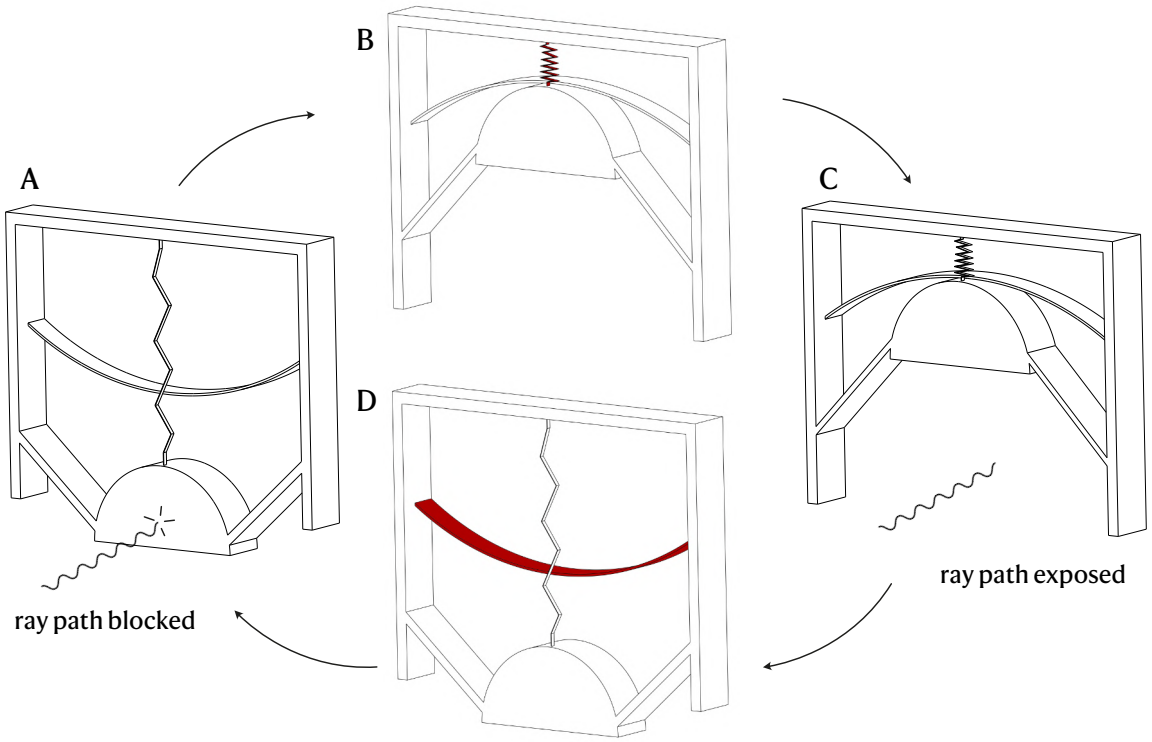


Fig. 3.7 | Actuation cycle of Proposal C. Steps A and C represent the two stable positions. The SMA wire is used to open the shutter (B), while the SMA strip is used to close it (D). The "shuttle", a term that will be used in this report, is the moving part blocking and exposing the ray path.

The actuation of the shutter works with antagonist SMAs that deform one another through the bistable transition of the flexures from one position to the other. Once the current is applied on one of the SMA actuators, its phase transformation force must be sufficient to overcome the activation force of the compliant flexure, which when moving from opened to closed deforms the second SMA –fully martensitic– allowing cycle reversal by heating it and bringing it back to its undeformed state.

vSince all proposals were obtained from the definition of initially defined constraints and developed through design characteristics in accordance with the aforementioned requirements, it could be rested assured that they all satisfied the preliminary conditions for the application. Nevertheless, a brief second screening containing real mission data such as temperature range, maximum mass, maximum allowable power consumption, dimensions, and tolerable actuation speed, all obtained from the different departments and teams present on this mission, was performed to verify the feasibility and alignment of all three candidates. As they all passed the preliminary evaluation, the choice of which option to develop followed and is detailed in the next section.

3.4. Evaluation and proposal selection

To select the most suitable candidate from the three proposed concepts, a weighted decision matrix was employed. This method was chosen because it provides a structured and transparent framework for comparing alternatives based on quantifiable material properties and performance criteria. At the same time, the approach allows the evaluator to assign relative importance to individual criteria, thereby incorporating engineering judgment into the assessment process. The combination of data-driven evaluation and professional judgment was considered to provide a balanced and reliable basis for the selection of the most suitable concept.

Before constructing the decision matrix, an initial feasibility assessment was performed to verify that each of the three proposed concepts was capable of meeting the minimum functional requirements of the intended application. This preliminary evaluation indicated that all concepts were technically viable, provided that an appropriate material and geometry were selected. Consequently, the objective of the decision matrix was not to determine whether a concept was feasible, but rather to identify the alternative offering the best overall performance with respect to the project requirements.

The criteria included in the evaluation matrix (found in Table 3.1) were first identified based on the functional requirements of the device and the design objectives established during the previous sections. Subsequently, each criterion was assigned a weighting factor reflecting its relative importance to the final application. The weighting process was carried out collaboratively by multiple evaluators in order to reduce individual bias and to obtain a more representative assessment of the project's priorities. Thus, greater weighting was assigned to parameters considered critical for the successful operation of the device, whereas secondary characteristics received proportionally lower weights.

Table. 3.1 | Criteria used in the evaluation of proposals. The technical parameters, each weighing 10%, account for 40% of the total score.

Criterion	Definition	Weight (%)
Reliability	Probability the design has of performing its function consistently as intended, without failure, during the specified period of time, under the defined operating conditions.	25
Size, mass, scalability	Considers: 1. Ability of the design to be enlarged or reduced while maintaining performance, 2. Compactness, 3. "Lightweightness".	10
Energy Consumption	Total electrical energy used. Considers: 1. Required power and 2. Time for the completion of an entire actuation cycle.	10
Mechanical	Considers: 1. Ability to keep structural integrity and geometry (robustness), 2. Resistance to random and sine loads.	10
Thermal	Ability to function under high temperatures and withstand extreme fluctuations.	10
Cost	Considers: 1. Monetary investment, 2. Time for development, 3. Complexity of the design.	15
Manufacturability	Considers: 1. Tools and processes required for the production, 2. Availability of components.	20

Once the weighting factors had been established, each concept was independently evaluated against every criterion using a numerical rating scale ranging from 1 to 3, where higher scores indicated better performance. In order to have more distinct ratings, it was established that the score could not be repeated when evaluating the same criterion. The assigned scores were based on engineering analysis, literature, and qualitative assessment where quantitative information was not yet available. For each criterion, the rating was multiplied by its corresponding weighting factor, and the weighted values were summed to obtain the final score of each concept according to:

$$\sum_{i=1}^{n} w_i r_i \tag{3.1}$$

where w_i represents the weighting factor assigned to criterion i, r_i is the rating of the evaluated concept for that criterion, and n is the total number of evaluation criteria.

The reader is referred to Appendix A for the complete evaluation matrix and a detailed breakdown of the decision-making process. Based on the weighted scores, Proposal C achieved the highest overall rating and was therefore selected for further development.

This outcome was primarily driven by its superior robustness, lower expected energy consumption, and greater scalability compared with the other concepts. In addition, Proposal C was regarded as the solution with the best mix of uniqueness and challenge, something that was also considered important during the assessment.

Although the final ranking inevitably incorporates a degree of engineering judgment through the selection of evaluation criteria and their corresponding weighting factors, the weighted decision-making provides a strctured and transparent methodology that accounts for multiple performance aspects without relying on a single criterion or subjective preference.

Chapter 4

Concept Development

4.1. Compliant mechanisms and bistability

Compliant bistable mechanisms are a class of mechanical systems capable of having two distinct stable equilibrium configurations without requiring continuous external energy input. Unlike conventional mechanisms, which rely on rigid bodies connected through joints, bearings, or hinges, compliant mechanisms achieve motion through the elastic deformation of one or more flexible members [54]. The integration of flexibility directly into the structure allows motion and force transmission to occur without separated moving parts, resulting in a monolithic architecture.

Bistability arises from the existence of two local minima in the system's energy, separated by an unstable equilibrium state (Figure 4.1-A). When sufficient external force is applied, the mechanism transitions from one stable state to the other by overcoming an energy barrier. Once the transition is completed, the mechanism remains in its new configuration without the need for additional power input. This characteristic distinguishes bistable mechanisms from purely elastic structures that return automatically to their original configuration after unloading. The force-displacement response of a typical compliant bistable mechamism, in Figure 4.1-A, reflects this behavior. Initially, the required actuation force increases as elastic strain energy accumulates within the flexible segments of the structure [54]. As the mechanism approaches the unstable equilibrium point, the force reaches a maximum value. Beyond this critical point, in which it is found the so-called activation force, a snap-through event occurs and the required force decreases rapidly as the mechanism transitions into its second stable state. Consequently,

the force-displacement curve exhibits a characteristic non-linear shape associated with energy storage and release [53].

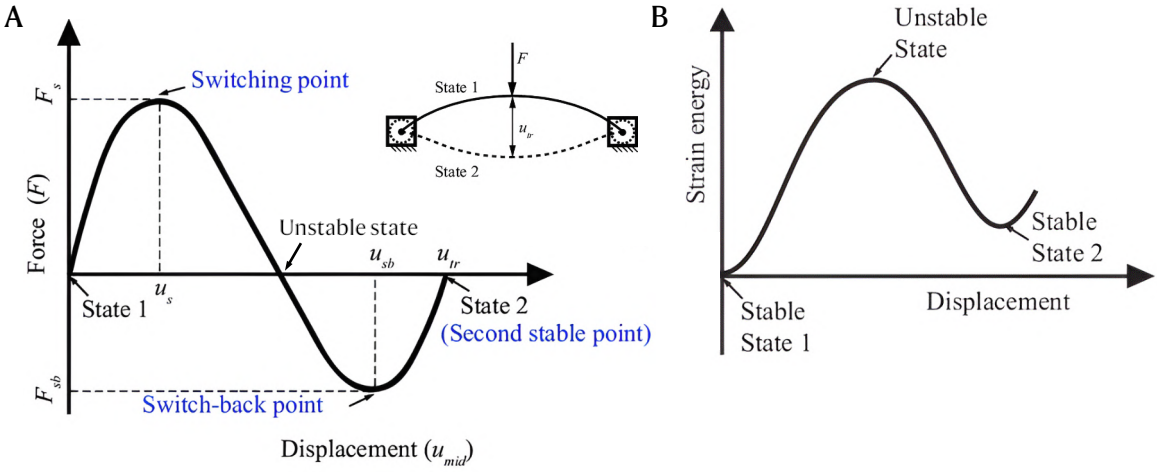


Fig. 4.1 | Typical behavior of a bistable mechanism. Force vs Displacement graph (A) showing the activation (switching) and return (switch-back) forces, unstable position, and two stable states. Strain energy graph (B) as an alternative representation of the bistable behavior. [54]

This behavior can also be understood from an energy perpective (Figure 4.1-B). In a monostable system, the total potential energy contains only a single minimum corresponding to the undeformed configuration [53]. By contrast, a bistable system possesses two distinct minima separated by a local maximum, with the latter corresponding to the unstable equilibrium configuration [53, 54]. To transition between stable states, external work must be supplied to overcome the energy barrier associated with this unstable configuration.

As explained by Howell, it is important to consider that the magnitude of this energy barrier strongly influences the actuation force, snap-through behavior, and stability of the mechanism. A high energy barrier generally improves resistance to unintended switching caused by vibration or external disturbances, but it also increases actuation force requirements. Conversely, a low energy barrier facilitates switching though it might cause a reducton in positional stability. As a result, designing a bistable mechanism frequently involves balancing these two depending on the desired behavior of the mechanism.

The absence of traditional joints offers several advantages compared to conventional mechanical systems. Compliant mechanisms generally exhibit reduced friction, negligible backlash, lower wear rates, improved reliability, reduced maintenance requirements, and lower overall part count [45, 46, 49]. Since motion is achieved through material deformation rather than relative sliding between components, lubrication is often unnecessary [46]. These characteristics are particularly attractive in applications where maintenance access is limited or, as it is the case of this project's context, where lubricants cannot be used.

The ability to remain in either stable state without continuous power consumption represents another important reason for having chosen Proposal C. A bistable mechanism can function with passive position locking, consuming energy only during the transition between stable states. This feature has also made bistable structures to become of very high interest in the field of space systems, with research in morphing structures [35] and space deployment mechanisms [45].

There exist several analytical models to capture the large deflection behavior of compliant mechanisms, which is inherently geometrically non-linear [33]. As it can be difficult to analyze using conventional rigid-body approaches, compliant segments are often represented using pseudo-rigid-body models (PRBMs), first introduced by Howell in the 1990s. In this approach, flexible members are replaced by rigid links connected through torsional springs located at characteristic pivot points [45, 46, 53]. This approximation enables to apply established rigid-body kinematic techniques while retaining the essential mechanical behavior of the compliant structure, significantly reducing computational complexity compared to full finite element simulations although being less precise [50].

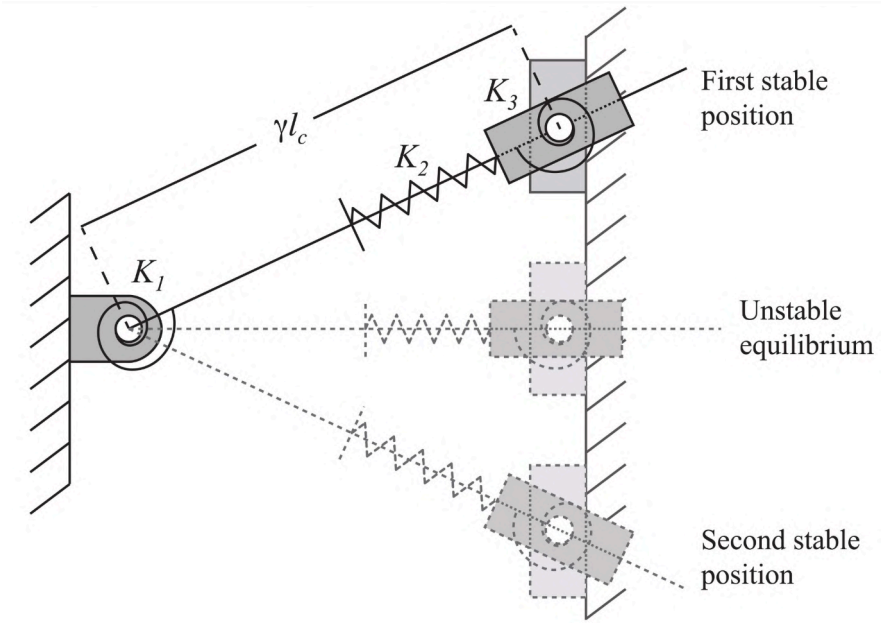


Fig. 4.2 | Schematic of the pseudo-rigid-body model. Rigid segments with the system's compliance modelled with torsional and linear springs. [45]

4.2. Early prototypes

Prior to the numerical modelling stage, several proof-of-concept prototypes were manufactured using polymer additive manufacturing. These intial designs were developed primarily from intuition and a limited understanding of compliant bistable behavior. The resulting prototypes failed to exhibit bistability, as the flexural members

did not deform sufficiently to generate a snap-through instability. Instead, localized stresses in the joints caused premature fracture of the beams before a second stable configuration could be reached. These early failures highlighted the sensitivity of bistable behavior to geometry and stiffness, and emphasized the need for a more systematic design methodology.

To validate the operating principle experimentally, a refined prototype based on dimensions reported in the work of Zirbel et al. was manufactured and tested. This design successfully demonstrated an excellent bistable behavior and served as the starting point for the numerical optimization process. Once the concept had been validated experimentally, the geometry was adapted to satisfy the dimensional constraints imposed by the VEM instument.

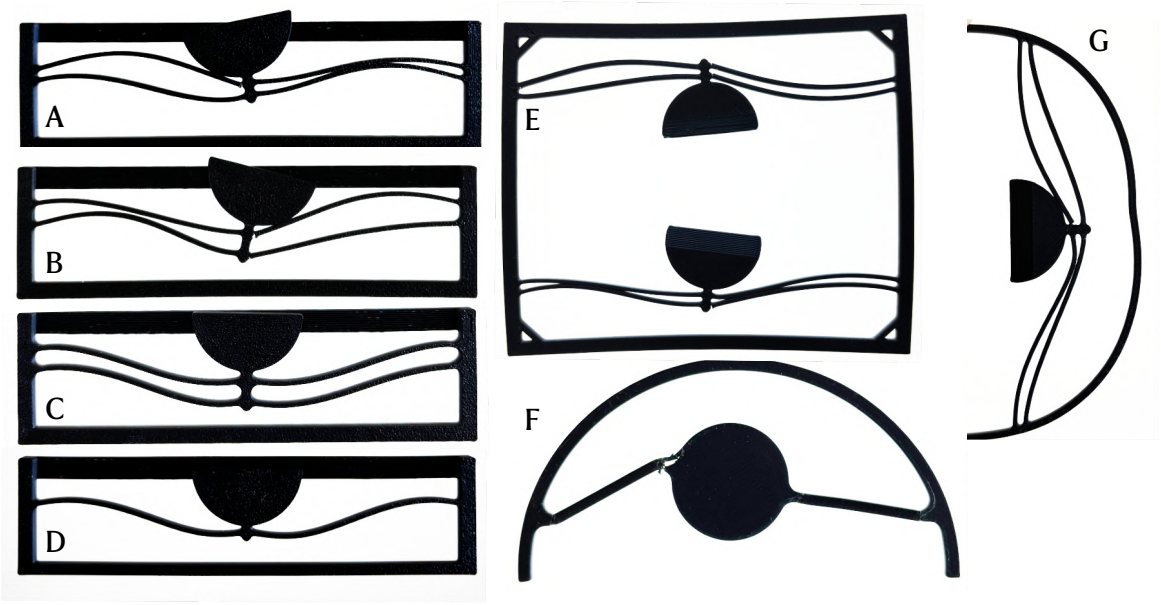


Fig. 4.3 | Early prototypes of the bistable flexure. It can be observed how fractures occurred in the same location, namely in the middle flexure joints. Prototypes C and D didn't fracture, even after several cycles, possibly due to increased fillet radii and and larger middle-joint area which decreased stress concentration in the central part.

From this initial round of prototypes, two critical events were witnessed. On the one hand, the mechanism's ability to cleanly snap-through and reliably hold its second equilibrium state was reduced when the size was scaled down. Additionally, fracture always occurred in the same place, namely in one of the inner joints. Regarding the first issue, it was observed that several prototypes didn't hold its bistable position due to out-of-plane deformation or lateral buckling. Prototypes with width-to-thickness ratios approaching 1 suffered significantly more from lateral buckling and therefore exhibited less stable secondary positions. As out-of-plane deformation heavily depends on the ratio of out-of-plane stiffness to in-plane stiffness [72], higher width-to-thickness ratios

showed to provide greater resistance to lateral buckling forces during the snap-through action. Being the respective moments of inertia for in-plane and out-of-plane deformations:

$$I_{in} = \frac{w \times t^3}{12} \tag{4.1}$$

$$I_{out} = \frac{t \times w^3}{12} \tag{4.2}$$

The resistance to out-of-plane deformation relative to the force required to snap the beam is dictated by the following ratio, which can be simplified directly:

$$\frac{I_{out}}{I_{in}} = \left(\frac{w}{t}\right)^2 \tag{4.3}$$

Hence, for the development of the numerical model, a minimum in-to-out-of-plane stiffness ratio of 2.25 was defined, although higher ratios are preferred.

In regards to the location of the fractures, increasing the fillet radius and the thickness of the shuttle showed significant improvement in the number of cycles the prototypes could be actuated.

4.3. Material candidates and selection

4.3.1. Material for the SMA

Among the different families of shape memory materials reported during the literature review, shape memory alloys have demonstrated to be the ones exhibiting the best balance of structural integrity and recoverable strain [1-11]. Out of all commercially available alloys, near-equiatomic nickel-titanium (NiTi) is often used due to its ductility, fatigue strength and corrosion resistance [7]. Although alternative SMA systems, such as Cu-based and Fe-based alloys, have been investigated for actuator applications [68], NiTi remains the most mature and extensively characterized material with the highest accessibility of all.

One of the main reasons for selecting NiTi is the extensive body of scientific literature available regarding its thermomechanical behavior. The transformation temperatures, stress-strain response, fatigue performance –although still being extensively researched [65]–, and constitutive models of NiTi have been studied for several decades, resulting in well-established design methodologies and reliable material data. This considerably reduces the uncertainty associated with predictions and experimental validation, something valuable as it will allow to better forecast the behavior of the actuator with greater confidence.

From a practical perspective, NiTi is also the most commercially available SMA. It is widely produced in the form of wires, springs, tubes, and sheets with well-controlled compositions and transformation temperatures, making it readily accessible for short-term research and fast prototyping. Compared to less established SMAs, NiTi already has standardized manufacturing methods established and a broad supplier network in Europe. This is highly valuable when facing a project that needs immediate application and industry-standard reliability.

Finally, the selection of NiTi was also motivated by the context and scope constraints of the present work. To develop or properly characterize alternative SMA compositions would signify work and efforts that are not aligned the objectives of this thesis, as the primary aim is the development of a functional mechanism to shield and expose satellite optics. Therefore, the use of a well-established material with predictable behavior was the preferred option to allow the work to focus on the design, optimization, and integration of the actuation mechanism rather than on the development of the SMA itself. Considering its excellent functional performance reported in numerous studies and practical applications [2, 4-14, 17, 18], available industrial use, and relatively high level of technological maturity among other SMA alternatives, NiTi was considered the most suitable shape memory alloy for the proposed application.

An important advantage of NiTi over many other shape memory alloys is that its transformation temperatures can be tailored over a relatively wide range through careful control of both chemical composition and thermomechanical processing. This flexibility allows the material to be adapted for specific operating conditions. For actuator applications, the austenite finish temperature (A_f) is particularly important [1], as it determines the temperature above which the material has fully recovered its parent austenitic phase and where is thus capable of generating the desired actuation force.

The transformation temperatures are highly sensitive to the Ni/Ti atomic ratio [16]. Even small deviations from the equiatomic composition can produce significant changes in the transformation behavior, as seen in Figure 4.4. In general, increasing the nickel content shifts the transformation temperatures to lower values, whereas titanium-rich compositions increase them –always inside a general range between -130°C and up to 110°C for non-HTSMAs. This sensitivity originates from changes in the stability of the parent austenite phase and explains why the composition of commercial NiTi alloys is typically controlled within only a few tenths of an atomic percent [1]. Consequently, manufacturers are able to supply NiTi components with transformation temperatures tailored to the intended service conditions without substantially altering the overall mechanical properties of the alloy.

Besides composition, thermomechanical processing also plays an important role in determining the temperature of response of NiTi alloys. In the work conducted by Zhu et al., the authors demonstrated how ageing treatments can promote the formation of intragranular precipitates that increase in size with aging duration and increase the temperature of tha alloy's phase transformation noticeably. Furthermore, solution

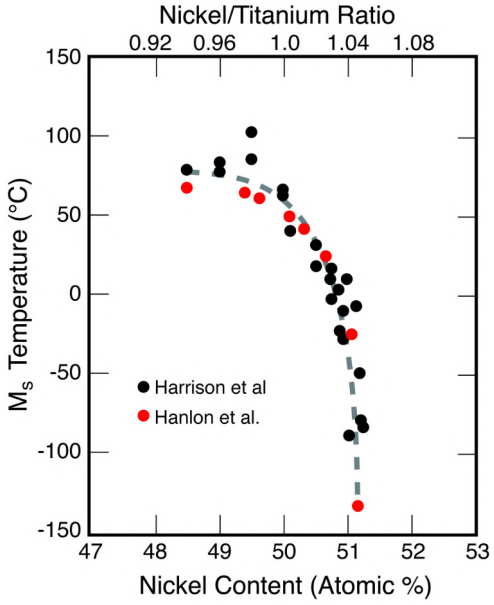


Fig. 4.4 | Effect of nickel content to the start of martensite transformation temperature. NiTi alloys are highly sensitive to the nickel/titanium ratio, allowing to tailor the transformation temperature by varying the alloy's chemical composition. [source: public domain]

annealing was found to be the heat treatment with the highest effectiveness in increasing the transformation temperature. Such treatment was conducted on as-fabricated nitinol and it even increased the one-way shape memory effect (OWSME) degradation resistance dramatically [55]. The authors explain how thermomechanical processing such as solutionized annealing eliminates atomic-scale defects (voids, dislocations) which typically inhibit martensite phase transformation, effectively rising the transformation temperatures. Additionally, the dissolution of titanium within the NiTi matrix causes a decrease in the Ni/Ti atomic ratio, hence increasing M_s as in Figure 4.4. It is also mentioned how these heat treatments can dissolve metastable Ti particles into the NiTi matrix, further reducing the quantity of atomic defects.

Two different NiTi wires were ordered from two different suppliers. Since it was important that the transformation temperature was as high as possible given the operating conditions of the mission, the highest available Af were selected. Table 4.1 shows the characteristics of the SMAs available for this work. Special attention must be given to the force of the wires when heated as it defines the maximum allowable activation force of the bistable mechanism.

Table. 4.1 | List of available NiTi SMAs for the project. G.RAU GmbH is preferred for its F_{max}.

Suplier	Martensitic Force - F_{min} (N)	Austenitic Force - F_{max} (N)	A_f (ºC)
G.RAU GmbH	0.64	2.00	90
DYNALLOY Inc.	0.55	1.37	90

4.3.2. Material for the bistable mechanism

Material selection is one of the most important aspects in the design of compliant bistable mechanisms. Because compliant systems rely on elastic deformation rather than rigid-body motion, the material itself effectively acts as a functional component of the mechanism. Consequently, material properties directly influence performance, durability, actuation force, fatigue resistance, and environmental stability. A commonly used metric for evaluating materials intended for compliant applications is the ratio between strength and elastic modulus [47], also known as the yield strain. Materials possessing a high strength-to-modulus ratio can undergo larger elastic strains before yielding, enabling greater deformation without permanent damage [46]. Such materials are generally preferred because they maximize achievable displacement while maintaining structural integrity.

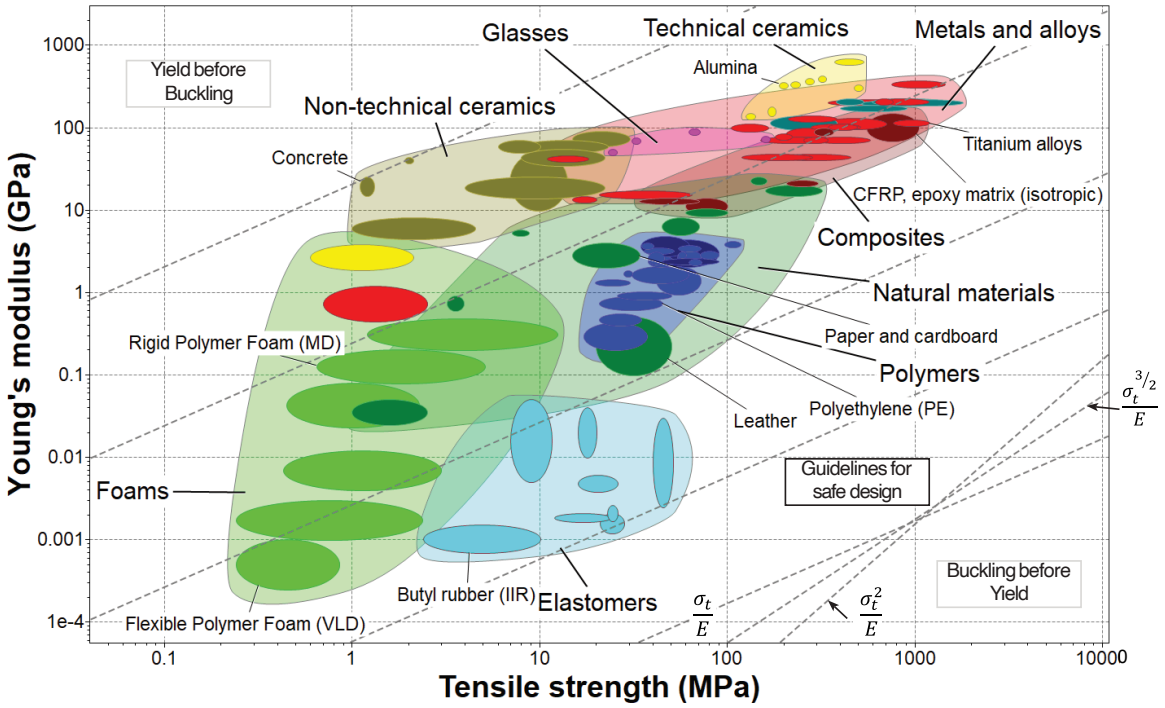


Fig. 4.5 | Young's modulus vs tensile strength chart. Higher strength-to-stiffness ratio is desired in compliant bistable mechanisms. While polymers are great candidates, they lack properties such as resistance to high temperatures, UV-radiation stability, and low CTE. [chart: Ansys Inc.]

The coefficient of thermal expansion (CTE) represents another critical parameter [47], particularly in aerospace applications. Thermal fluctuations in orbit can produce substantial dimensional changes that alter the force-displacement response of a compliant mechanism or introduce undesirable stresses. Materials with low thermal expanson coefficients are therefore advantageous because they provide greater dimensional stability across a broad temperature range.

Conventional engineering polymers are frequently used in laboratory prototypes primarily due to their low cost, ease of manufacturing, and high elastic strain limits. Materials such as nylon, ABS or PLA can achieve large reversible deformations that would be difficult to obtain in many metallic systems [21]. However, their relatively low strength and stiffness often limit their use in structural applications. Furthermore, polymer degradation can become a significant concen in space. Exposure to ultraviolet radiation, atomic oxygen, vacuum conditions, and extreme thermal cycling [20, 21] may result in embrittlement, outgassing, dimensional instability, or deterioration of mechanical properties over time [47]. As a result, although polymer-based compliant mechanisms are valuable for proof-of-concept studies and applications in Earth, their suitability for space deployment may be limited especially when compared to their metallic counterparts. This, together with the notably higher accessibility of polymers with 3D printing technologies and the limited time and budget, are the main reason why, in this work, an additively manufactured polymer will be used as the early-stage concept validation.

While metals offer higher strength and improved environmental resistance, they also exhibit lower elastic strain limits. For compliant aerospace structures, among a broad field of metallic materials options, titanium alloys, amorphous metals, and nickel-based alloys have received the most attention [44-46].

Titanium alloys are particularly attractive due to their favorable combination of high specific strength, corrosion resistance, and relatively low density, and because of this they have been largely used in structural applications for aerospace engineering. Merriam et al. demonstrated the possibility of creating sound bistable compliant mechanisms using 3D printed titanium parts. Though having proved the potential for applicability, it is also stressed that manufacturing-induced defects must be carefully considered. Electron beam melting (EBM) and other powder-bed fusion processes inherently produce a certain degree of porosity, especially near free surfaces. A study by Wooter and Denis reported that fully dense material is typically found only beneath a shallow surface layer, while thinner sections such as compliant flexures may consist almost entirely of material affected by surface-connected pores. Although according to Merriam these micropores generally have a limited influence on short-term tensile properties, surface roughness and micro-crack initiation sites can substantially reduce fatigue life. This issue is particularly relevant for compliant mechanisms, given that its operation relies on repeated elastic deformation of slender flexural elements. Nevertheless, this fatigue-related drawback can be significantly improved using hot isostatic pressing (HIP), as investigated by Qu et al., as it is able to eliminate a significantly large proportion of the internal microvoids present in as-printed alloys, leading to substantial improvements in fatigue resistance. Qu's results indicate an increase in fatigue strength of approximately 42% following HIP treatment, highlighting the detrimental role of microvoid formation in additive manufacturing and their role in crack initiation and propagation.

An important benefit of 3D printing is the reduced material waste associated with near-net-shape fabrication. Conventional manufacturing processes that use subtractive techniques (e.g. machnining) frequently remove large amounts of material from a bulk workpiece, generating substantial scrap waste. In contrast, since additive manufacturing deposits material only where required, it enhances material utilization and potentially reduces environmental harm. This advantage becomes increasingly relevant when high-cost aerospace alloys are used.

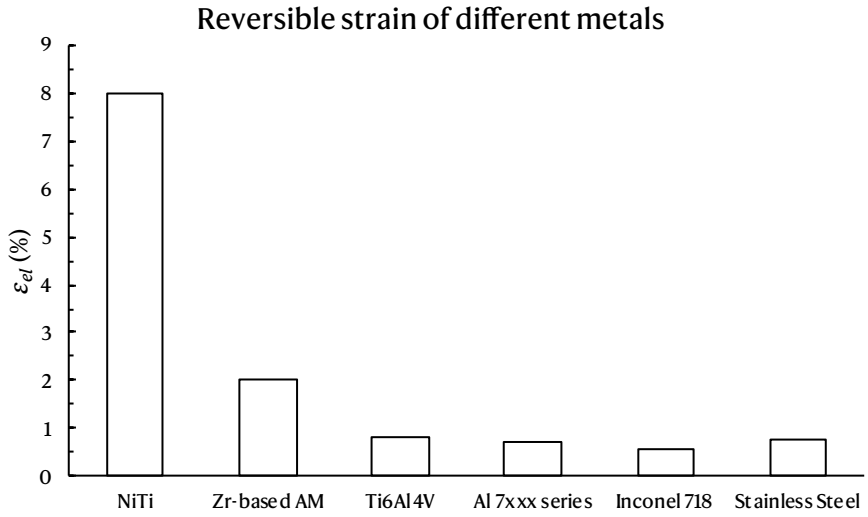


Fig. 4.6 | Comparison of the recoverable strain of various metals. NiTi alloys can achieve up to four times larger reversible strains than amorphous metals (AM), whereas the latter are able to elastically deform more than twice compared to their crystalline counterparts.

More recently, amorphous metals, also commonly referred to as bulk metallic glasses (BMGs), have emerged as a particulalry attractive class of materials for compliant mechanisms and precision engineering applications [44, 49]. Unlike conventional crystalline alloys, BMGs possess a disordered atomic structure with no long-range crystallographic order. The absence of dislocations as the dominant deformation mechanism results in exceptionally high yield strengths while maintaining an elastic strain limit of approximately 2% [47], several times greater than that of most engineering metals. Because of this, BMGs offer one of the highest strength-to-elastic-modulus ratios among structural metallic materials, making them especially well-suited for components that rely on large reversible elastic deformation [49].

Hofmann and Agnes describe BMGs' thermoplastic-like formability as one of the most distinctive characteristics of bulk metallic glasses. Since these alloys have low melting temperatures, they soften in a manner similar to highly viscous polymers and allow the fabrication of intricate geometries using molds, achieving very high dimensional accuracy and surface finish. Other studies have successfully demonstrated compliant mechanisms manufactured from BMGs, some also exhibiting bistability, highlighting their ability to store large amounts of elastic energy while remaining entirely within the

elastic regime [44, 49]. Nevertheless, their relatively high material cost and limited commercial availability currently restrict their widespread industrial adoption.

Shape memory alloys, particularly near-equiatomic NiTi, represent another promising family of materials for compliant bistable systems: although this time not for their shape memory properties but rather for their unusual superelastic behavior. This unique pseudoelastic martensitic transformation enables recoverable strains of up to 8%, significantly exceeding those achievable in conventional metallic alloys. As mentioned in previous chapters, SMAs have been quite extensively investigated for morphing structures and deployable mechanisms for aerospace, or in biomedical devices and vibration damping systems, however its research is significantly more focused on their shape memory effect rather than on their superelasticity –reason being their claimed low fatigue strength [16].

The three metallic material families discussed above each present distinct advantages for compliant bistable mechanisms. Titanium alloys provide a very interesting balance between specific strength, environmental resistance, and technological maturity. Bulk metallic glasses offer excellent strength-to-stiffness ratio and high energy storage capabilities thanks to their amorphous structure, while superelastic SMAs should be ideal considering their ultralarge recoverable strains. To figure out which is the material of choice, testing will be conducted and the results will be analyzed side by side.

4.4. Finite element modelling of the bistable mechanism

The modeling of compliant bistable mechanisms remains a formidable challenge due to the strong nonlinearities associated with post-buckling deformation and snap-through instability [50]. Unlike conventional structures, the excessively large displacements and geometric instabilities that bistable mechanisms undergo during operation results in a snap-through behavior that cannot be accurately captured using linear approaches. Furthermore, the existence of multiple equilibrium positions introduces additional complexity into the numerical solution process [53]. Previous studies have demonstrated the effectiveness of non-linear finite element methods for predicting the force-displacement response, stress distribution, and stability characteristics of bistable mechanisms [32, 33, 35, 44-46, 51].

4.4.1. Setup of the nonlinear numerical model

Finite element simulations were performed using the Abaqus software. The objective of the numerical study was to optimize the geometry of the bistable beam while evaluating the suitability of the three candidate materials identified in the previous chapter: Ti-6Al-4V, a zirconium-based amorphous metal (ZR01), and superelastic Nitinol. The geometric

parameters that were investigated included the beam's vertical and horizontal lengths, the initial inclination angle, and cross-sectional dimensions. These parameters are known to strongly influence the bistable response, activation force, achievable displacement, and stress distribution within compliant mechanisms [33].

To reduce computational cost, the mechanism was modelled using a two-dimensional wire geometry rather than a full three-dimensional model. Additionally, geometric symmetry was applied to the X-axis. This approach significantly reduced the number of elements required while maintaining sufficient accuracy for comparative design studies. The simplified model was also advantageous given the node limitations associated with the Abaqus Academic version.

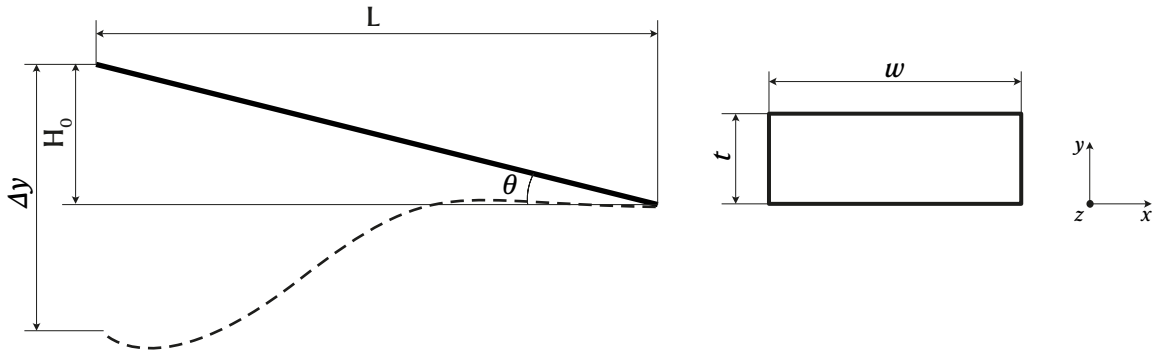


Fig. 4.7 | Model of the beam with geometrical variables. On the left, the beam with its starting position (solid line) and deformed second equilibrium state (dashed line). On the right, the cross-section of the beam. L is horizontal length, H_0 is the shuttle's height (height of the moving node), θ is the angle of the beam with the X-axis, Δy is the total displacement, t and w are the thickness and widht of the cross-section, respectively.

The initial finite element model reproduced the geometry of the experimentally validated prototype. Subsequently, the dimensions were progressively modified to obtain a more compact design suitable for integration within the available space envelope of the final instrument.

Capturing the snap-through instability of a bistable mechanism requires a geometrically non-linear solution process [51, 59]. Conventional static analyses are generally unable to follow the equilibrium path through unstable regions and therefore fail to predict bistable behavior correctly [50]. For this reason, the Static Riks method available in Abaqus was employed. The Riks algorithm is specifically designed to track non-linear equilibrium paths and is commonly used for problems involving buckling, snap-through instabilities, and post-buckling behavior [59]. The method introduces a load proportionality factor (LPF), allowing the solver to continue tracing the structural response even after passing limit points where traditional force-controlled approaches

would diverge. The interested reader is referred to [59] to find further detailed information on the Riks method in Abaqus.

The NLGEOM option was activated for all simulations in order to account for large deformations and noticed geometric non-linearities. The function of this setting is to update the structural stiffness throughout the analysis as the geometry changes. Without this formulation, stresses and displacements would not be accurately predicted, particularly near the snap-through region where the largest changes in geometry occur.

Several preliminary simulations were required to calibrate the numerical procedure. Parameters such as the initial increment size, maximum increment size, and load proportionality factor limits were adjusted iteratively until stable convergence and consistent results were obtained.

4.4.2. Material definition

The primary purpose of the simulations was to compare the mechanical response of the candidate materials under identical geometric and loading conditions. The final material selection was based not only on the force-displacement response but also on the resulting stress and strain levels generated during snap-through.

Titanium alloy Ti6Al4V and ZR01 amorphous metal were modelled as isotropic linear elastic materials with elastic moduli of 114 GPa and 87 GPa respectively. Their yield strengths and maximum strains were defined as 880 MPa for Ti6Al4V and 1.6 GPa for ZR01, and 0.8% and 2% respectively. All data was obtained from well-regarded open access material databases such as MatWeb [70]. The parameters used are presented in Table 4.2.

The modelling of NiTi's pseudoelastic properties was less straight forward, as nonlinearities coming from material behavior itself needed to be accounted for on top of the geometric ones. To capture a realistic response, the program's superelastic built-in model was used. This constituve model is fundamentally rooted in the generalized plasticity theory framework that was originally developed by Ferdinando Auricchio in 1997, which is the generally accepted model used for the FEA simulations of NiTi alloys [71]. Since the mechanical response of NiTi alloys changes based on processing conditions, chemical compositions, and ambient temperatures, the input parameters, found in Table 4.3, were extracted from recent literature reporting reliable typical-use data following NiTi's medical grade standards [66-68], a criterion that also applies to the majority of NiTi suppliers.

Table. 4.2 | Material properties used in the FEA. Obtained from supplier datasheets and [70].

Material	σ_y (MPa)	E (MPa)	ε_{el}	Poisson ratio
ZR-01	1600	87000	0.020	0.35
Ti6Al4V	880	114000	0.008	0.34

Table. 4.3 | Material properties used in the superelastic NiTi FEA. Based on [66-68].

E_A (MPa)	E_M (MPa)	ε_{trans}	$\sigma_{end\text{-}loading}$ (MPa)	$\sigma_{end\text{-}loading}$ (MPa)	$\sigma_{start\text{-}unloading}$ (MPa)	$\sigma_{end\text{-}loading}$ (MPa)	Poisson ratio
60000	20000	0.057	420	500	150	115	0.33

4.4.3. Boundary conditions and loading

The boundary conditions applied to the model are presented in Figure X. The right end of the beam was constrained using an encastre boundary condition, representing a fully fixed support. The opposite end was constrained in the horizontal direction while remaining free to move vertically. This configuration reproduced the kinematic behavior of the physical mechanism while maintaining symmetry within the model.

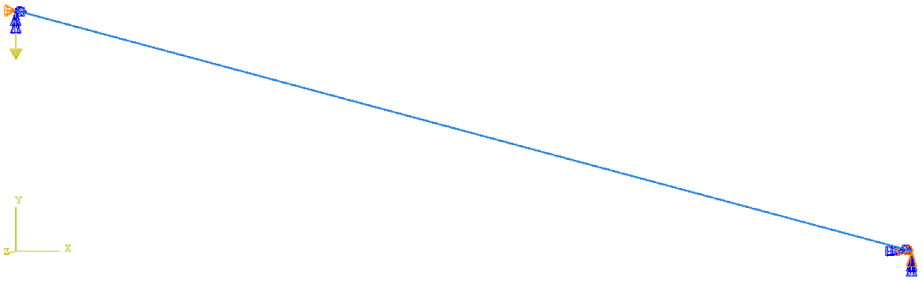


Fig. 4.8 | Applied boundary conditions and loading in the FEA model. The left node is constrained with an X-axis symmetry, having a single DOF in the U2 space, and a downward force of 1 unit to indicate the direction of motion. The right node is fully fixed with an encastre BC.

A small unit load was applied in the downward direction at the movable node. As the Riks method uses the load magnitude as an unknown variable [59], the purpose of this load was simply to indicate the desired initial direction of deformation and facilitate convergence of the non-linear solution. Therefore, the analysis was essentially a displacement-controlled simulation.

During the simulation, the program was told to automatically compute the reaction force at the moving and fixed nodes through the load proportionality factor. Simultaneously, the vertical displacement of the traveling node was recorded. These outputs enabled the plotting of the characteristic force-displacement curves (Table 4.1-A) describing the complete bistable response of the mechanism.

4.4.4. Design optimization criteria

The force-displacement curves obtained from the simulations were used as the basis for the optimization process. Particular attention was given to the characteristic N-shaped

response associated with bistable mechanisms, ensuring the deformation produced negative force values corresponding to the transition to a second equilibrium state.

An effective bistable design was considered to be one that exhibited a clear snap-through event, sufficient displacement to satisfy the minimum aperture requirements of the system, and a force to activate the bistable transition falling within the constraint range. This last one, recorded as the reaction force in the Y axis, became one of the principal design indicators during optimization as it had to be compatible with the actuation force of the selected SMA wire.

In addition to bistable performance, the structural integrity of the mechanism was evaluated through stress and strain analysis. Von Mises stress values were extracted for every single node throughout the deformation process to identify the critical regions and verify that stresses remained below the yield strength of the materials. True strain was also monitored during the simulations. Although yield criteria are typically formulated in terms of stress, strain provides a direct measure of local material deformation and can be particularly useful when evaluating highly compliant structures undergoing large deflections [54]. For this reason, strain was used as an additional verification parameter to ensure that local deformation levels remained within the allowable elastic limits reported for each material.

Chapter 5

Results

This chapter presents the results obtained from the finite element analysis simulations together with the validation of the computational model through experimental tests with physical prototypes. The subsequent Chapter 6 will examine the findings in more detail, discuss their relevance, and provide clues in regards to the potential improvements for future work.

Overall, the FEA simulations examined the effect of geometrical variables and material properties to the bistability of the system. The main parameters of interest will be the snap-through force (or activation force); being the force needed to trigger instability to the mechanism and make it transition into its second equilibrium state, the displacement value at the second stable position; namely to ensure the shutter is able to move sufficiently to achieve the minimum aperture, the stresses in the material; to validate the integrity of the mechanism, and finally the strains; which were additionally monitored because large-deflection compliant structures are prone to exhibiting highly localized deformation, therefore it was considered a relevant complementary measure to stress when assessing whether the material remained inside its elastic operating regime.

Table. 5.1 | Requirements to ensure the compliance with the target application. A force under 2 N is necessary for the shape memory nitinol to actuate the shutter, and above 0.09 N should be sought to avoid unexpected trigger due to random loads. A displacement of 11 mm or more is mandatory to comply with the minimum aperture. A minimum safety factor of 1.5 is decided considering the intended use of the part.

Parameter	Force (N) - F	Displacement (mm) - Δy	Safety Factor
Condition	$0.09 \leq F \leq 2$	≥ 11	≥ 1.5

A subset of 26 specimens was modelled to assess the shutter's global bistable behavior. The three candidate materials, Ti6Al4V, ZR-01 (AM), and NiTi, were compared side by side. Three different beam dimensions were defined according to the maximum vertical and horizontal measurements of the instrument. The simulations started with the longest version of beam to guarantee the existance of a bistable behavior, and then the size was subsequently reduced with the objective of finding the smallest possible beam that adhered to the force-displacement requirements.

A total of 8 different cross-sections were modelled and evaluated. A similar approach to the general beam dimensions was used for varying the cross-sections. All materials started with a beam width of 1 mm, which was reduced to as low as 0.6 mm for some materials. This width was selected because it adapted well to the available space inside the VEM. The thickness values were chosen after multiple attempts at achieving a proper bistability curve, as well as after conducting a thorough market search and supplier talks. The only supplier that could provide the amorphous metal (Heraeus Amloy GmbH) expressed a that a minimum thickness of 300 microns was achievable with their technology. For titanium, as sheet formats are available as thin as 50 microns or less, the minimum thickness was until the activation force went below the minimum threshold condition found in Table 5.1. This bottom threshold was defined as follows: considering that maximum peak accelerations of unmanned space missions (such as ULA's Vulcan Centaur or SpaceX's Falcon Heavy) are typically capped at around 3 G's, and knowing that the weight of the bistable mechanism's shuttle is around than 3 grams, we can approximate the minimum activation force that the mechanism should have in order to prevent unwanted activation.

$$a_{max} = G_{level} \times 9.81\ m/s^2 \tag{5.1}$$

Having the acceleration, the peak inertial force due to vibration can be determined:

$$F_{vib} = a_{max} \times m \tag{5.2}$$

Which results in a minimum activation force of 0.088 N in both directions.

In the case of superelastic nitinol, the available sheets in the market achieve thicknesses down to 100 microns.

Table. 5.2 | Geometric parameter combinations of modelled beams. Initially defined geometric parameters based on bistable behavor and selected materials.

Beam type	L (mm)	H_0 (mm)	θ (°)	w (mm)	t (mm)
Long	45	10	12.53		
Average	42.5	8.75	11.63	1 / 0.8 / 0.6	0.4 / 0.3 / 0.2 / 0.1
Short	40	7.5	10.62		

All presented specimens show a bistable behavior. Figure 5.1 shows the comparison of the three materials with exact same beam length and cross-sectional dimensions, which in that case correspond to the long beam with a 1x0.4 mm cross-section. It can be directly observed how the activation force is directly related to the material's stiffness, being titanium (E = 114 GPa) the one with the highest force, followed by the amorphous metal (E = 87 GPa) and finally superelastic nitinol (E_{M-A} = 20-60 GPa), with a force more than five times lower than ZR-01. This directly positions nitinol as the only material valid for the application with these dimensions. The displacement of 15.5 mm exhibited by all candiadtes is comfortably above the minimum for the application.

If the Von Mises stresses of the three materials are analyzed, the simulation tells us that titanium reaches stresses beyond the elastic limit, meaning its deformation would become permanent. This is also confirmed by the localized stresses in titanium, which go about 0.1% beyond its limit. The amorphous metal stays below yield thanks to its very high elastic limit and high deformation strains, something that already positions it as a better candidate than titanium if we consider they both had almost exactly the same localized strain. Regarding nitinol, on the other hand, due to its exceptionally high allowable deformation strain of 8%, it holds its integrity far from its elastic limit.

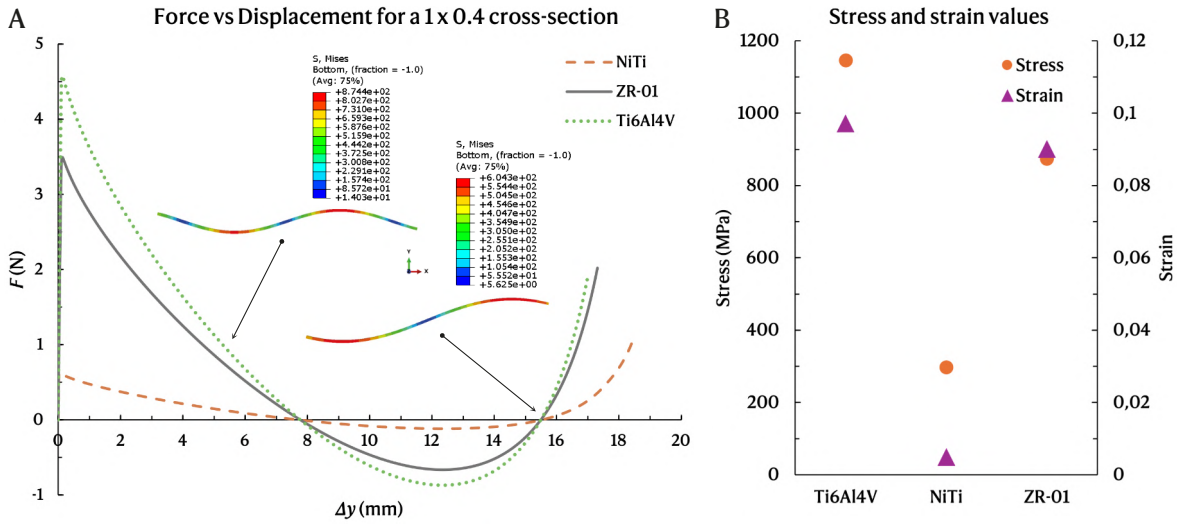


Fig. 5.1 | Force-displacement curves and maximum stress and strain for the three materials. Plot A shows the difference in activation and snap-back forces of NiTi compared with titanium and amorphous metal, though their unstable and total displacements remain exactly the same. Chart B shows how the stresses and strains are highest for titanium, which yields and fails to recover its deformation. On the contrary, NiTi and ZR-01 are able to stay below their yield stresses and strains, already demonstrating superior performance. All beams have the same L and H_0 of 45 x 10 mm.

It is remarkable, however, to observe that during that high deformation nitinol never used its superelastic properties. Figure 5.2-B corroborates that, when the martensite volume fraction (MVF) is analyzed, no part of the beam managed to transform its phase from austenite to martensite. This is a clear indicator that the real potential of superelastic niti-

nol is still not being used, demonstrating the clear superiority compared to the other two materials when it comes to a high-deformation compliant bistable application.

A visualization of the beam's deformation during the FEA is shown in Figure 5.1-A, in this case for the ZR-01, presenting the maximum stress during the snap-through transition and having a decrease at the second stable position. This aspect supports the validity of the model, as such behavior aligns with what is described in the literature [33, 44, 45].

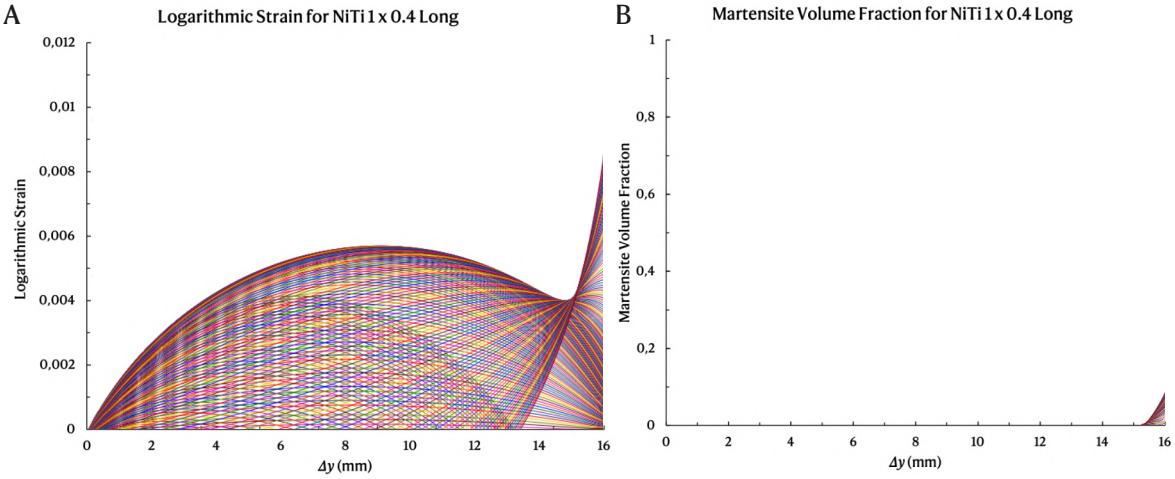


Fig. 5.2 | Strain and martensite volume fraction of NiTi. Figure A shows how the maximum strain is also during the instability transition as the stress, while B is an evidence of how the model did not reach sufficient strain for the microstructure to transform phases.

At the same general dimensions of 45x10 mm, the thickness of titanium and ZR-01 is reduced to find out whether they are viable solutions or not. At its minimum manufacturable thickness of 0.3 mm, ZR-01 becomes a viable option for the application. By reducing 0.1mm from its previous thickness, the activation force goes from 3.49 N down to 1.51 N, enough for the SMA to actuate it. The strains and stresses are also reduced noticeably, bringing its safety factor from 1.83 up to 2.45.

In Table 5.3-B it can be observed that reducing the thickness in titanium has naturally influenced positively as well. Since titanium can be rolled, thin sheets and foils can be made out of it. This provides thicknesses than cannot currently be achieved with 3D printing, which is the main available production method for ZR-01. For this reason, thinner versions are modelled with titanium in the simulations.

Although titanium's force for the 0.3 mm thickness is below the upper threshold, it remains too close to the SMA's available actuation force. Reducing the thicknesses to 0,2 mm significantly decreases the required force. At this cross-section, titanium provides the best balance with respect to the application constraints, as it maintains the required force within the target range while achieving a safety factor above 1.5. None of the other cross-section configurations in titanium satisfy both criteria simultaneously. While the

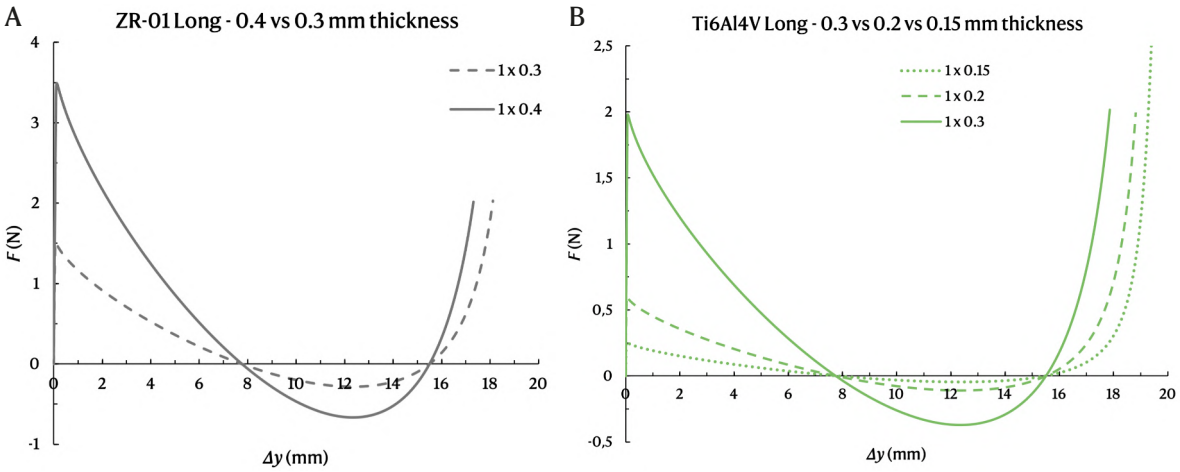


Fig. 5.3 | A. Thickness comparison of ZR-01 and B. Thickness comparison of Ti6Al4V . ZR-01's activation force is within range of actuation of the SMA when using a 0.3 mm thickness. On the right, Ti6Al4V has an optimal thickness of 0.2 mm, given that at 0.15 mm it is below minimum force (0.047 N) and at 0.3 mm the stresses are still too high, with a SF of only 1.03.

force of the 0.3 mm thickness can be lowered by decreasing the width w, the stresses and strains remain the same and represent a SF of only 1.03 (see Appendix B). A thickness below 0.2 mm is translated into a force that is not high enough, meaning there is a high risk of triggering the mechanism unintentionally due to vibrations or external loads.

When the general dimensions of the beam are reduced ("Average" and "Short" beams), the activation forces are slightly increased while the stresses and strains are mildly reduced. The greater force is given because of the lower slenderness of the beam when reducing the length L. The lower stresses and strains are thought to be due to the decre-

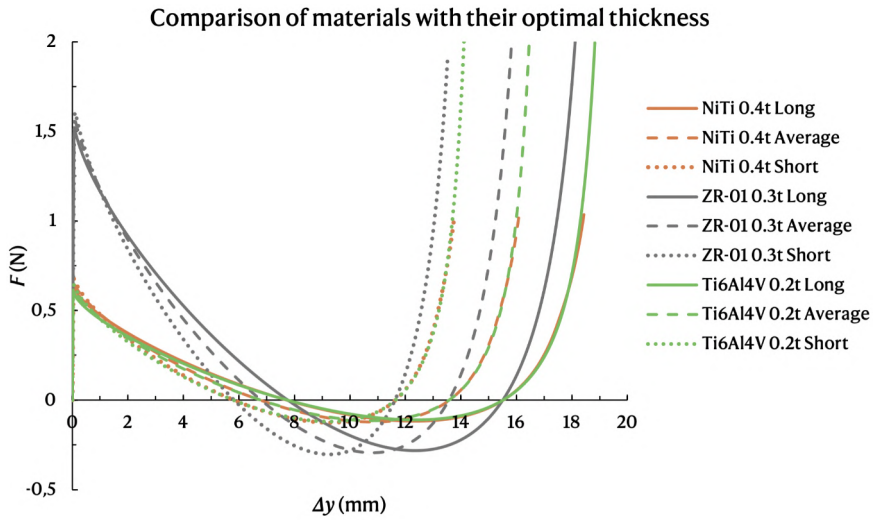


Fig. 5.4 | Beam length and material comparison with best-performing thicknesses . The thicknesses (t) that adhered to the requirements are 0.4 for NiTi, 0.3 for ZR-01, and 0.2 mm for Ti6Al4V.

ase of the angle θ, which, given that the displacement of the shuttle is also reduced, makes the beams deflect a shorter distance.

The FEA model still confirms that the nitinol has not undergone stress-induced phase transformation, even with the short beam. The results from Figure 5.4 are from the NiTi alloy behaving purely in elastic mode and it is nevertheless still outperforming the other two materials in terms of force and safety factor.

To use the true potential of the alloy's superelastic properties a new beam length was modelled, this time with dimensions L = 20 mm and H_0 = 7.5 mm, and cross-section of 1x0.4 mm. Something that can be directly observed from the resulting force-displacement curve, shown in Figure 5.5-A, is the significant increase in peak force. This is one thing that similarly occurred when reducing the lengths in the previous geometries. Another clear parameter that is now outside the frame of constraints is the displacement,

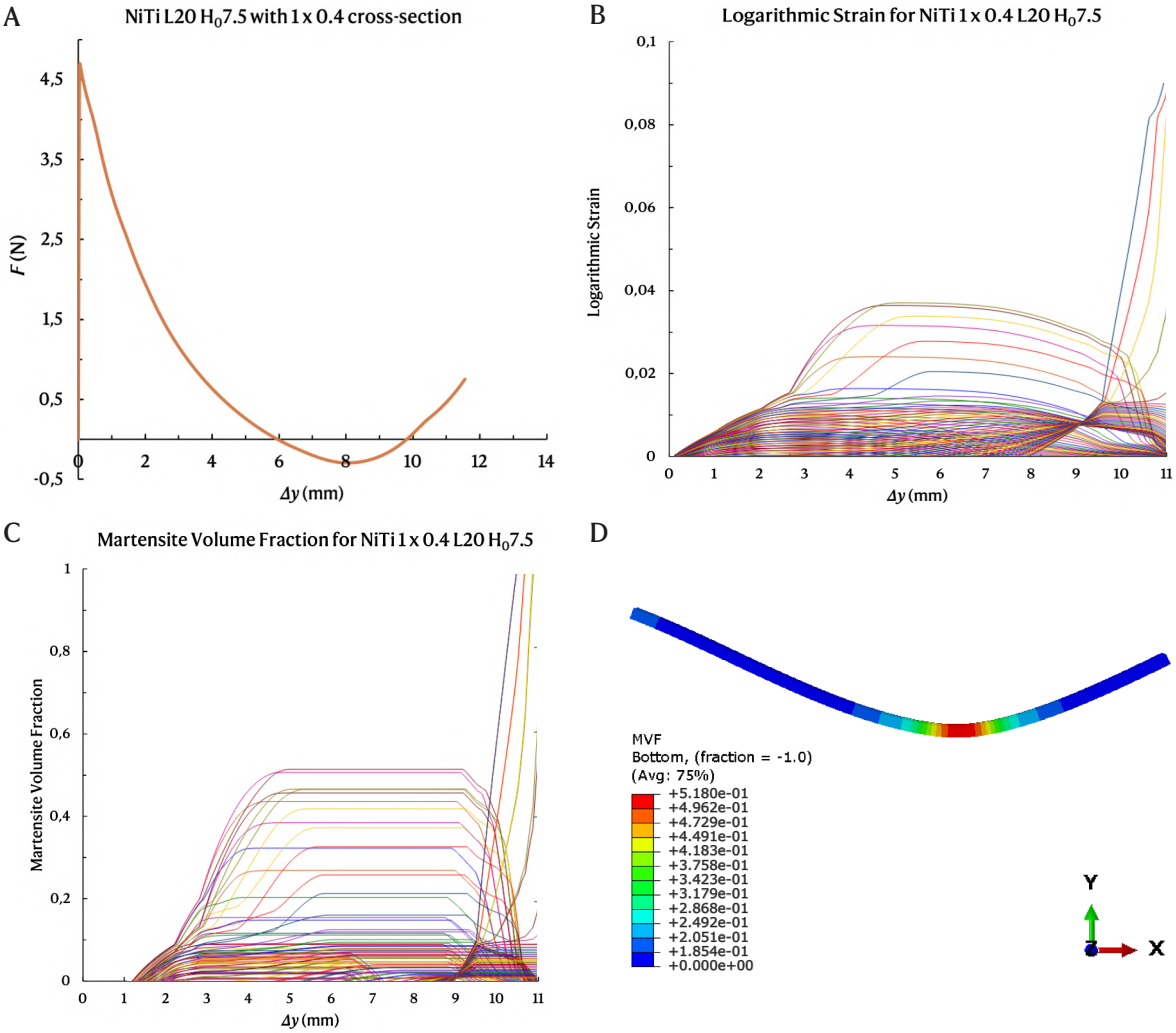


Fig. 5.5 | Behavior of the NiTi beam with 20 mm *L* and 7.5 mm H_0. Plot A shows the peak force is too high and the total displacement falls short. Plot B is the true strain, now reaching 3.7%, and C is the martensite fraction, which transforms in the location indicated in D a total volume of 51.8%.

which falls short at 9.74 mm. This occurred as a reason of decreasing the beam length L to less than half while maintaining a low height H_0.

This significant reduction of length accomplished triggering the martensitic phase transformation, as shown in Figure 5.5-C. Of the total microstructure, 51.8% experienced a transition from austenite to martensite through the application of stress, mainly in the middle region, as highlighted in red in Figure 5.5-D, where deformation was highest. It also occurred at the moment of snap-through instability, fulfilling the main purpose of using nitinol's superelastic properties in this application. The true strain in Figure 5.5-B presents a maximum of 0.037 or 3.7%, which also corroborates that the material would still be within the recoverable strain regime. The true strain (or logarithmic strain) is used instead of the engineering strain because the simulation involves large displacements, rotations and bending, and such high nonlinearities can only be captured by true strain [64].

An additional configuration with the same length, L, was modelled to obtain a second equilibrium state at minimum displacement of 11 mm while ensuring that the snap-through force remained within the actuation range. To achieve this, two geometric parameters were adjusted. The initial height, H_0, was increased, consequentially increasing the angle (θ) as well. Second, the thickness was reduced incrementally, first from 0.4 to 0.3 mm and then to 0.2mm, as the snap-through force at a thickness of 0.3 mm remained above the target range. As presented in Figure 5.6, these changes were successful, as the activation force was reduced to 0.67 N, the return force to 0.1 N which is still above the minimum, and the displacement extended to 13.01 mm. This version also harnessed the superelastic properties of the NiTi alloy, with a martensite volume fraction of 6.8% and a maximum strain of 1.27%.

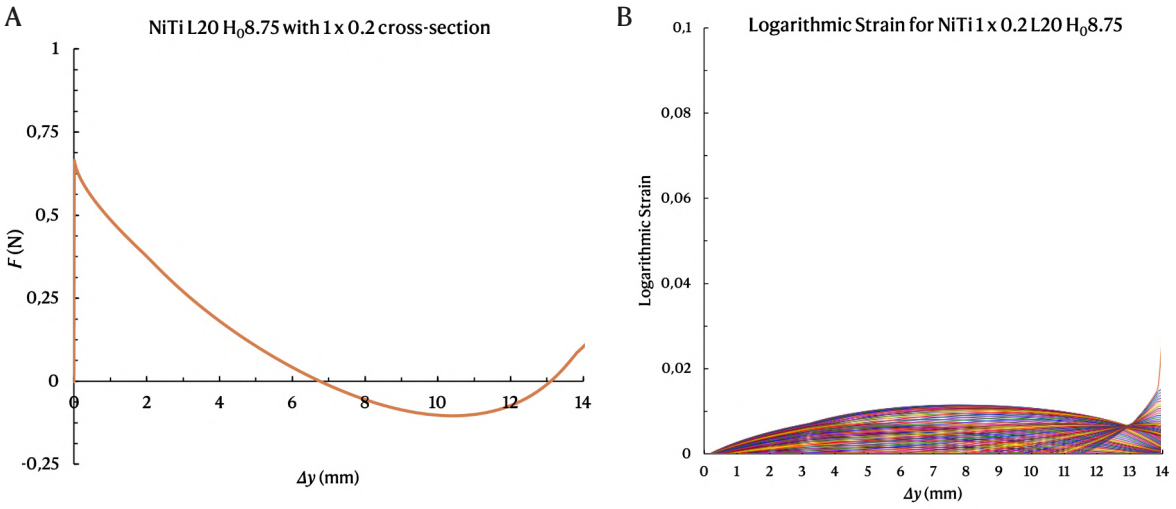


Fig. 5.6 | Behavior of the NiTi beam with 20 mm L and 8.75 mm H_0 with 0.2 mm thicknes. Plot A shows the force is now within range on both sides and the total displacement is sufficient. The true strain in B reaches 1.27%, well below the 8% theoretical limit.

Another interesting parameter to compare is the strain energy stored of each material during bending. This stored elastic energy is defined as the area under the force-displacement curve [63]:

$$U_b = \int_0^y F\, dy \tag{5.3}$$

Conversely, the derivative of the strain energy curve equals the force. With this, we can determine the bending strain energy of each material for a single geometry, observing how nitinol is more energy efficient considering the fact that it requires significantly less input work –over seven times less compared with titanium and over five compared with ZR-01– to achieve the same displacement Δy. This is also noticeable by the peak-to-valley difference, corresponding to the energy barrier needed to overcome to transition into a bistable or multistable state. The steepness of the energy curve tells the significant difference in activation force, with the flatter corresponding to a lower stiffness material.

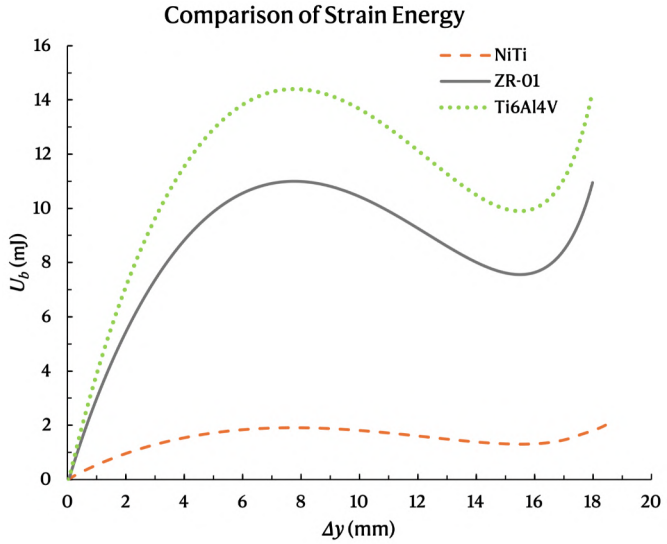


Fig. 5.7 | Energy comparison between materials. Represented is the strain energy (or potential energy) for the three material candidates for the same geometry and cross-section: L and H_0 of 45 x 10 mm, respectively, and cross-section of 1 x 0.4 mm.

To evaluate the validity and accuracy of the FEA model, an experimental test using rapidly available 3D-printed polylactic acid (PLA) prototypes was performed. The experimental results were later compared with simulations conducted using the same FEA model, this time incorporating PLA material properties, to quantify the deviation between the numerical predictions and the experimental response. This comparison evaluates the reliability of the model and determines whether the simulations performed for titanium, ZR-01, and superelastic NiTi accurately represent the expected behavior of the mechanism under real operating conditions or not. This time, two beams in parallel

were used to increase the low stiffness of PLA. This was naturally introduced in the simulations as well.

The tests were force vs displacement tests conducted using a constant controlled displacement test rig. The rotating motor responsible of the displacement was a Faulhaber 3242X024BX4 coupled with a 32L series linear actuator and a Faulhaber 5005 encoder. The force gauge had a precision of 0.1 N and a sample rate of about 100 counts/second. The speed of the shuttle was fixed at a constant displacement of 0.5 mm/s. The bistable samples were printed on a Bambulab X1 Carbon FDM printer using Bambulab standard PLA, which has a reported elastic modulus of 2580±220 MPa, and the fiber orientation was set along the length of the beam to ensure maximum bending resistance. To assess the effects of printing resolution, two samples with different resolution (rough and high-res) were printed, though results show no critical difference between the two. When comparing the experimental results with the FEA, the high-res sample will be used to reduce the effects coming from additive manufacturing imperfections.

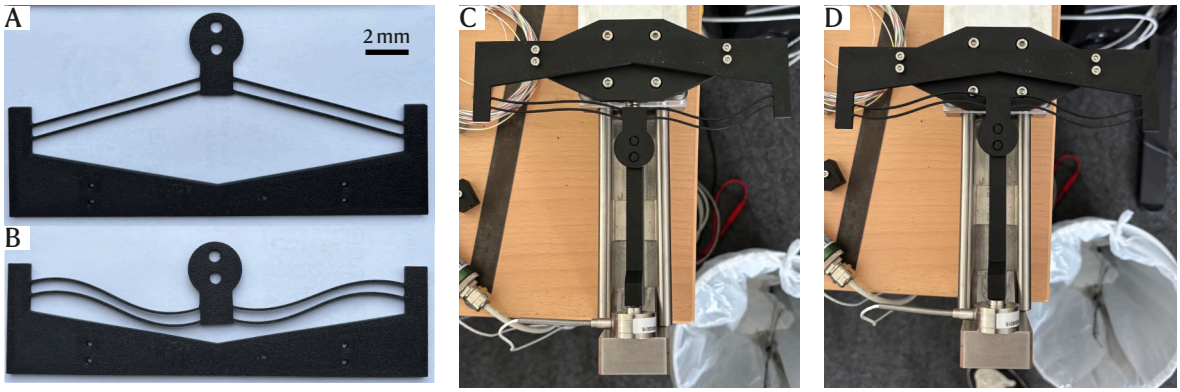


Fig. 5.8 | Experimental setup for the validation of the FEA model. In A, one of the PLA prototypes with beams fully extended (first stable state). In B, the same prototype in its second stable state. Image C shows the clear asymmetry between left and right deformed beams. Image D is the prototype in the testing rig after achieving the full displacement. A PLA with double-beams was modelled accordingly in Abaqus for the comparison with the experimental results.

The results, showcased in Figure 5.9, indicate that the model predicts the bistable response with a 11.9% error in activation force and a 3.35% error in displacement, which are the two main parameters of interest. Concerning the position of instability, although it is a parameter of no recognized significance for the application's requirements, it is worth mentioning the noticeable disparity of 24.56%. These deviations are primarily thought to be caused by three main experiment-related conditions:

1. The inaccuracy of the testing rig: the low-resolution load cell (0.1 N) magnified the deviation errors when compared to the high numerical precision output of the simulation. The asymmetrical response of the beams observed during testing, caused by the inexact boundary conditions of the rig, differ significantly from the idealized, symmetry-constrained computational model.

2. The lack of precise material data: the datasheet of the used PLA reports an XY-axis Young's modulus of 2580 MPa with a ±220 MPa deviation, making it a very rough value by which the high-sensitivity simulation is greatly affected.
3. The manufacturing route of the prototype: although the bistable behavior is a macroscopic phenomenon, the microscopic coarseness and small-scale defects (air voids, fiber misalignment, surface deformity) of consumer 3D-printing technologies can influence the mechanical response at the macro level.

To account for these factors coming from reality, a refinement to the model was made in an effort to reduce the deviation error of the three analyzed parameters but particularly focusing on optimizing the accuracy of the force and displacement values. This optimization was carried out after observing the asymmetries during the experimental tests (see Figure 5.8-C). This lack of symmetry can also be interpreted from all non-optimized force-displacement plots, such as Figure 5.9, where the activation force has an acute peak while the experimental data shows a more rounded transition. The sharp peak is an evidence of the extremely sudden change from increasing to decreasing force, typical from the beginning of buckling, which in reality is more progressive due to the inexistence of perfect symmetry and boundary conditions. To account for these imperfections, the straight geometry of the beam was changed for an arch to obtain a softer transition, a method adopted from the work of Shahsavari et al, which also delayed the displacement of the unstable state. In a similar study, Dunning et al. also employ the same technique of using a curved arch to better match the results of the simulation with the experiments when modelling a straight beam, considering it as adding an imperfection into the model. Additionally, the elastic modulus was tweaked within the ±220 MPa range to match the true stiffness of the actual material. The effects of 3D

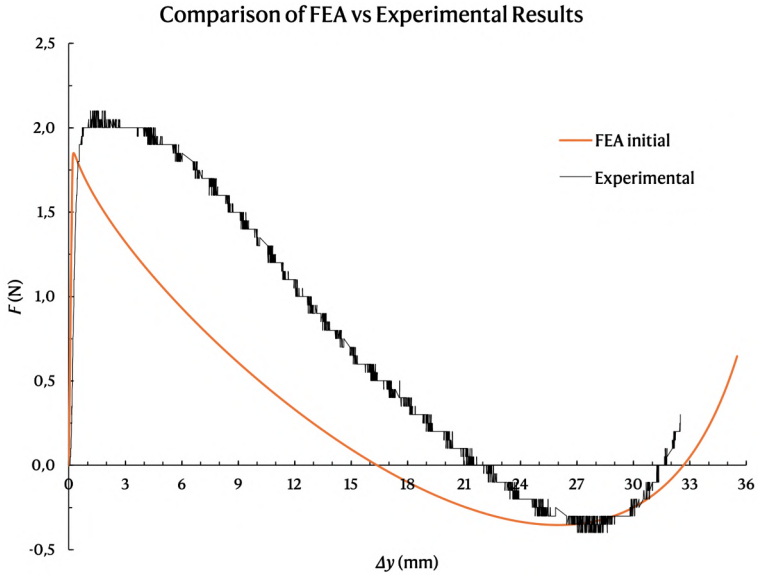


Fig. 5.9 | FEA vs experiment results. The model shows good agreement for the activation force, return force, and total displacement. Differences in curve shape arise from the idealized assumptions of the numerical model.

printing were not addressed in the simulation, therefore the model interpreted the beam as a perfect solid. The refined model showed a significant improvement over the initial version, with noticeably lower deviations for the main parameters of interest (F, Δy) and also for the instability displacement, Δy_u (see Table 5.3).

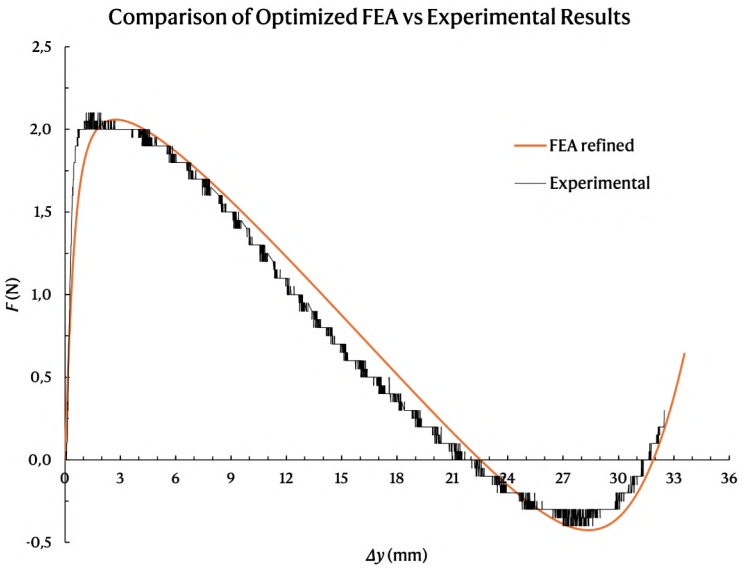


Fig. 5.10 | Optimized FEA vs experiment results. The refined model is able to account for asymmetries and other real-life imperfections, closely replicating the behavior observed in the experiment.

The deviation error of the FEA compared to the experiment is calculated as follows:

$$RE = \frac{(x_{sim} - x_{exp})}{x_{exp}} \times 100 \tag{5.4}$$

With x being the parameter to study.

Table. 5.3 | Deviations from the two different FEA models. The improvement of the refined model is significant in all parameters.

Model	F_{error} (%)	$F_{return\,\text{error}}$ (%)	$\Delta y_{u\,\text{error}}$ (%)	Δy_{error} (%)
Initial	-11.90	-9.53	-24.56	+3.35
Refined	-0.81	+4.98	+3.23	+1.09

From this FEA vs. experiment comparison, it can be deduced that the FEA values obtained for the metallic materials will most probably be translated into higher forces and slightly shorter displacement when tested experimentally. However, with the deviation values obtained for the initial model, this should not affect their validity as their force and displacement parameters would still be within the range of established requirements.

The completion of the study is concluded with the consolidation of all ideas into a single, assembled product. The conducted reseach has proved that the pseudoelasticity exhibited by equiatomic NiTi alloys is considerably superior in achieving the project's objectives than that of high-strength titanium alloys or amorphous metals. For the final design, NiTi's ability to undergo a microstructural transformation under stress is combined with its thermally-induced memory effect, obtaining the assembled shutter presented in Figure 5.11.

Regarding the selection of the ideal SMA, the forces obtained in the FEA for the chosen NiTi geometry (see Figure 5.6) must be properly aligned wih the SMA's actuation capabilities. To validate the functionality of the available SMAs, previously presented in Table 4.1, in synergy with the selected bistable geometry, inequation 5.7 must be fullfilled (note that these are only for one shuttle as the assembly is actuated symmetrically):

$$F_{close} = 0.67 + F_{min} \tag{5.5}$$

$$F_{open} = 0.1 + 2F_{min} \tag{5.6}$$

$$F_{max} \geq \text{Target force} \geq F_{min} \tag{5.7}$$

Where the 0.67 N is the obtained activation force in the closing direction, the 0.1 N is the return force (or the activation force in the opposite, opening direction), F_{min} is the martensitic force of the SMA (i.e. the deformation force when cooled), and F_{max} is the austenitic force necessary to open and close the shutter. The *target force* in the inequation refers to either F_{close} or F_{open}, depending on the scenario studied.

As presented in Table 5.4, both SMA are capable of actuating the shutter in both directions without being triggered by the counterforce of twinned martensite. If we consider the minimum force of 0.09 N defined in Table 5.1, then the DYNALLOY wire is a more suitable choice as the smallest force difference is above the aformentioned constraint. In contrast, the wire by G.RAU has a 0.03 N difference that could risk accidentally closing

Table. 5.4 | Validation of the feasibility for the proposed SMA-actuated bistable shutter. Both SMA candidates are feasible for the final assembly, as all target forces are within range. Note that F_{max} and F_{min} are twice the SMA's force when closing the shutter because two wires are employed.

Suplier	Action	F_{max}(N) - Austenite	Target force	F_{min}(N) - Martensite
G.RAU GmbH	Close	4.00	1.31 (eq. 5.5)	1.28
	Open	2.00	1.38 (eq. 5.6)	0.64
DYNALLOY Inc.	Close	2.74	1.22 (eq. 5.5)	1.10
	Open	1.37	1.20 (eq. 5.6)	0.55

the shutter in the case of heavy vibration or external loads. Therefore, the proposed assembly for the VEM shutter consists of a bistable mechanism incorporating superelastic NiTi flexures actuated by a SMA, whose force range varies from 0.55 N in the martensitic state to 1.37 N in the austenitic state.

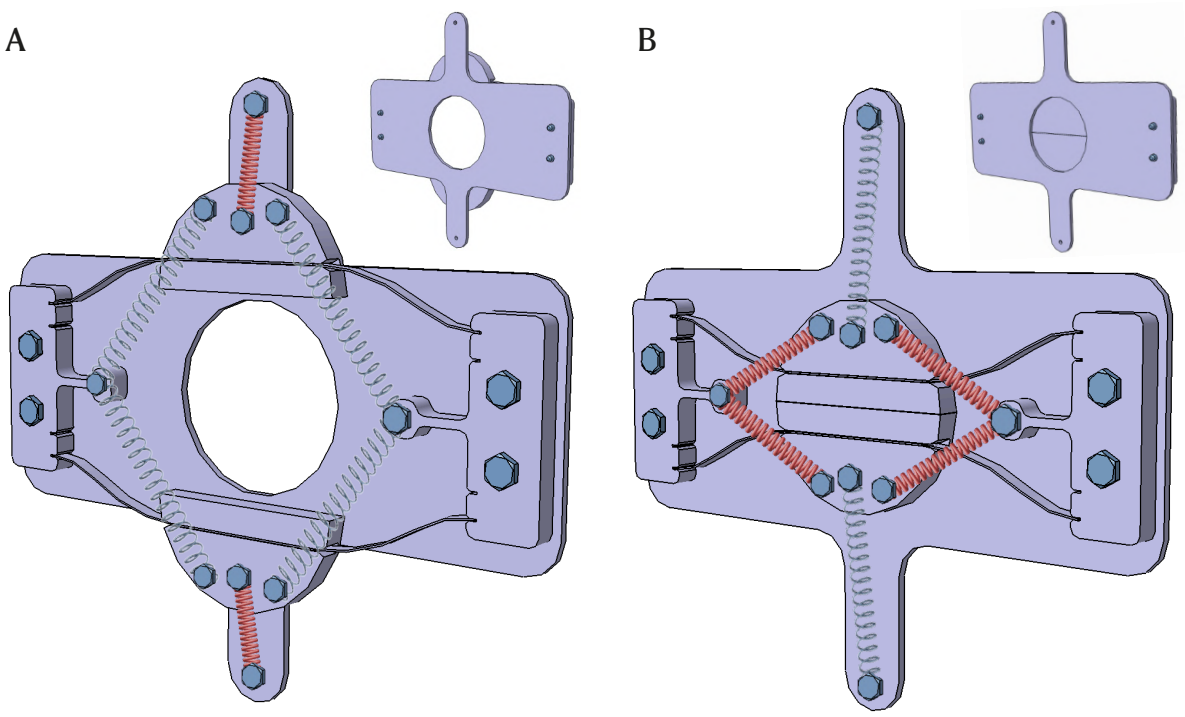


Fig. 5.11 | Final design proposal for the VEM shutter. The 3D model of the opened shutter is presented in image A, accompanied by a smaller image of the shutter's opened back view. In B, the shutter is presented in its closed configuration. The SMAs that must actuate to obtain either equilibrium position are highlighted in red, in reference to the heating of the wire. The superelastic NiTi flexures are inserted into slots to facilitate the manufcaturing and assembly. At the same time, such clearance allows for slight repositioning of the NiTi beams during actuation, reducing strains and stress concentration compared to a fully fixed part.

Chapter 6

Supplementary Design Proposal

A second proposal is briefly presented. This additional design was developed with the goal of providing a more industry-ready concept, offering higher reliability but less originality and experimental scope.

For this design, miniaturization and full-aperture displacement were the set objectives. Inspiration was drawn from the internal mechanism of ball-point pens, where a relatively large axial stroke is achieved within a confined volume through the use of springs and guided motion. This concept was considered advantageous for the present application because it enables performing a considerable displacement inside the compact housing of the VEM instrument, all while allowing the use of a single NiTi actuator. In contrast to the first proposal, which relied on antagonistic nitinol elements, this configuration employs one active nitinol wire working against a passive bias spring. Since actuation always occurs in the same direction, both for extension and retraction, the control and assembly of the nitinol is greatly simplified.

The initial implementation of this concept was developed for a half-aperture mechanism, covering only 50% of the window. Although mechanically feasible and dimensionally smaller, this configuration needed to be enhanced. The main reasons are because a full-aperture mechanism reduces the number of moving elements and therefore assembly complexity, eliminates potential misalignment between opposing covers, avoids incomplete closure that could permit stray light leakage, and lowers power consumption requirements because only a single nitinol element must be actuated. For these reasons,

the concept was further developed into a full-aperture design, which ultimately proved viable and small enough to fit inside the instrument's diameter.

The resulting mechanism consists of two parallel rails containing compression springs that interact with the assembly through a translating bush. The springs bias the system toward one of two stable positions, while the SMA element, when heated, provides sufficient force to overcome the spring load and shift the cover to the other stable position. Once the desired position is reached, the cover is held in equilibrium without further energy input, as the pushing spring force and the retention force of the guiding arm are balanced. Hence, the SMA is in both positions deformed and therefore always able to pull further to move the arm to restart a new cycle.

A critical design requirement for this nitinol-bias spring assembly is that the spring force must be strong enough to deform the nitinol wire when it is in its low-temperature (martensitic) state, yet sufficiently weak to be overcome when the wire is heated to its high-temperature (austenitic) state. The force ranges for the two nitinol wires evaluated are shown back in Table 4.1. Consequently, the spring system must operate entirely within these bounds during the full stroke of the mechanism. Because the force generated by a compression spring increases with compression, the spring geometry and arrangement can be tailored so that the force profile matches the nitinol force window.

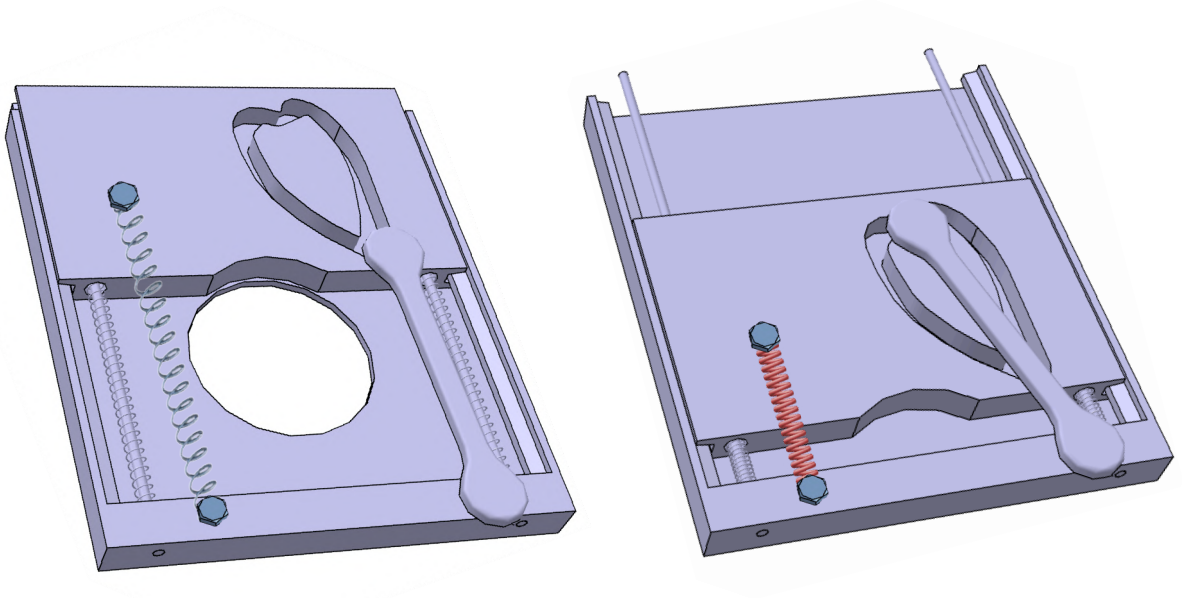


Fig. 6.1 | Second design proposal. The two stable states are presented (opened and closed). The SMA wire is heated to make the arm move into the second equilibrium position, guided by the sunken path. Once the current is stopped and the SMA cools down, the bias springs push and the cover is held by the arm. To open the shutter once again, the SMA is heated back up, the arm moves constrained by the path and is returned down to the initial stable position.

The assembly, as seen in Figure 6.1, incorporates two parallel spring rails, which doubles the force generated by a single rail. However, practical constraints arose from the physical dimensions of commercially available springs. Springs with longer free lengths exhibited larger mean coil diameters, which exceeded the internal diameter of the bush. To overcome this limitation while still achieving the required stroke, multiple shorter springs were stacked sequentially within each rail. This configuration increased the available deformation length without increasing the spring diameter beyond acceptable limits. Although springs are geometrically arranged in series, the housing architecture constrains them such that each spring undergoes the same axial displacement as the bush translates. Therefore, the system does not behave as an ideal series spring system in terms of equivalent stiffness. Instead, series stacking increases the available stroke while preserving the force–deflection behavior of each individual spring. If the extended bush length is denoted by L_{ext} and the number of springs in each rail by $n_{springs}$, the length of a single spring at the extended position is:

$$L_{e-spring} = \frac{L_{ext}}{n_{springs}} \tag{6.1}$$

and at the contracted position,

$$L_{C-spring} = \frac{L_{ext} - 27}{n_{springs}} \tag{6.2}$$

since the bush stroke is fixed at 27 mm. The forces generated by one rail are therefore,

$$F_{e-rail} = k\left(L_0 - L_{e-spring}\right) \text{ and } F_{c-rail} = k\left(L_0 - L_{c-spring}\right) \tag{6.3-6.4}$$

where L_0 is the unstressed length of the spring and k its stiffness constant. With two rails in parallel, the total forces exerted on the mechanism become:

$$F_{e-total} = 2\left(F_{e-rail}\right) \text{ and } F_{c-total} = 2\left(F_{e-rail}\right) \tag{6.5-6.6}$$

This model was verified through independent spreadsheet calculations and analytically, confirming that it accurately represents the physical behavior of the mechanism.

In order to select the optimal spring for this design, a constraint search problem can be formulated in terms of two discrete design variables: the extended bush length, L_{ext}, and the number of stacked springs, $n_{springs}$. For any candidate pair (L_{ext},$n_{springs}$), the spring lengths at both bush positions must remain between the unstressed length L_0 and the minimum admissible compressed length L_{min}. Simultaneously, the corresponding forces must remain within the Nitinol force window, namely above the minimum force in the extended position and below the maximum force in the contracted position.

Because these geometric and mechanical constraints are coupled and depend nonlinearly on both L_{ext} and $n_{springs}$, no direct analytical solution can be derived to

determine suitable combinations. The problem was therefore expressed as a discrete constraint satisfaction problem and solved computationally. Integer values of L_{ext} within the feasible geometric range and integer values of $n_{springs}$ within practical assembly limits were systematically evaluated. For each combination, the spring lengths were calculated, geometric feasibility was verified, and the resulting forces were computed using the validated physical model. Only those configurations satisfying all constraints were retained as admissible solutions. This procedure was implemented in Python as a simple deterministic search algorithm (the code can be found in Appendix C). For each candidate spring defined by its parameters (L_0 ,L_{min} ,k), the algorithm evaluates all possible configurations and determines whether a feasible design space exists. Springs for which no admissible combinations are found are conclusively rejected as incompatible with the mechanism. For springs that do yield compatible solutions, the script returns the minimum and maximum forces and provides the exact combinations of bush length and number of stacked springs that ensure compliance with both geometric and force requirements.



Fig. 6.2 | Actuation cycle path of the arm. The red lines indicate the path followed by the arm when the SMA is pulling in austenitic state. The green path refers to the pushing of the spring when the SMA is in martensitic state. The circles are the locations of the two stable positions.

Several spring types from the product catalogue of the German supplier Gutekunst Federn GmbH were evaluated as potential candidates. The selection of the optimal spring was primarily dictated by the geometric constraints of the assembly, in particular

the maximum allowable outer diameter imposed by the bush (≤ 3.1 mm) and the minimum feasible inner diameter imposed by the mandrel (≥ 1.0 mm). In addition to these spatial constraints, an upper limit on the admissible static spring force of 2 N was defined, based on the effective actuation range and force output capabilities of the available nitinol wire actuators. A preliminary screening based on these boundary conditions concluded that five spring geometries satisfied both dimensional and first-order mechanical feasibility criteria and were therefore kept for the following compatibility assessment. This set was later reduced to three valid configurations by the deterministic search algorithm, as shown in Figure 6.3.

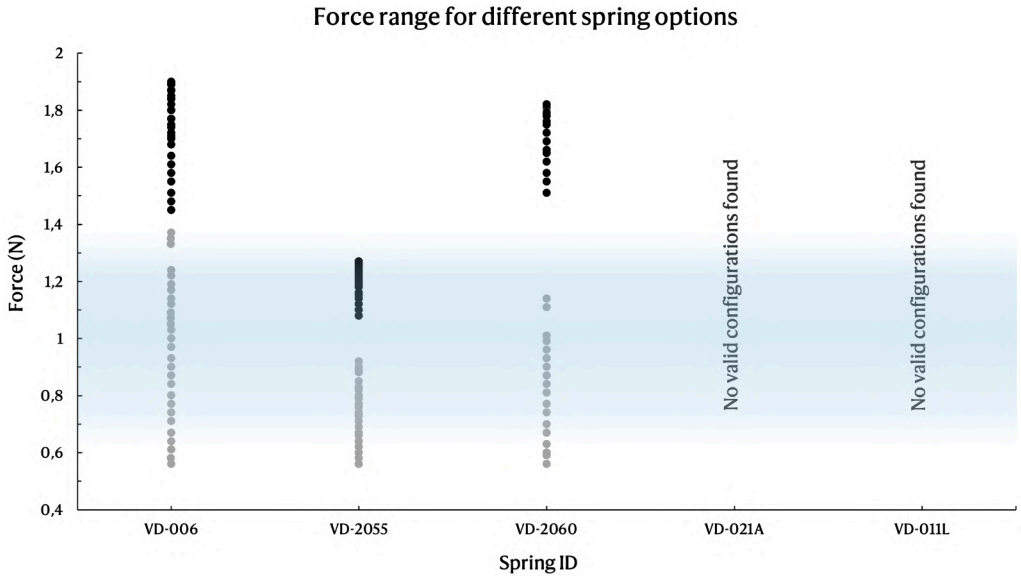


Fig. 6.3 | Compatible solutions found for the five selected spring geometries. Black markers correspond to maximum force (i.e. closed window cover) while gray markers are force values when the springs are only slightly compressed (i.e. opened window cover). The area of interest, in which compatibility for the two SMA types is found, is shadowed in blue.

Out of the three possible springs, model VD-006 returned a total of 28 valid solutions, with VD-2055 having 24 valid solutions and VD-2060 falling behind with 18. The algorithm returned the forces at the moment of maximum assembly compression, indicated as black markers in Figure 6.3, and at the moment of minimum compression (i.e. when the assembly was extended and the aperture opened), depicted as gray markers in the same Figure. The area shadowed in blue corresponds to the region in which the force range falls between the highest minimum and the lowest maximum forces of both nitinol options. In other words, a spring that has both its maximum and minimum forces inside this region can effectively operate with the two types of nitinol wire. For this reason, since model VD-2055 is the only spring that has a force width that is functional with both wires, it is chosen as the best candidate for this design proposal.

Chapter 7

Discussion and Conclusions

Overall, the results demonstrate that, among currently available metallic materials, harnessing the superelastic properties of NiTi is a highly suitable approach for the development of a compact and high-displacement bistable structure. It is shown how both thermal and stress induced austenite-martensite transformations in NiTi can be combined to achieve rapid motion actuators with very low friction, fewer parts, and low energy consumption. The plotted force-displacement curves also show how the desired behavior –operation distance, force, energy– can be accurately tailored with the geometry and the material of the flexing element, which gives the possibility to build actuators with precise movement control –something necessary in many engineering fields. The work demonstrates, through numerical analysis and experimental validation, that the target optical shutter exhibiting bidirectional motion, compact dimensions, passive position locking, and shape memory actuation is feasible for harsh applications such as the exploration of neighbor planets.

The experimental results are in good agreement with the FEA predictions, and the comparison of the calculated force-displacement response confirms that the model reliably captures the nonlinear behavior of the mechanism. The remaining deviations between reality and simulation can reasonably be attributed to the low accuracy experimental setup, the multiple uncontrollable factors of the manufacturing technology used in the prototypes, and the simplifications adopted for the computational model. On one hand, aspects such as clamping friction, imperfect boundary conditions, low-precision equipment, and geometric imperfections coming

from rough manufacturing tolerances are responsible of hindering a closer alignment with the simulation. On the other hand, the FEA model has room for improvement regarding the fine-tuning of the modelled materials and in enhancing the tracking of nonlinearities to match the real physics more closely. It should also be remarked that the software used was a license-free academic version of Abaqus, which naturally comes with program limitations. Such discrepancies, however, are expected when modeling nonlinear compliant mechanisms [50]. When studying the degree of fidelity of the predicted forces and displacements of the first model, it can be backed by literature that the findings are solid. Similar studies published in respected journals show deviation errors in the same range or even higher than in the initial model of this work [32, 33, 44]. It should be noted that for the elaboration of the refined model, the experimental results were needed in order to observe how the physical prototype behaved. The clear asymmetry and the higher force led to a more precise definition of the variables for the model, which in turn resulted in a significantly more accurate prediction.

Although the proposed design has been successfully demonstrated, several aspects remain for further investigation. For the elaboration of similar studies, it is highly recommended to conduct the experimental tests with a standardized tensile testing machine. This is considered particularly importnt as it would provide more reliable boundary conditions by minimizing uneven specimen deformation while also improving the accuracy of the measured force response. Moreover, considering the prototyping with superelastic NiTi was unfortunately outside the available timeframe for this assignment, it is greatly encouraged to include it in future work to enable the refinement and enhance the validation of the superelastic FEA model. The experimental validation was limited to room-temperature conditions, which, even though temperature and external agents were considered theoretically, testing the prototype in an environment with broad thermal amplitude would provide additional confidence for its intended use in harsh environments. Furthermore, long-term cyclic loading was not investigated, as the target application requires fewer than 100 actuation cycles. Nevertheless, the long-term reliability of the mechanism is validated by the fact that the strain is within a safe window of 1-2%, while high-cycle applications such as cardiovascular stents have proofed to survive over 10^8 cycles at mean strains of 5% [65]. Finally, the integration of the bistable mechanism with the SMA actuator was not experimentally validated, as the superelastic and shape memory NiTi materials coud not be delivered within the timeframe of this project. This aspect therefore remains an important step toward the complete experimental verification of the proposed concept.

The objectives established for this master's thesis were successfully achieved through the development of two actuator concepts, concluding with a compact bidirectional shutter that satisfies the dimensional and functional constraints of the Venus Emissivity Mapper. The work demonstrates the feasibility of combining bistable structures with the two unique phase-transformation behaviors of NiTi alloys to develop compact and passively stable actuation systems for aerospace applications, considered to be a very

unusual approach. The close correlation between the numerical predictions and the experimental results provides additional confidence in the followed design methodology, while the limitations identified can be taken into account for future optimization and validation. As such, this work provides a foundation for continuing the development of bistable actuation systems integrating superelastic and shape memory materials.

Chapter 8

Ethical, Sustainable, & Economical analysis

8.1. Sustainability and ethical considerations

During this work, several decisions were influenced by such considertions during the design and development process.

From a manufacturing perspective, the use of 3D-printing for concept validation presents both advantages and limitations. Polymer prototypes were produced using fused deposition modelling (FDM), which enabled rapid design iterations while minimizing building time and material consumption compared to other conventional production methods. As additive manufacturing deposits material only where required, this results in significantly lower material removal than subtractive processes while not being highly energy-demanding. This makes it particularly suitable for low-volume prototyping and research applications. Nevertheless, the fabrication of several design iterations generated plastic waste, particularly from support structures and unsuccessful prototypes. Although these prototypes were necessary to validate the design concept, they represent an environmental cost that should be acknowledged.

The numerical study performed using Abaqus also contributed to reducing material consumption by allowing multiple design alternatives to be evaluated virtually instead of manufacturing physical prototypes. Finite element simulations inevitably require computational resources and therefore consume electrical energy. However, the numerical model was intentionally simplified by employing two-dimensional elements and exploiting geometric symmetry with the goal of minimizing computational effort while maintaining sufficient accuracy. This approach reduced simulation times and allowed a larger number of design iterations to be explored without unnecessary computational cost.

The design was always intended to be made with the smallest footprint in terms of size and weight, not only for functional purposes but also to prevent using nonessential material. It could also be thought that, in case the design was to be used, spacecraft fuel consumption would be reduced given the light weight of the shutter.

The selection of a NiTi alloy can have advantages, such as enabling a more compact and lightweight assembly with reduced part-count, but it also has negative implications, such as the energy-intensive extraction, refinement, processing, and heat treatments necessary for high-quality specialized alloys. This also comes hand in hand with critical ethical concerns, mainly found in the extraction stage, where mineral mining is still extremely unregulated and poses severe threats to basic human rights, namely in resource-rich, low-income countries ruled by capitalist occidental powers.

8.2. Economic breakdown

Decisions were also taken considering their financial cost. Although this was not one of the main constraints or limitations of the project, time, which is in many cases linked with financial expense, definitely was a main factor.

Naturally, time was limited for the development of the work, something that impacted the scope and reach of the project. Additionally, the "time" factor was experienced to be a multi-dependent aspect, as in many occasions it was subject to delays, incomplete tasks or adjustments to the approach plan. A good example is the lack of an actual NiTi working prototype, which was not accomplished due to slow supplier communication and long shipping times.

To have an approximation of the total cost of the project, considering the time invested, the supervision of professionals and professors, the cost of the material for the prototypes, the materials and mounting of the testing rig, the 3D printer, the travel expenses, the program licenses (mainly CATIA V5), the cost of the ordered NiTi (for the first design proposal) and springs (for the second design), and all other factors involved in the work, it could be approximated to:

Factor	Cost
Time	>10,000 €
Supervision	>15,000 €
NiTi (ordered, not received)	~6,500 €
Others (prototypes, program licenses, travel expenses, testing equipment...)	>25,000 €
Project total	**>56,500 €**

Chapter 9

References

[1] Lagoudas, D. C. 2008. Shape Memory Alloys. Vol. 1. Boston, MA: Springer US.

[2] Yuan, H., J. C. Fauroux, F. Chapelle, and X. Balandraud. 2017. "A Review of Rotary Actuators Based on Shape Memory Alloys." Journal of Intelligent Material Systems and Structures 28 (14): 1863–85.

[3] Miková, L., S. Medvecká-Beňová, M. Kelemen, F. Trebuňa, and I. Virgala. 2015. "Application of Shape Memory Alloy (SMA) as Actuator." Metalurgija 54 (1): 169–72.

[4] Yoo, Y. I., J. W. Jeong, J. H. Lim, K. W. Kim, D. S. Hwang, and J. J. Lee. 2013. "Development of a Non-Explosive Release Actuator Using Shape Memory Alloy Wire." Review of Scientific Instruments 84 (1).

[5] Yuan, H., F. Chapelle, J. C. Fauroux, and X. Balandraud. 2018. "Concept for a 3D-Printed Soft Rotary Actuator Driven by a Shape-Memory Alloy." Smart Materials and Structures 27 (5): 055005.

[6] Sheng, J., and J. P. Desai. 2015. "Design, Modeling and Characterization of a Novel Meso-Scale SMA-Actuated Torsion Actuator." Smart Materials and Structures 24 (10): 105005.

[7] Paik, J. K., E. Hawkes, and R. J. Wood. 2010. "A Novel Low-Profile Shape Memory Alloy Torsional Actuator." Smart Materials and Structures 19 (12): 125014.

[8] Hawkes, E., B. An, N. M. Benbernou, H. Tanaka, S. Kim, E. D. Demaine, et al. 2010. "Programmable Matter by Folding." Proceedings of the National Academy of Sciences 107 (28): 12441–45.

[9] Hu, K., K. Rabenorosoa, and M. Ouisse. 2021. "A Review of SMA-Based Actuators for Bidirectional Rotational Motion: Application to Origami Robots." Frontiers in Robotics and AI 8: 678486.

[10] Liu, X., H. Liu, and J. Tan. 2019. "Mesoscale Shape Memory Alloy Actuator for Visual Clarity of Surgical Cameras in Minimally Invasive Robotic Surgery." IEEE Transactions on Medical Robotics and Bionics 1 (3): 135–44.

[11] Schetky, L. M. 1991. "Shape Memory Alloy Applications in Space Systems." Materials & Design 12 (1): 29–32.

[12] Testoni, O., T. Lumpe, J. L. Huang, M. Wagner, S. Bodkhe, Z. Zhakypov, et al. 2021. "A 4D Printed Active Compliant Hinge for Potential Space Applications Using Shape Memory Alloys and Polymers." Smart Materials and Structures 30 (8): 085004.

[13] Paik, J. K., and R. J. Wood. 2012. "A Bidirectional Shape Memory Alloy Folding Actuator." Smart Materials and Structures 21 (6): 065013.

[14] Lu, L., S. Leanza, and R. R. Zhao. 2023. "Origami with Rotational Symmetry: A Review on Their Mechanics and Design." Applied Mechanics Reviews 75 (5): 050801.

[15] Orfin, J., and L. Delaey. 2002. "Hysteresis in Shape-Memory Alloys." International Journal of Non-Linear Mechanics 37 (8): 1275–81.

[16] Jani, J. M. 2016. "Design Optimisation of Shape Memory Alloy Linear Actuator Applications." PhD diss., RMIT University.

[17] Torres-Jara, E., K. Gilpin, J. Karges, R. Wood, and D. Rus. 2010. "Compliant Modular Shape Memory Alloy Actuators." IEEE Robotics & Automation Magazine 17 (4): 78–87.

[18] Steutel, P., G. A. Kragten, and J. L. Herder. 2010. "Design of an Underactuated Finger with a Monolithic Structure and Largely Distributed Compliance." In International Design Engineering Technical Conferences and Computers and Information in Engineering Conference, vol. 44106, 355–63.

[19] Pang, E. L., G. B. Olson, and C. A. Schuh. 2022. "Low-Hysteresis Shape-Memory Ceramics Designed by Multimode Modelling." Nature 610 (7932): 491–95.

[20] Lukco, D., D. J. Spry, R. P. Harvey, G. C. C. Costa, R. S. Okojie, A. Avishai, et al. 2018. "Chemical Analysis of Materials Exposed to Venus Temperature and Surface Atmosphere." Earth and Space Science 5 (7): 270–84.

[21] de Groh, K. K., D. Lukco, S. F. Crowell, S. J. Gregor, and B. A. Banks. 2025. Analyses of the MISSE 9-15 Polymers and Composites Experiment 1-4 (PCE 1-4) Contamination Samples. No. NASA-TM-20240009941. National Aeronautics and Space Administration.

[22] Lai, A., Z. Du, C. L. Gan, and C. A. Schuh. 2013. "Shape Memory and Superelastic Ceramics at Small Scales." Science 341 (6153): 1505–8.

[23] Di Leo, C. V. 2010. "Nitinol-Reinforced Shape-Memory Polymers." PhD diss., Massachusetts Institute of Technology.

[24] Lendlein, A., and S. Kelch. 2002. "Shape-Memory Polymers." Angewandte Chemie International Edition 41 (12): 2034–57.

[25] Contreras, M. M. 2019. "Design, Analysis, and Control of a Nitinol Shape Memory Alloy Rotary Actuator for Spacecraft Deployable Structures." PhD diss., Massachusetts Institute of Technology.

[26] Lan, C. C., J. H. Wang, and C. H. Fan. 2009. "Optimal Design of Rotary Manipulators Using Shape Memory Alloy Wire Actuated Flexures." Sensors and Actuators A: Physical 153 (2): 258–66.

[27] Kramár, T., J. Tauer, and P. Vondrouš. 2019. "Welding of Nitinol by Selected Technologies." Acta Polytechnica 59 (1): 42–50.

[28] Yang, X., W. Chen, H. Liu, B. Yang, Y. Xie, Y. Wang, et al. 2022. "Light-Driven Shape Memory of 3D-Printed PEEK for Programmable Actuations." Advanced Materials Technologies 7 (11): 2200266.

[29] Lazarus, N., G. L. Smith, and M. D. Dickey. 2019. "Self-Folding Helical Origami." Advanced Intelligent Systems 1 (7): 1900059.

[30] Kuribayashi, K., K. Tsuchiya, Z. You, D. Tomus, M. Umemoto, T. Ito, and M. Sasaki. 2006. "Self-Deployable Origami Stent Grafts as a Biomedical Application of Ni-Rich TiNi Shape Memory Alloy Foil." Materials Science and Engineering: A 419 (1–2): 131–37.

[31] Chakrabarti, A., K. Shea, R. Stone, J. Cagan, M. Campbell, N. V. Hernandez, and K. L. Wood. 2011. "Computer-Based Design Synthesis Research: An Overview." Computing and Information Science in Engineering (11): 021003-1

[32] Chen, T., and K. Shea. 2018. "An Autonomous Programmable Actuator and Shape Reconfigurable Structures Using Bistability and Shape Memory Polymers." 3D Printing and Additive Manufacturing 5 (2): 91–101.

[33] Chen, T., J. Mueller, and K. Shea. 2017. "Integrated Design and Simulation of Tunable, Multi-State Structures Fabricated Monolithically with Multi-Material 3D Printing." Scientific Reports 7 (1): 45671.

[34] Testoni, O., S. Bodkhe, A. Bergamini, and P. Ermanni. 2023. "Network of Selectively Compliant Actuators Based on Shape Memory Alloys and Polymers for a Reconfigurable Sandwich Panel." Journal of Intelligent Material Systems and Structures 34 (3): 341–51.

[35] Campanile, L. F., R. Keimer, and E. J. Breitbach. 2004. "The 'Fish-Mouth' Actuator: Design Issues and Test Results." Journal of Intelligent Material Systems and Structures 15 (9–10): 711–19.

[36] Hagelschuer, T., M. Pertenais, I. Walter, P. Dern, S. Del Togno, T. Säuberlich, et al. 2024. "The Venus Emissivity Mapper (VEM): Instrument Design and Development for VERITAS and EnVision." In Infrared Remote Sensing and Instrumentation XXXII, vol. 13144, 116–23. SPIE.

[37] Cermak, A. 2026. "VERITAS - NASA Science." NASA Science. January 30, 2026. https://science.nasa.gov/mission/veritas/.

[38] Envision. n.d. https://www.esa.int/Science_Exploration/Space_Science/Envision.

[39] "VERITAS Mission - VEM Instrument." n.d. DLR. https://www.dlr.de/wr/forschung-transfer/projekte/planetenforschung/vem-veritas.

[40] Cermak, A. 2025. "Science - NASA Science." NASA Science. April 28, 2025. https://science.nasa.gov/mission/veritas/science/.

[41] Bézard, B., C. C. Tsang, R. W. Carlson, G. Piccioni, E. Marcq, and P. Drossart. 2009. "Water Vapor Abundance Near the Surface of Venus from Venus Express/VIRTIS Observations." Journal of Geophysical Research: Planets 114 (E5).

[42] Helbert, J., T. Säuberlich, M. D. Dyar, C. Ryan, I. Walter, J. M. Reess, et al. 2020. "The Venus Emissivity Mapper (VEM): Advanced Development Status and Performance Evaluation." In Infrared Remote Sensing and Instrumentation XXVIII, vol. 11502, 36–59. SPIE.

[43] Cermak, A. 2024. "Overview - NASA Science." NASA Science. November 3, 2024. https://science.nasa.gov/mission/veritas/overview/.

[44] Homer, E. R., M. B. Harris, S. A. Zirbel, J. A. Kolodziejska, H. Kozachkov, B. P. Trease, et al. 2014. "New Methods for Developing and Manufacturing Compliant Mechanisms Utilizing Bulk Metallic Glass." Advanced Engineering Materials 16 (7): 850–56.

[45] Zirbel, S. A., K. A. Tolman, B. P. Trease, and L. L. Howell. 2016. "Bistable Mechanisms for Space Applications." PLoS One 11 (12): e0168218.

[46] Merriam, E. G., J. E. Jones, and L. L. Howell. 2014. "Design of 3D-Printed Titanium Compliant Mechanisms." In The 42nd Aerospace Mechanism Symposium.

[47] Hofmann, D. C., and G. S. Agnes. 2013. Bulk Metallic Glasses and Composites for Optical and Compliant Mechanisms. No. NPO-48768.

[48] Qu, Z., Z. Jiang, R. Liu, and Z. Zhang. 2025. "Naturally High Fatigue Performance of a 3D Printing Titanium Alloy Across All Stress Ratios." Science Advances 11 (34): eady0937.

[49] Wegner, J., M. Frey, R. Busch, and S. Kleszczynski. 2021. "Additive Manufacturing of a Compliant Mechanism Using Zr-Based Bulk Metallic Glass." Additive Manufacturing Letters 1: 100019.

[50] Rossetti, M., S. M. Kargar, and G. Berselli. 2025. "Modeling and Design of Compliant Bistable Mechanisms: A Brief Review with a Case Study on Variable Constant Force Mechanism." In 2025 IEEE/ASME International Conference on Advanced Intelligent Mechatronics (AIM), 1–6. IEEE.

[51] Gustafson, K. J. 2019. "Study of the Compliance and System Integration of Bistable for Use as Actuation Mechanisms in Bioinspired Adaptive Systems." PhD diss., University of Illinois at Urbana-Champaign.

[52] Wooten, J., and D. P. Dennies. 2008. "Electron Beam Manufacturing for Production Hardware." SAE International.

[53] Masters, N. D., and L. L. Howell. 2003. "A Self-Retracting Fully Compliant Bistable Micromechanism." Journal of Microelectromechanical Systems 12 (3): 273–80.

[54] Howell, L. L. 2013. "Compliant Mechanisms." In 21st Century Kinematics: The 2012 NSF Workshop, 189–216. London: Springer London.

[55] Zhu, J. N., W. Zhu, E. Borisov, X. Yao, T. Riemslag, C. Goulas, et al. 2023. "Effect of Heat Treatment on Microstructure and Functional Properties of Additively Manufactured NiTi Shape Memory Alloys." Journal of Alloys and Compounds 967: 171746.

[56] Kim, S. W., J. S. Koh, J. G. Lee, J. Ryu, M. Cho, and K. J. Cho. 2014. "Flytrap-Inspired Robot Using Structurally Integrated Actuation Based on Bistability and a Developable Surface." Bioinspiration & Biomimetics 9 (3): 036004.

[57] Patel, H., J. Arora, S. Joshi, and S. Mukherjee. 2021. "Development of Shape Memory Alloy (SMA) Based Hold-Down and Release Mechanism for Space Applications." In Advances in Industrial Machines and Mechanisms: Select Proceedings of IPROMM 2020.

[58] Smith, S., D. Dowen, E. Fossness, and A. Peffer. 1999. "Development of Shape Memory Alloy (SMA) Actuated Release Mechanism for Spacecraft Applications." 13th AIAA/USU Conference on Small Satellites.

[59] Dassault Systèmes. 2024. "Unstable Collapse and Postbuckling Analysis." Abaqus HTML Documentation. https://docs.software.vt.edu/abaqusv2024/English/?show=SIMACAEANLRefMap/simaanl-c-postbuckling.htm.

[60] Plummer, G., M. I. Mendelev, O. Benafan, and J. W. Lawson. 2023. "Microstructural Mechanisms of Hysteresis and Transformation Width in NiTi Alloy from Molecular Dynamics Simulations." Journal of Physics: Condensed Matter 35 (49): 495404.

[61] Yan, Z., J. N. Zhu, E. Borisov, T. Riemslag, S. P. Scott, M. Hermans, et al. 2023. "Superelastic Response and Damping Behavior of Additively Manufactured Nitinol Architectured Materials." Additive Manufacturing 68: 103505.

[62] Ma, J., I. Karaman, and R. D. Noebe. 2010. "High Temperature Shape Memory Alloys." International Materials Reviews 55 (5): 257–315.

[63] Liu, T., G. Hao, J. Zhu, P. Kuresangsai, S. Abdelaziz, and E. Wehrle. 2024. "Modeling Compliant Mechanisms Based on the High-Order Smooth Curvature Model." International Journal of Mechanical Sciences 275: 109315.

[64] Ansys Inc. 2020. "Engineering Strain and True Strain." Mechanical Strain in Deformation Analysis.

[65] Launey, M. E., S. M. Pelton, H. Gill, P. Saffari, J. Keck, J. Ulmer, et al. 2025. "High-Durability Nitinol for Medical Devices: A 100 Million-Cycle Bending Fatigue Characterization Study." Shape Memory and Superelasticity, 1–18.

[66] Shahsavari, H., X. Chen, G. Kaleng Tshikwand, F. Wendler, and M. Kohl. 2024. "Finite-Element Analysis of an Antagonistic Bistable Shape Memory Alloy Beam Actuator." Advanced Engineering Materials 26 (22): 2400969.

[67] Bernini, M., R. Hellmuth, C. Dunlop, W. Ronan, and T. J. Vaughan. 2023. "Recommendations for Finite Element Modelling of Nickel-Titanium Stents—Verification and Validation Activities." PLoS One 18 (8): e0283492.

[68] Berti, F., S. Bridio, G. Luraghi, S. Pant, D. Allegretti, G. Pennati, and L. Petrini. 2022. "Reliable Numerical Models for Nickel-Titanium Stents: How to Deduce the Specific Material Properties from Testing Real Devices." Annals of Biomedical Engineering 50 (4): 467–81.

[69] Hartwell, A. A. J. 2018. "Shape Memory Alloys for Small Scale Actuation." PhD diss., Massachusetts Institute of Technology.

[70] MatWeb LLC. n.d. "Online Materials Information Resource Web Page." http://www.matweb.com.

[71] Auricchio, F., and R. L. Taylor. 1997. "Shape-Memory Alloys: Modelling and Numerical Simulations of the Finite-Strain Superelastic Behavior." Computer Methods in Applied Mechanics and Engineering 143 (1–2): 175–94.

[72] Yan, L., S. Lu, and P. Liu. 2023. "Development of a Fully Compliant Bistable Mechanism Based on Circular Beams with Enhanced Pitch Stiffness." Applied Sciences 13 (3): 1642.

[73] Dunning, A. G., N. Tolou, P. P. Pluimers, L. F. Kluit, and J. L. Herder. 2012. "Bistable Compliant Mechanisms: Corrected Finite Element Modeling for Stiffness Tuning and Preloading Incorporation." Journal of Mechanical Design 134 (8): 084502.

Appendices

Appendix A - Proposal evaluation matrix

Appendix B - Raw FEA data

Appendix C - Python spring selection code

Appendix A – Proposal evaluation matrix

	Reliability	Justification
	25%	
Proposal A	2	The rolling/folding of two sheets could differ between cycles due to factors like; springback, sheets interfering, unwanted swings during transition.
Proposal B	1	More variables, more risk of undesired behavior. SMP could heat up due to environment and force SMA to move, lower apparent precision,...
Proposal C	3	The bistable mechanism is like a switch, meaning it can be consistently opened /closed the same way over a high number of cycles.

	Scalability/dimensions/mass	Justification
	10%	
Proposal A	2	Due to the design's simplicity, scaling it up or down is feasible. However, power consumption would be significant if scaled up due to the large surface areas. Mass would also increase notably as it is an all-metal design.
Proposal B	1	It could be scaled up/down and its weight is expected to be very similar to the others. However, the SMP+SMA integration could be challenging at small scales.
Proposal C	3	This type of mechanism has been successfully manufactured at the nanoscale [53] (although without SMAs). Due to its relatively low power (wire/strip instead of foil), it could also be scaled up. The mass could be very low, as the different parts of the component could be made out of a polymeric or a composite material.

	Energy Consumption	Justification
	10%	
Proposal A	1	Significantly larger surface area required to heat up compared to the other options.
Proposal B	2	Wires need to be heated enough to conduct the heat into the SMP and make the latter reach its Tg. If the SMP's section is small, power could be relatively low.
Proposal C	3	Wires and/or strips need to be heated up. The strip could require significant power, but at such small scale probably not as much as the other two.

	Mechanical	Justification
	10%	
Proposal A	2	Being all NiTi, the mechanical performance is high. However, as folding requires a thin sheet (micron-level), out-of-plane deformation could occur under load (although improbable if designed with rails/guides to prevent it).
Proposal B	1	Seems the least favorable option in terms of robustness of the mechanism/design, although it could still perform well.
Proposal C	3	The stability/robustness is expected to be very high. It can be expected that no heavy vibration or typical sine load could alter the mechanism's position.

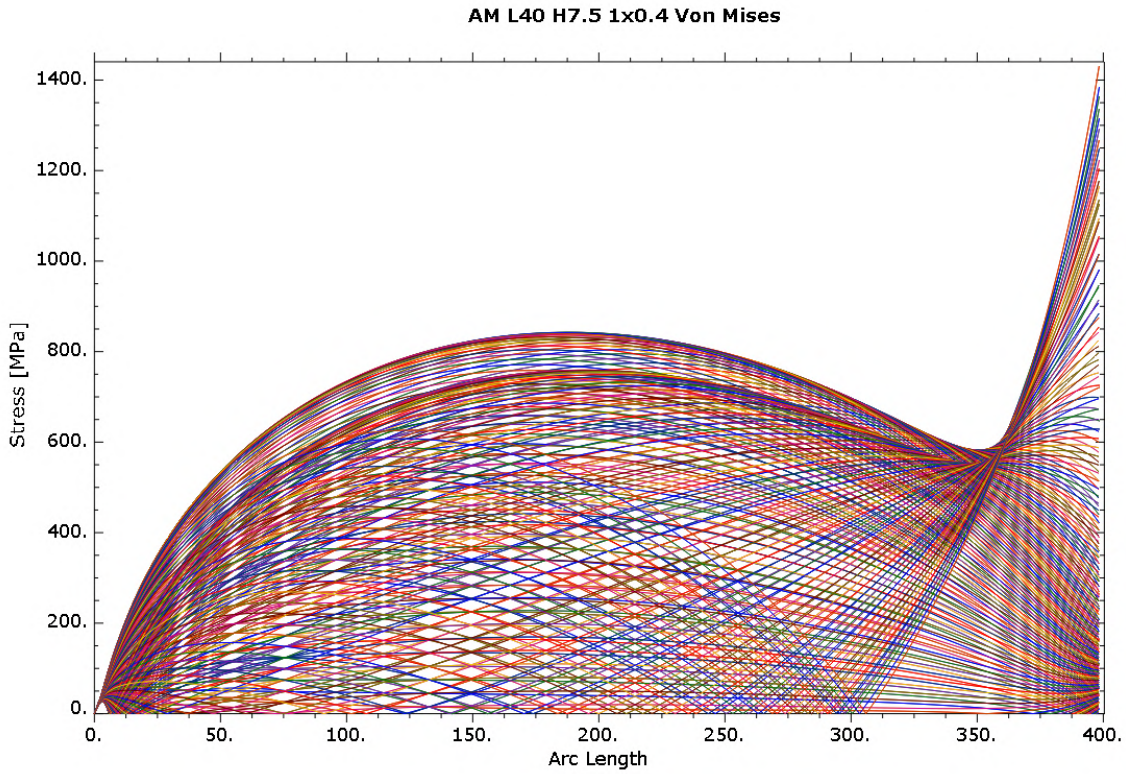
	Thermal	Justification
	10%	
Proposal A	2	NiTi SMAs can withstand significantly higher temperatures than the mission's. The only drawback could be the Af (≈90°C). However, as the shutter doesn't have to be actuated at *Tmax* (as during Sun calibration closed shutter is preferred), the front sheet can shield while being exposed at above-Af temperatures in an austenitic state, keeping the shutter closed, and then opening it using the back sheet once the front one has cooled below Af.
Proposal B	1	Having an SMP exposed at such temperatures can be problematic, as it probably makes the SMP to easily reach Tg. Furthermore, both the high temperatures and extreme UV exposure could most certainly degrade the polymer chains. It should be tested.
Proposal C	3	Similarly to Proposal A, if metals are used for the exposed part, it could comfortably withstand high temperatures. In this design, since the SMA is not exposed, there is not as big of a risk with the transformation temperature as with the SMA sheets/foils.

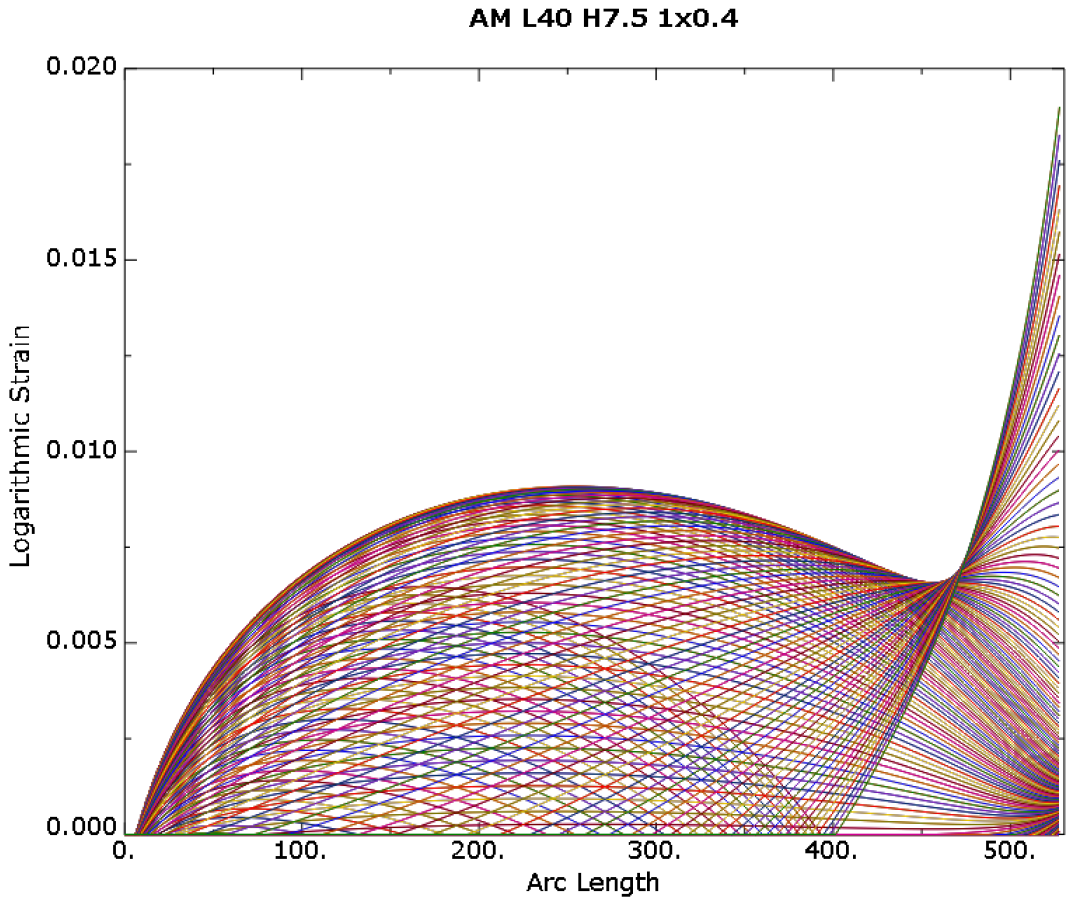
	Cost	Justification
	15%	
Proposal A	3	The low design complexity makes this option the most favorable. Components are readily available, although price is the highest due to larger quantities of SMA.
Proposal B	1	Price is between Proposals A and C (only wires, but need to be thick in order to bend the SMP). Design complexity is possibly the highest considering the limited space and the polymer-metal integration.
Proposal C	2	The design takes more time to be developed (geometry, snap testing, component placement) but there's availability and price is expected to be the lowest.

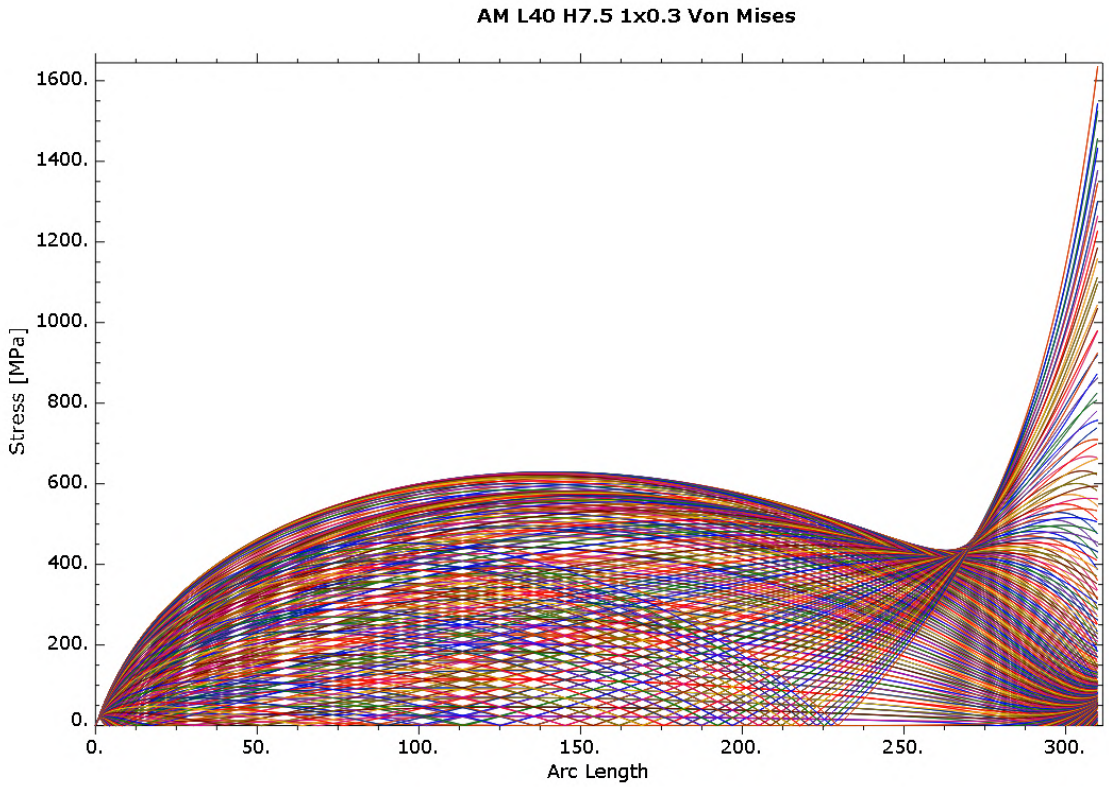
	Manufacturability	Justification
	20%	
Proposal A	3	Straightforward to obtain and assemble. Complexity could arise from shape setting, adding slits (laser engraving), or embedding a resistance path.
Proposal B	1	Most complex as SMP and SMA need to somehow be embedded. Availability of SMP with specific shape could be very challenging to find (possibly with 3D printing).
Proposal C	2	Higher complexity than A due to having the assembly of the bistable mechanism with the SMA components, but lower than B.

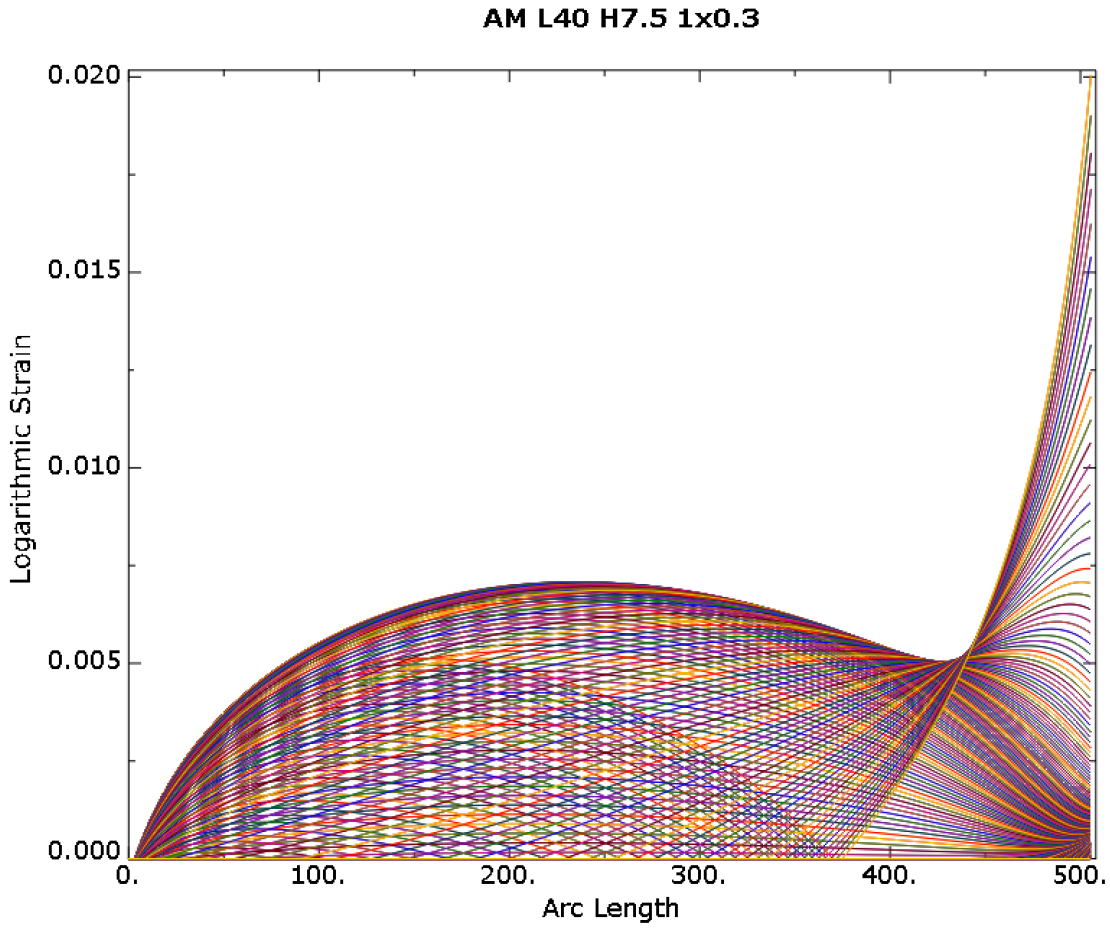
Appendix B – Raw FEA data

Amorphous metal (AM), ZR-01 – Short beam

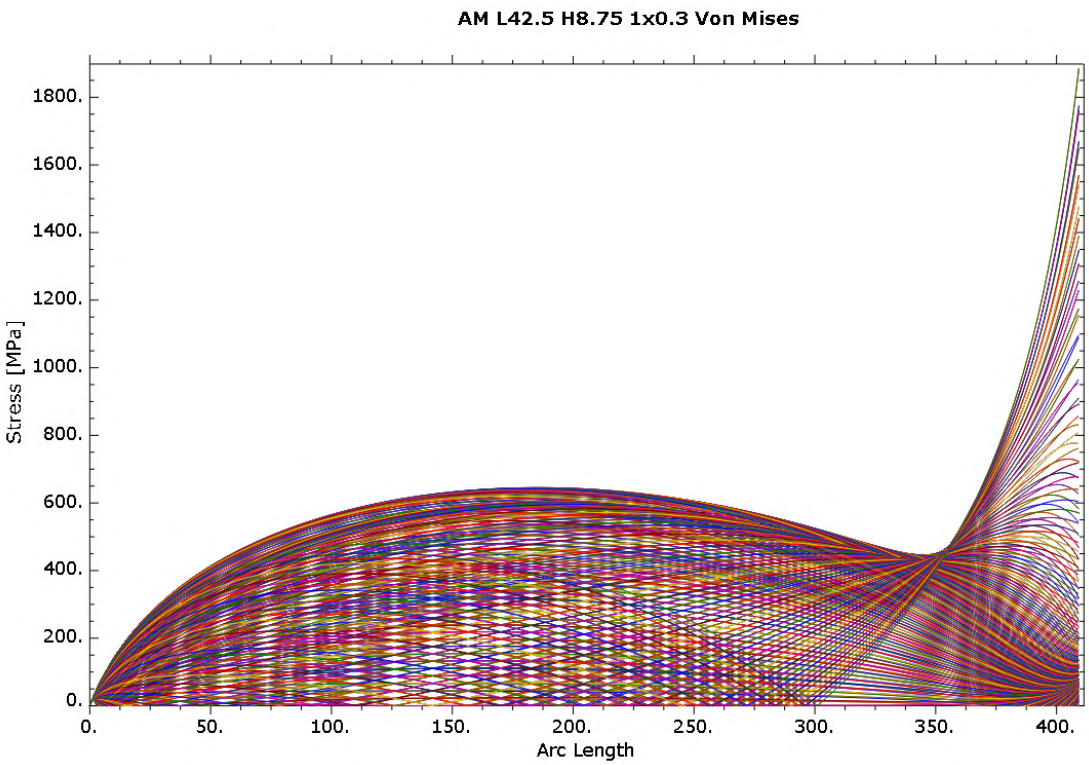


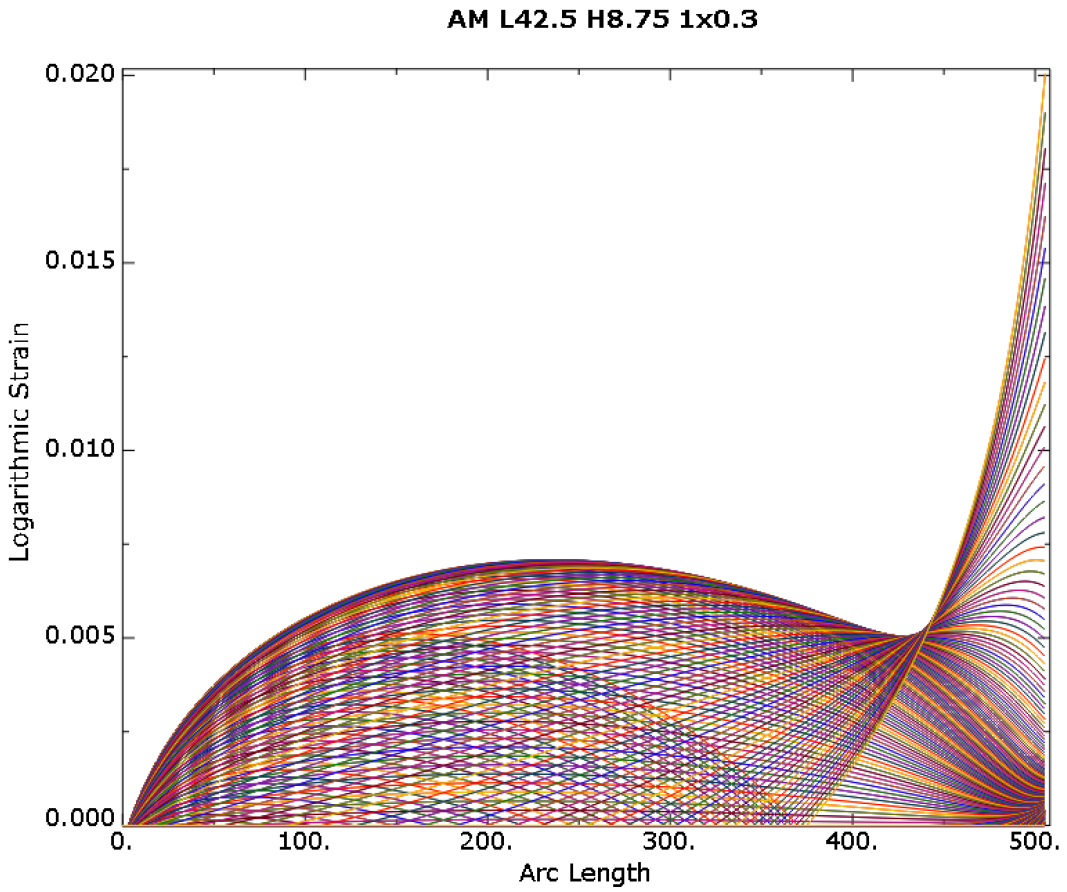


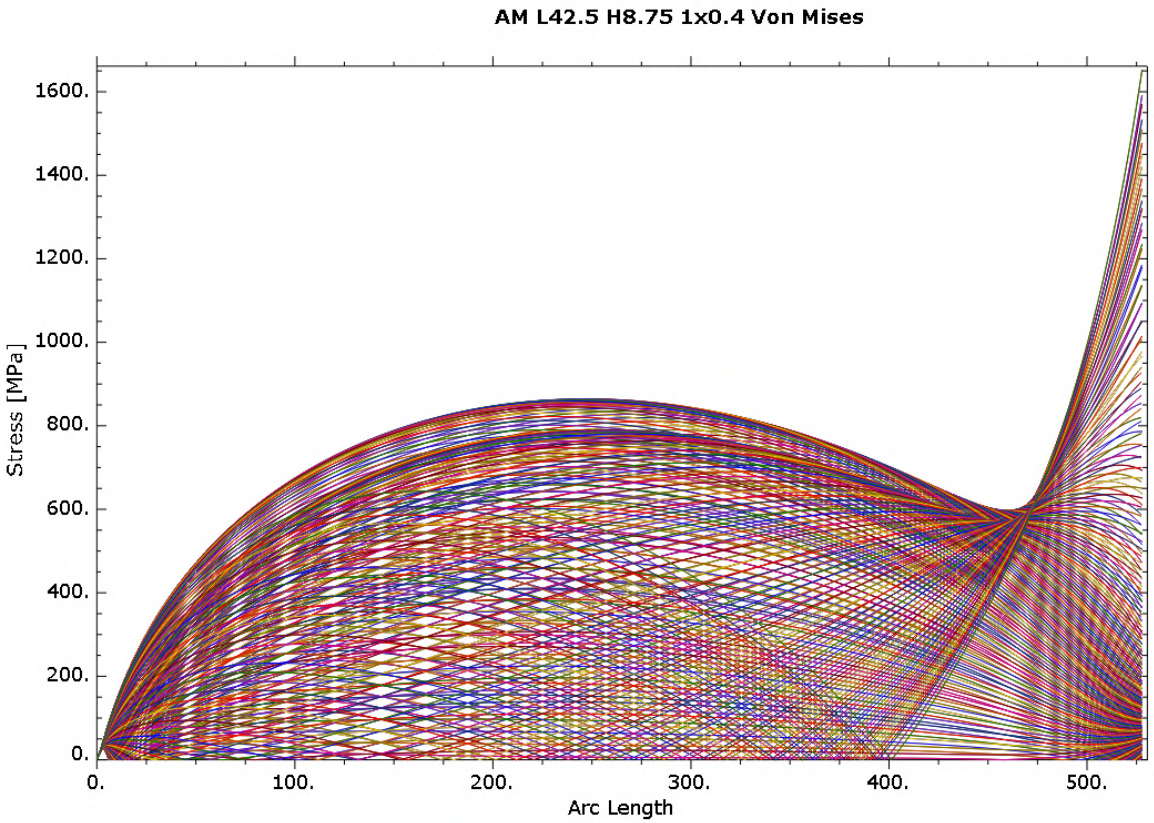

AM L40 H7.5 1x0.3 Von Mises
Stress [MPa]
1600.
1400.
1200.
1000.
800.
600.
400.
200.
0.
0.
50.
100.
150.
200.
250.
300.
Arc Length

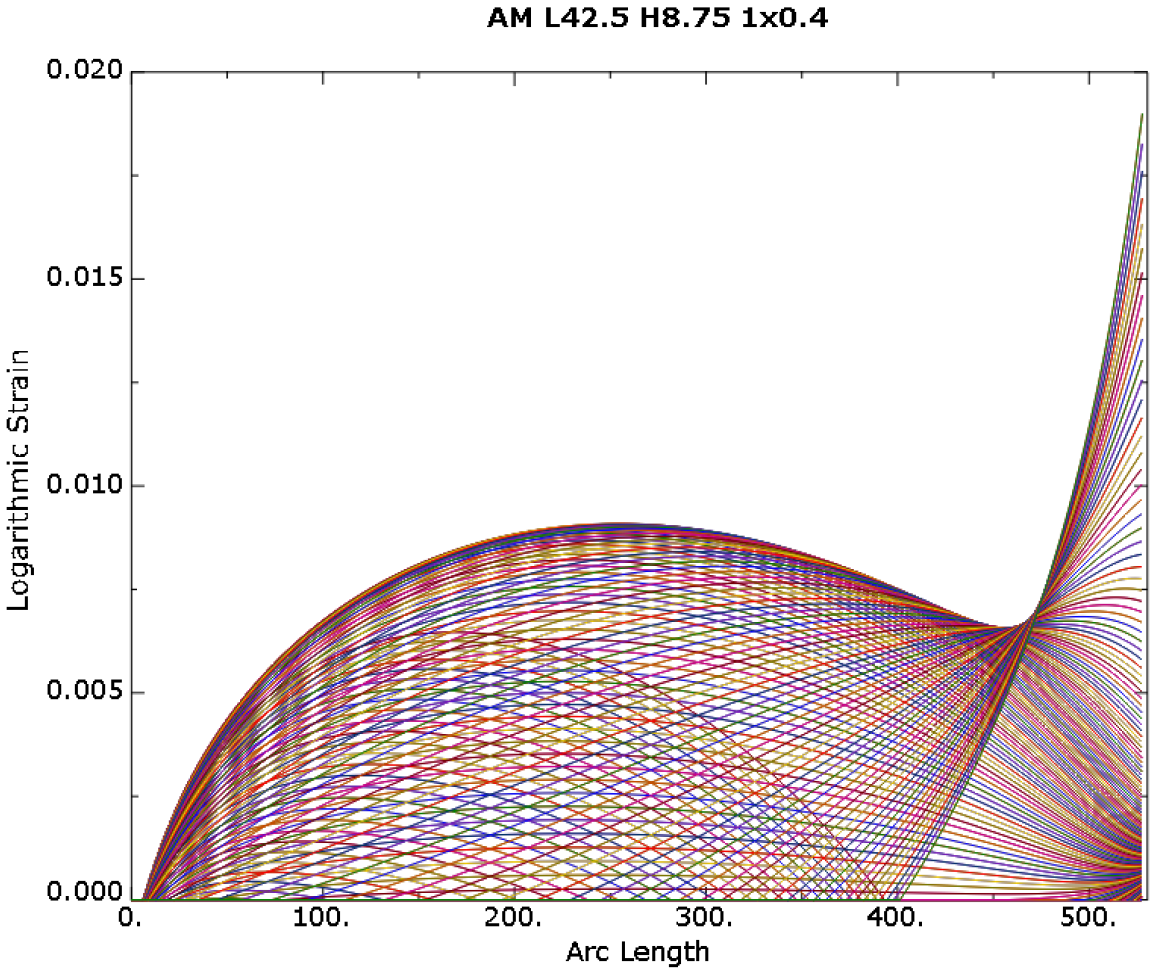

AM L40 H7.5 1x0.3
Logarithmic Strain
0.020
0.015
0.010
0.005
0.000
0.
100.
200.
300.
400.
500.
Arc Length

Amorphous metal (AM), ZR-01 – Average beam

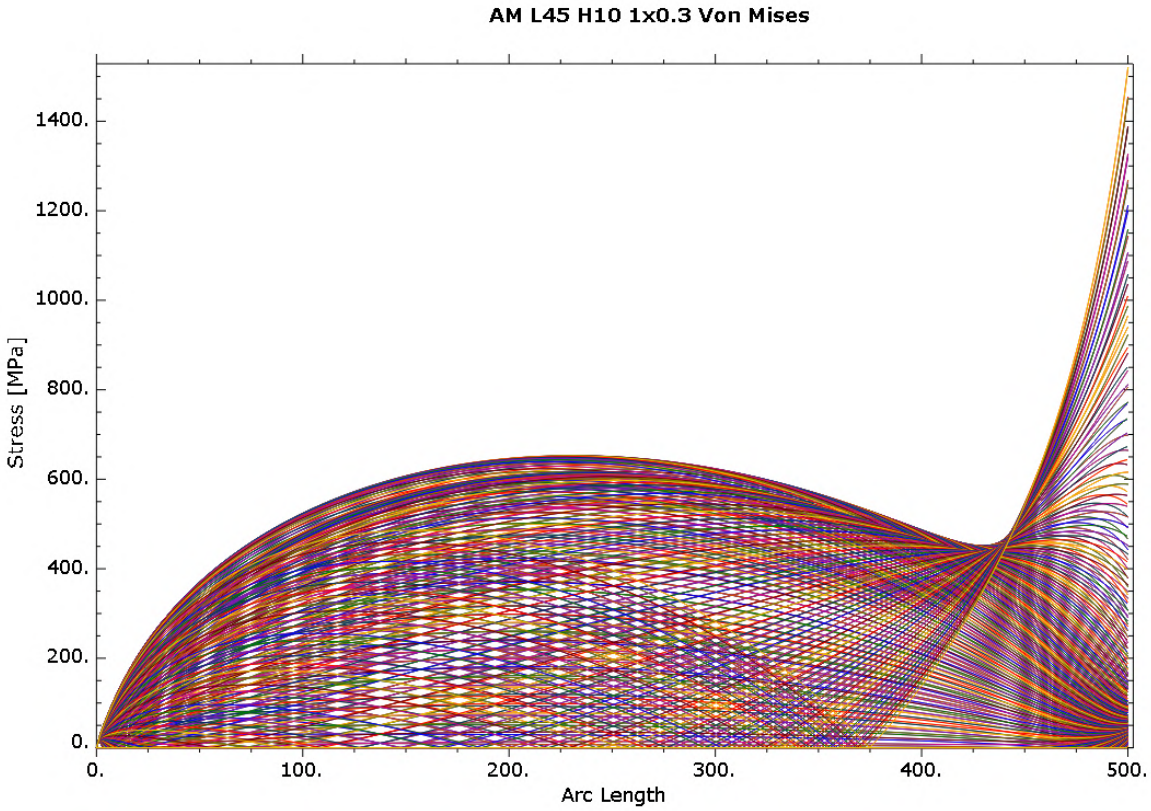


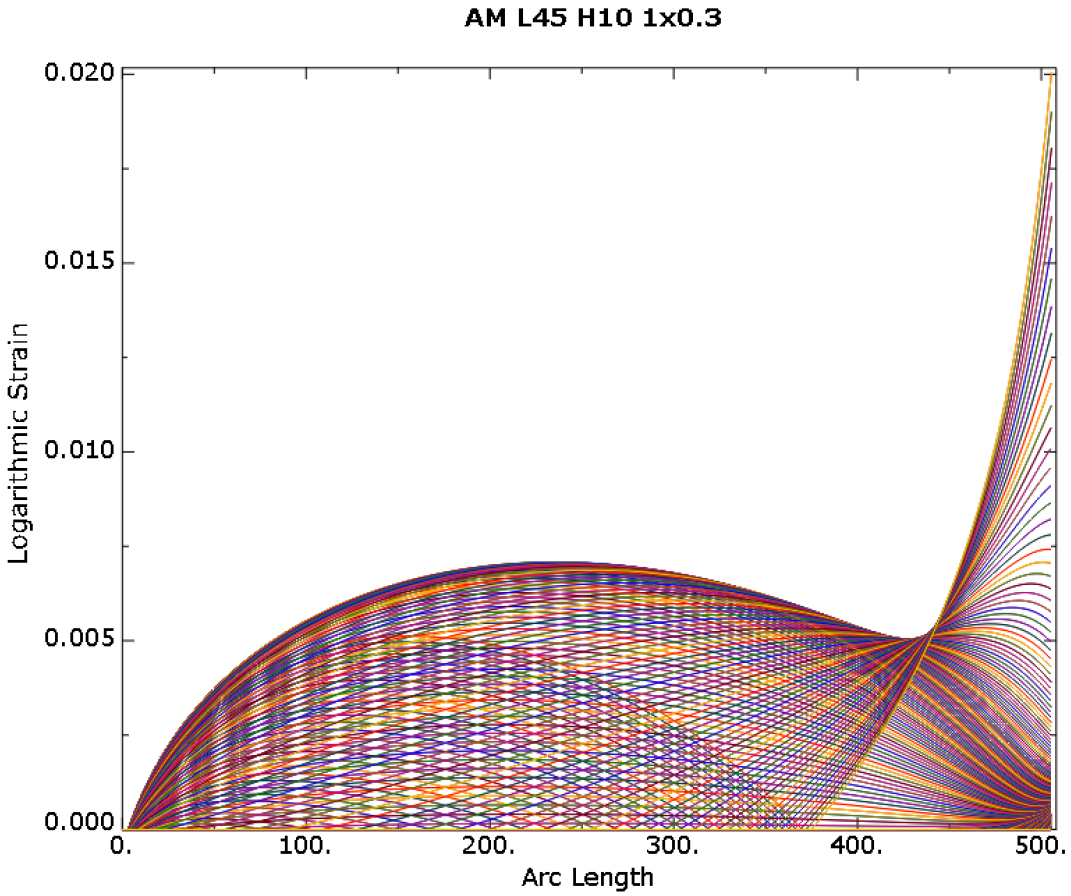


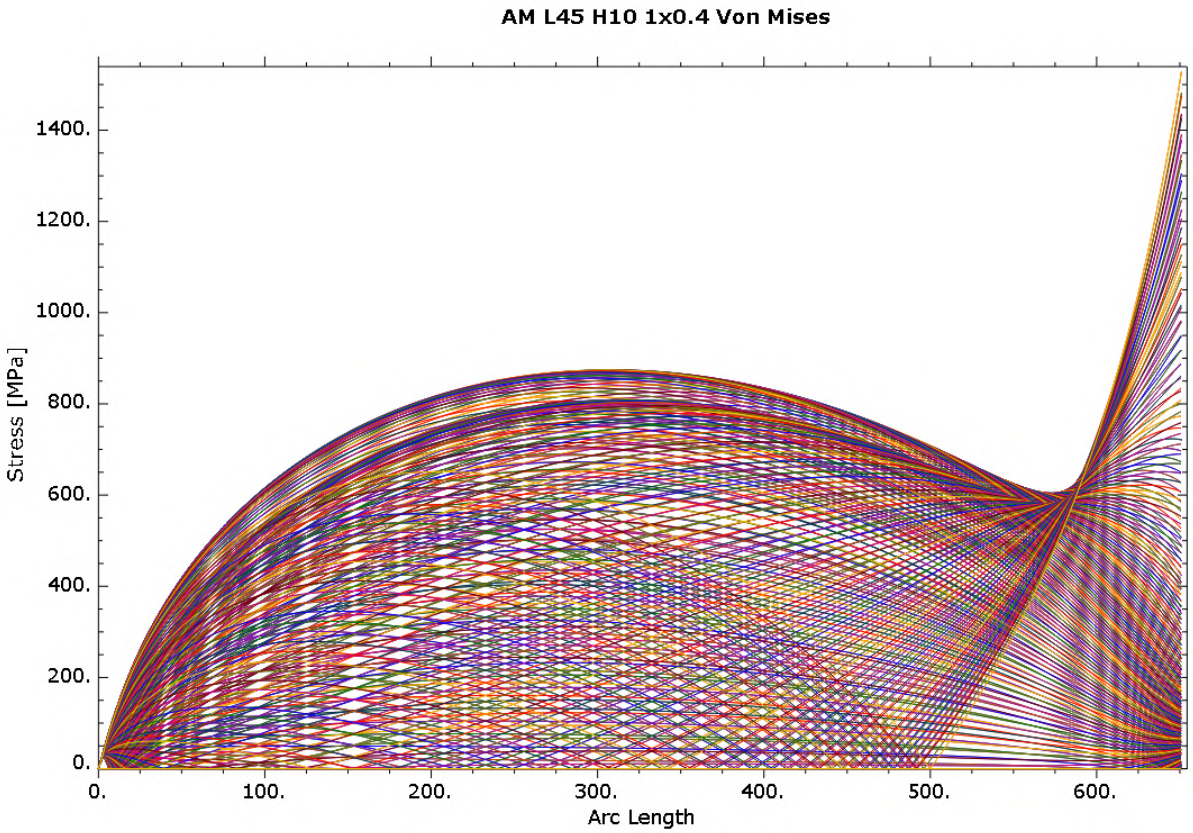

AM L42.5 H8.75 1x0.4 Von Mises
Stress [MPa]
1600.
1400.
1200.
1000.
800.
600.
400.
200.
0.
0.
100.
200.
300.
400.
500.
Arc Length

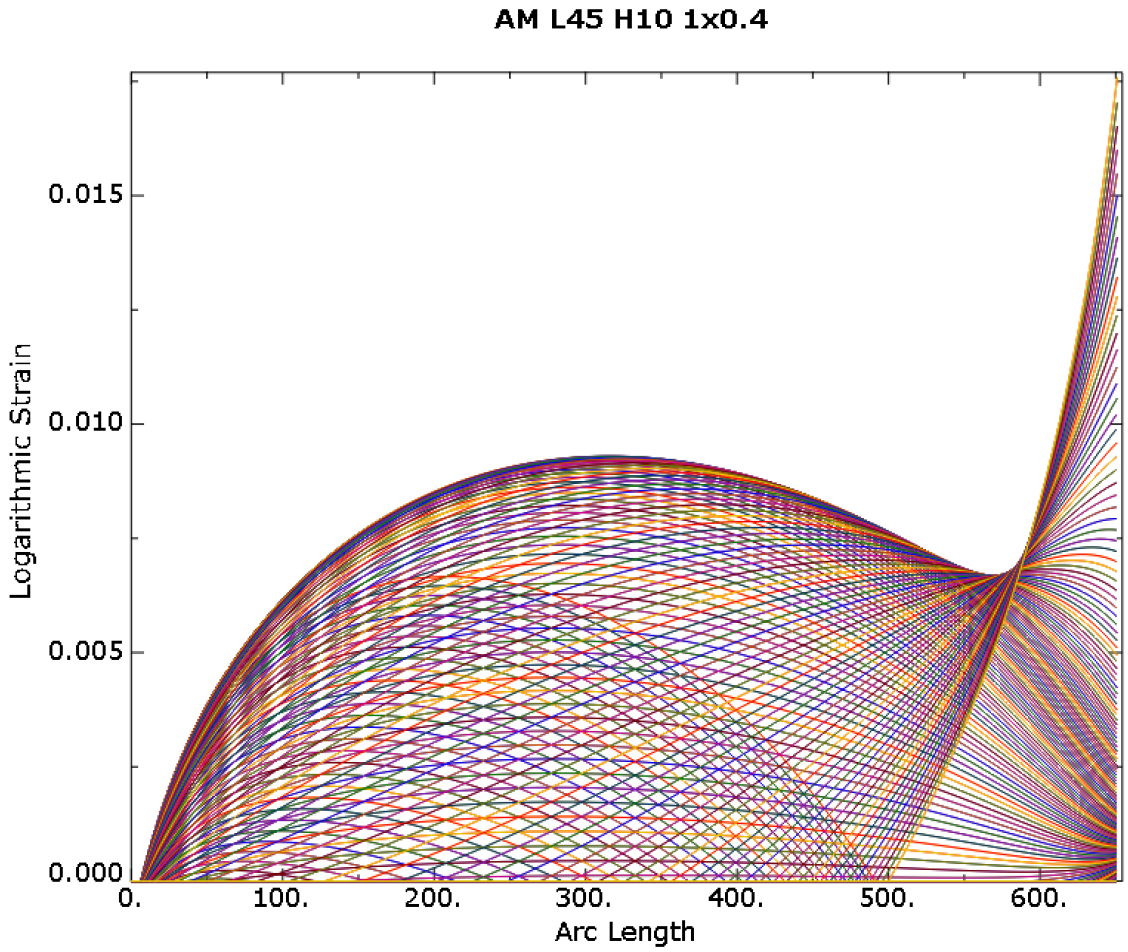

AM L42.5 H8.75 1x0.4
Logarithmic Strain
0.020
0.015
0.010
0.005
0.000
0.
100.
200.
300.
400.
500.
Arc Length

Amorphous metal (AM), ZR-01 – Long beam

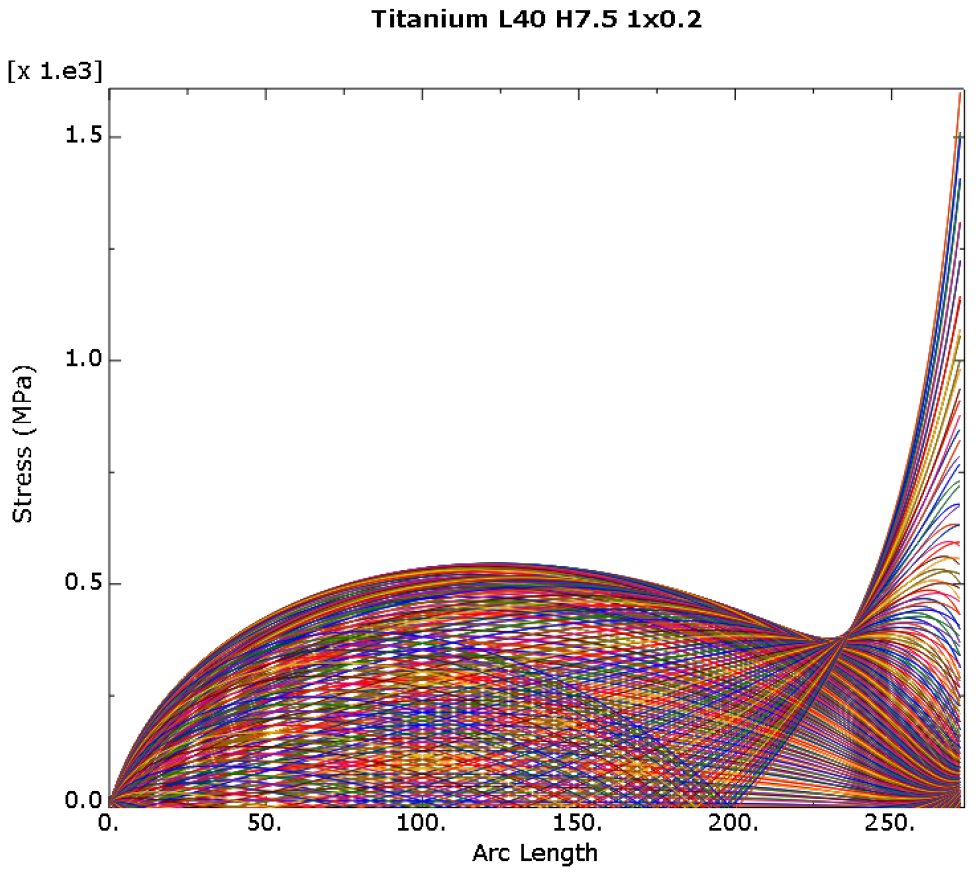


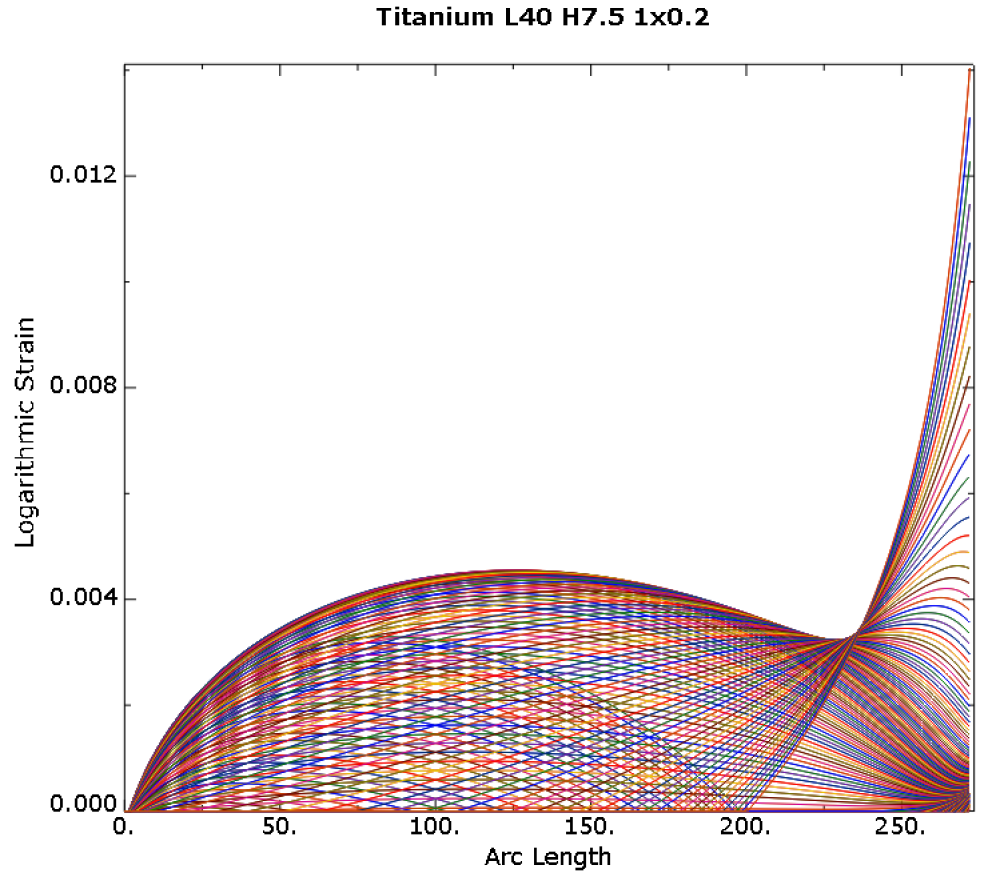


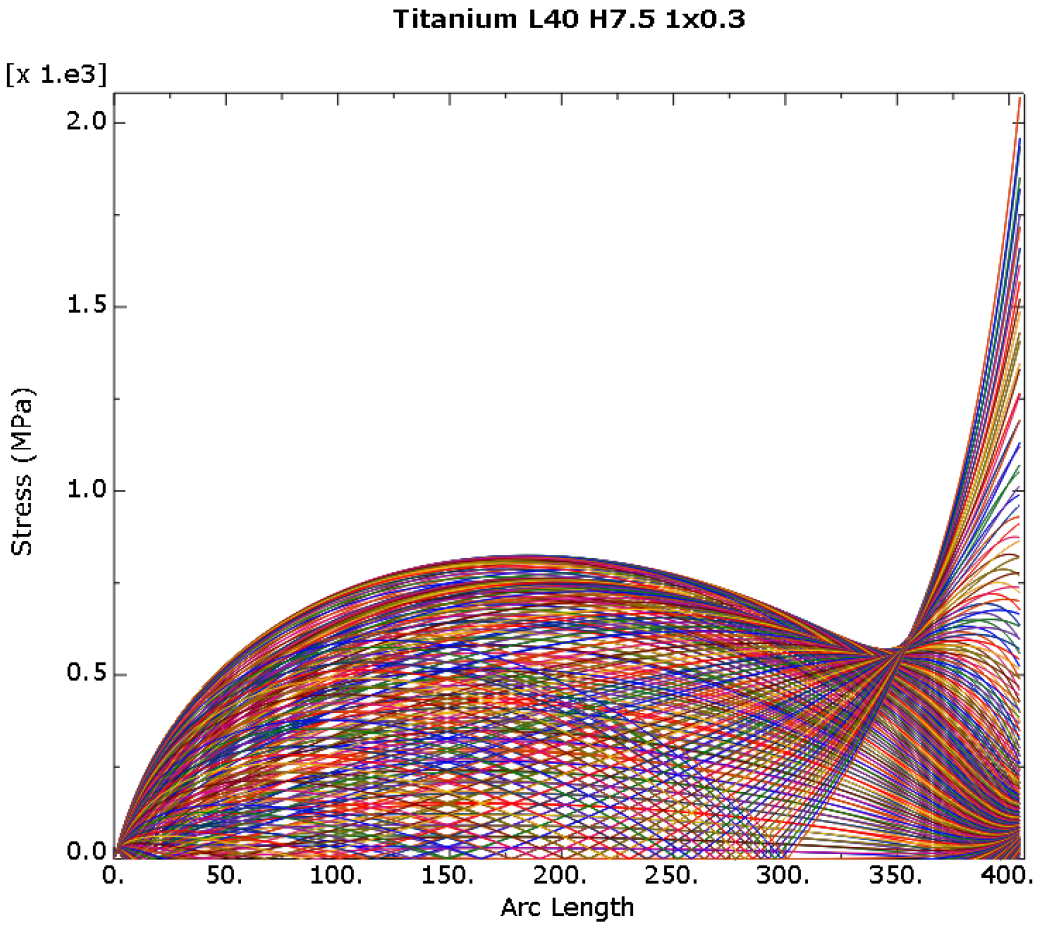

AM L45 H10 1x0.4 Von Mises
Stress [MPa]
1400.
1200.
1000.
800.
600.
400.
200.
0.
0.
100.
200.
300.
400.
500.
600.
Arc Length

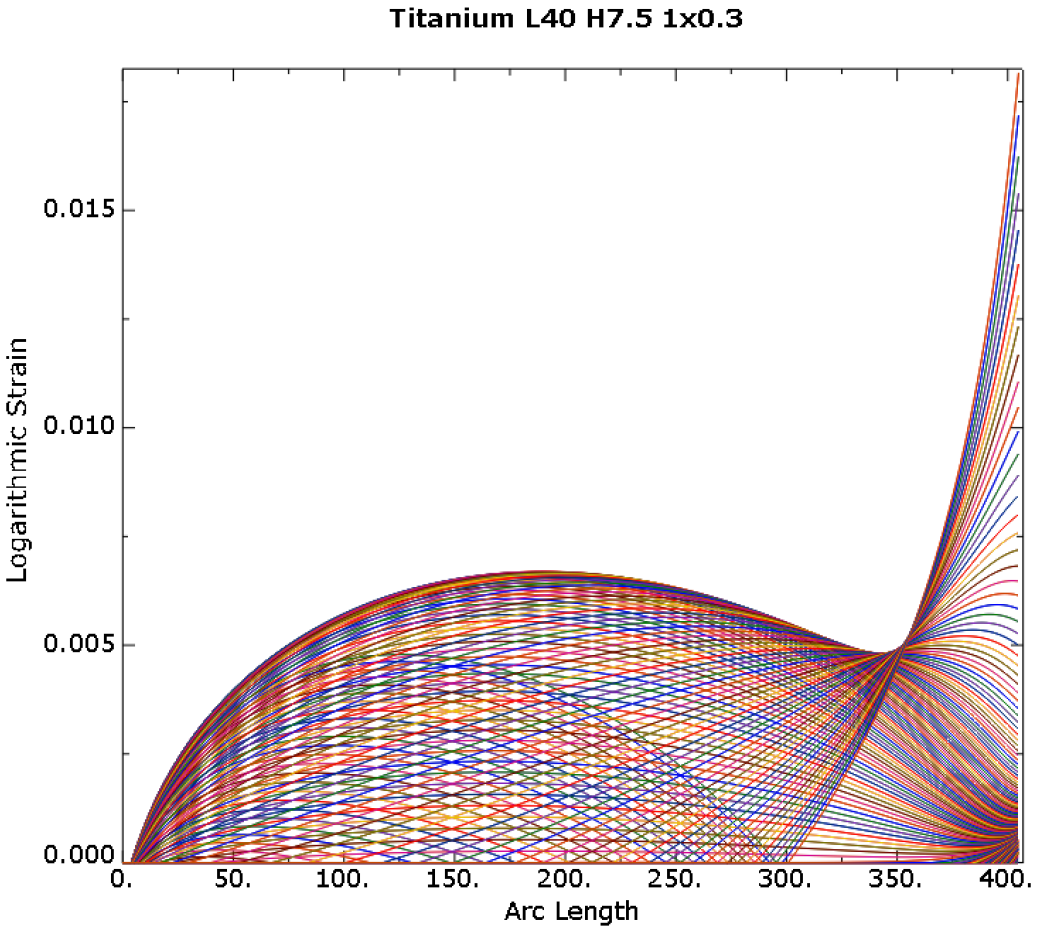

AM L45 H10 1x0.4
Logarithmic Strain
0.015
0.010
0.005
0.000
0.
100.
200.
300.
400.
500.
600.
Arc Length

Titanium, Ti6Al4V – Short beam

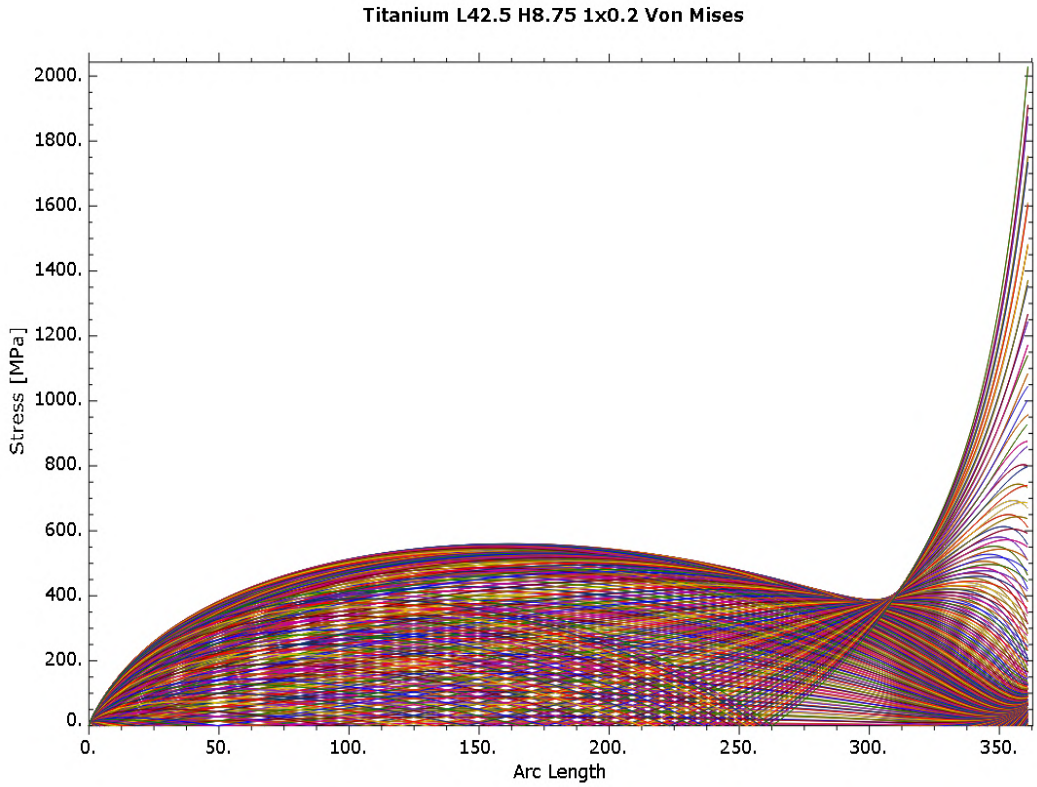


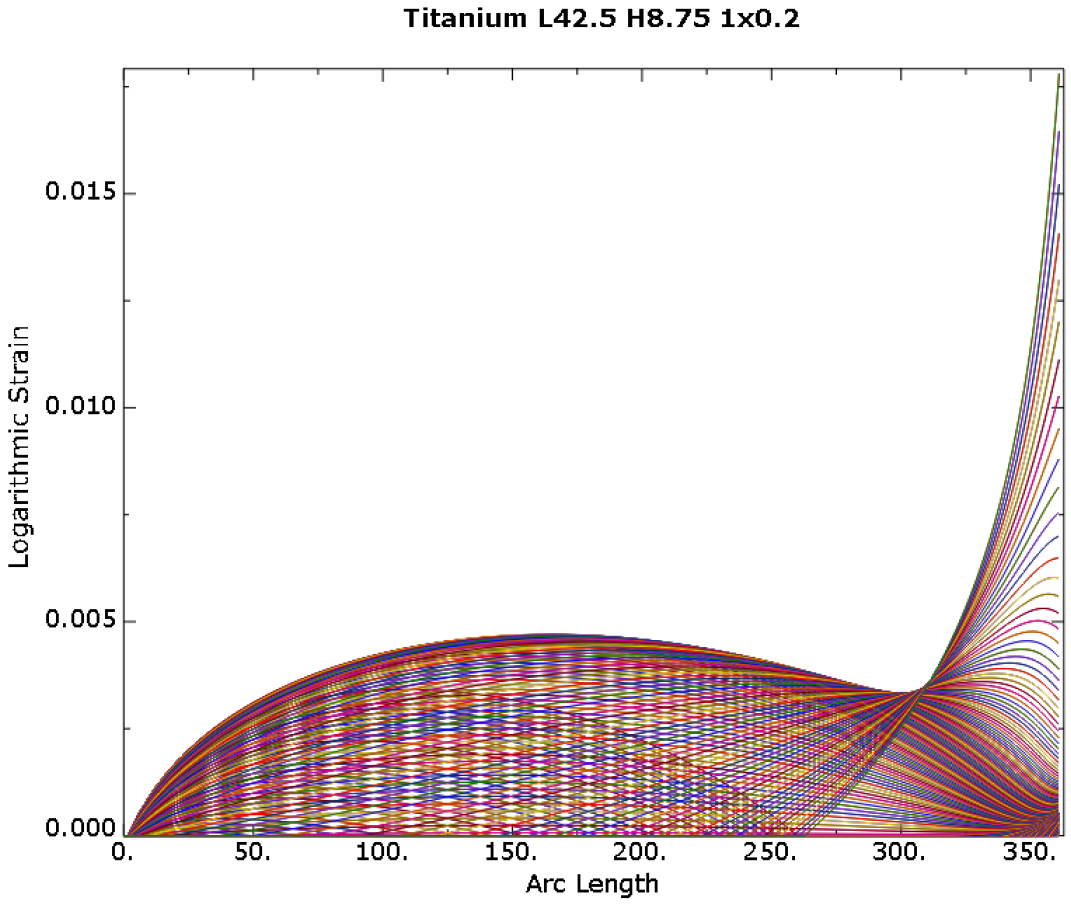


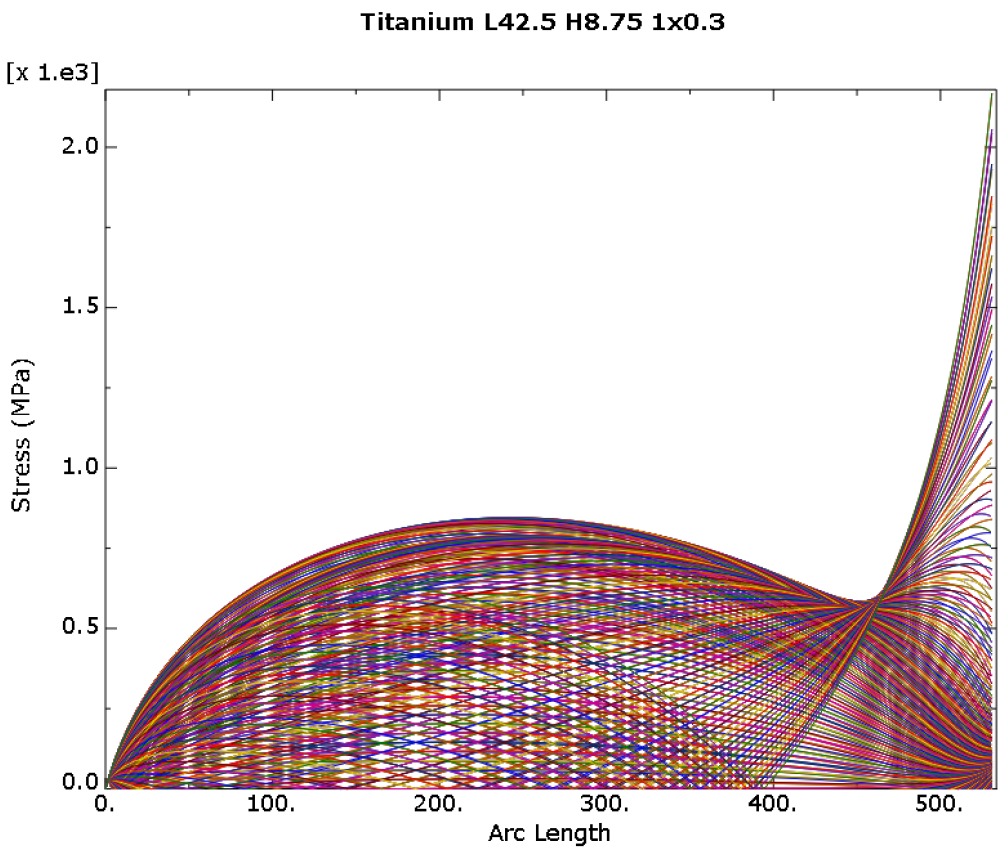

Titanium L40 H7.5 1x0.3
[x 1.e3]
2.0
1.5
1.0
0.5
0.0
Stress (MPa)
0.
50.
100.
150.
200.
250.
300.
350.
400.
Arc Length

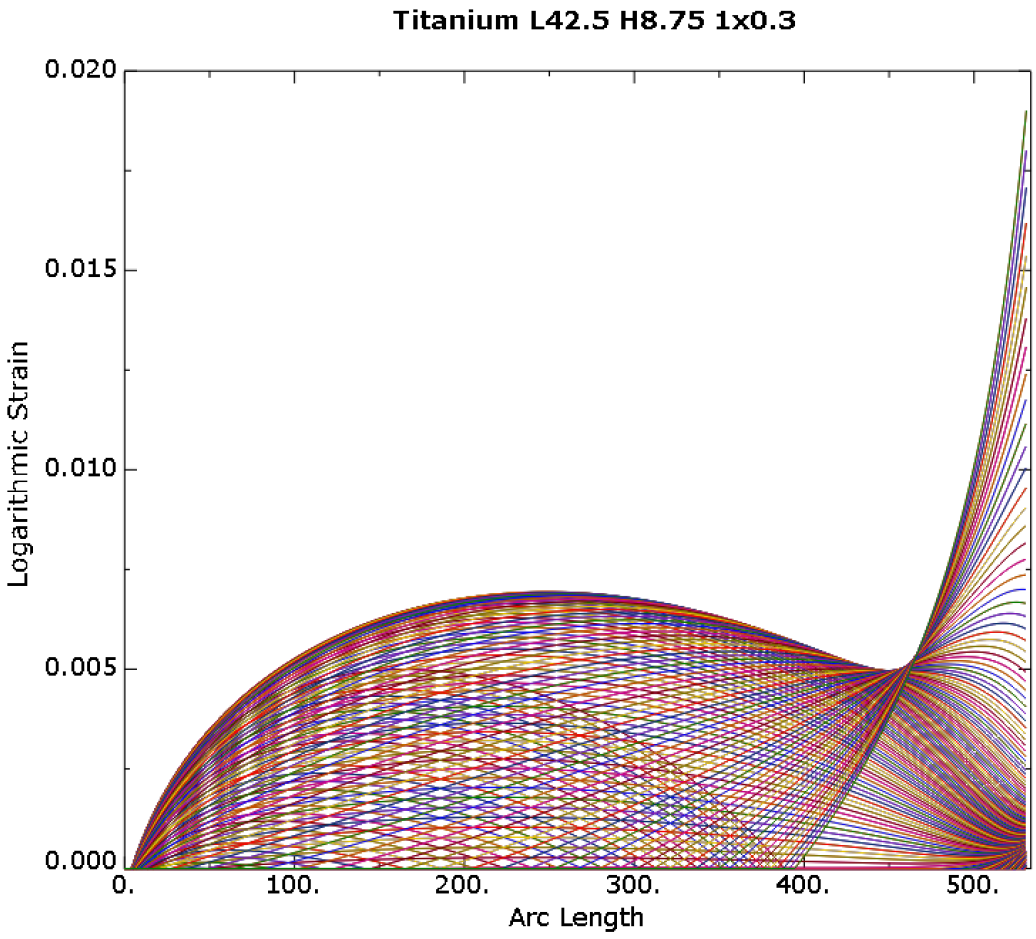

Titanium L40 H7.5 1x0.3
0.015
0.010
0.005
0.000
Logarithmic Strain
0.
50.
100.
150.
200.
250.
300.
350.
400.
Arc Length

Titanium, Ti6Al4V – Average beam

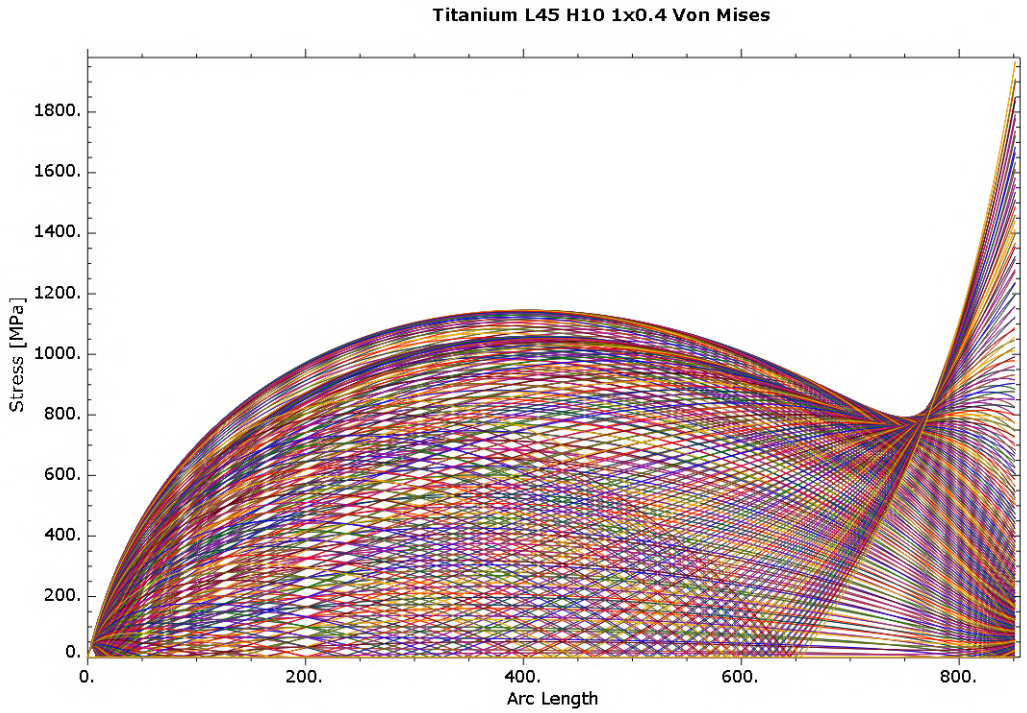


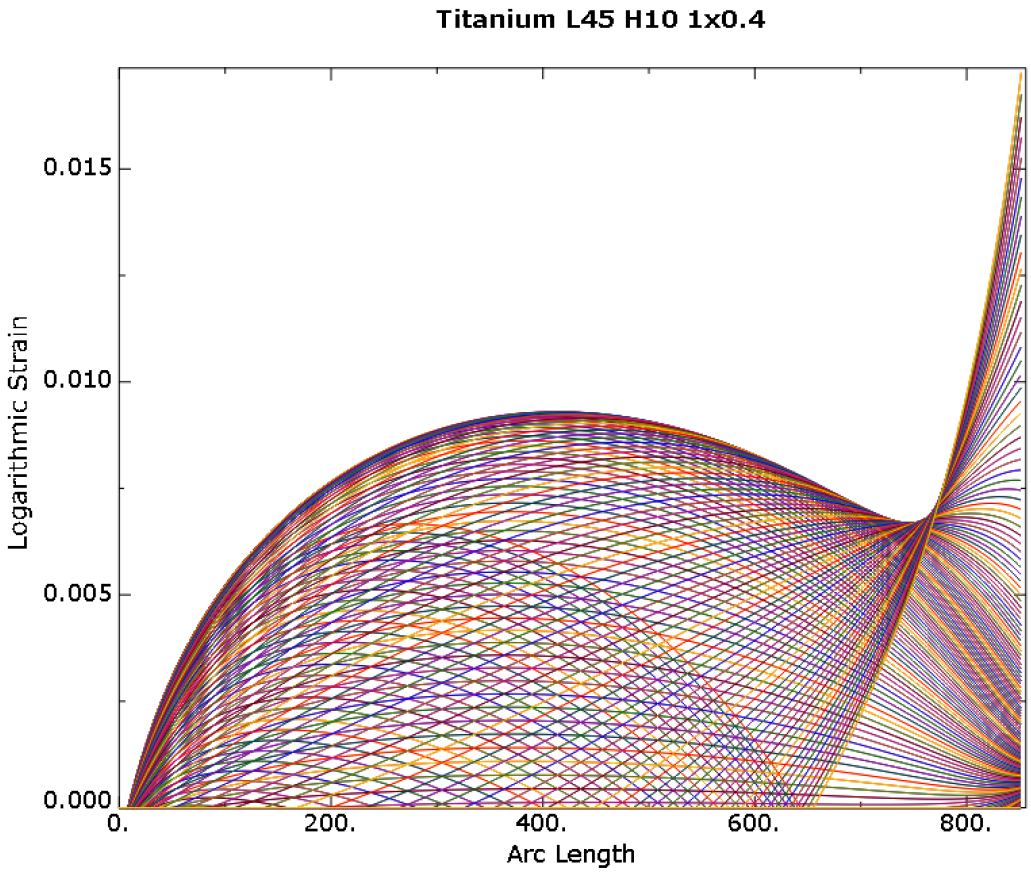


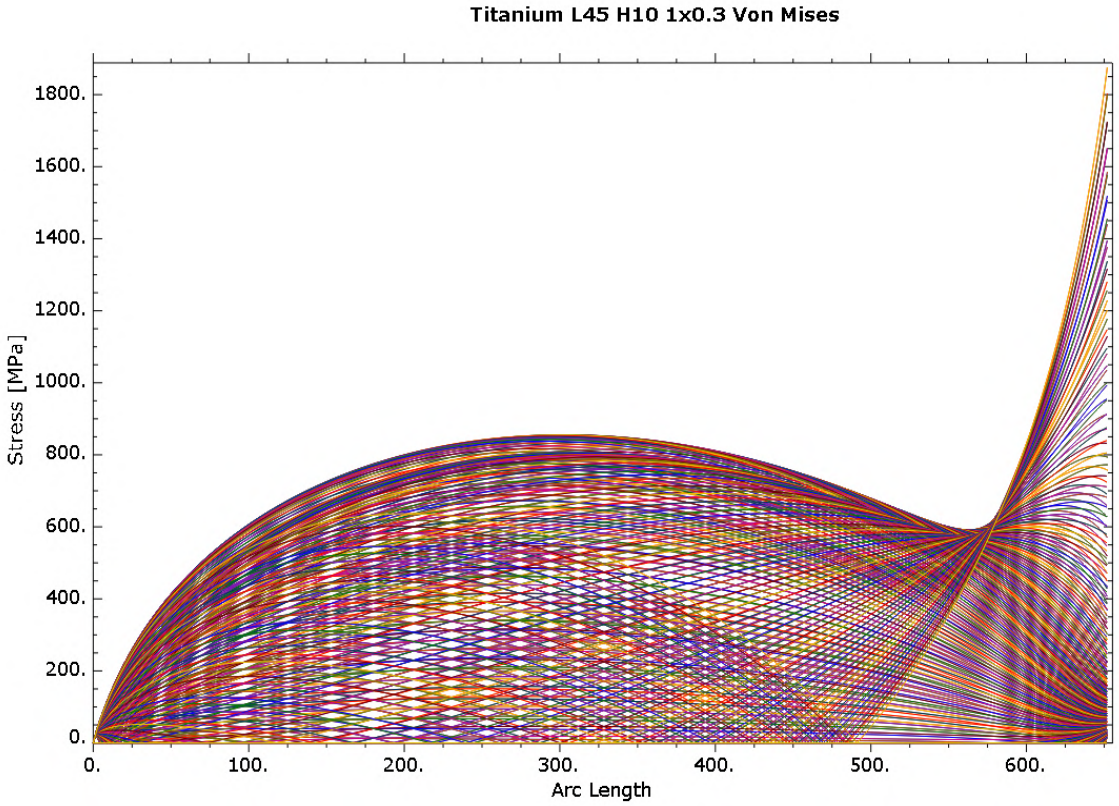

Titanium L42.5 H8.75 1x0.3
[x 1.e3]
2.0
1.5
1.0
0.5
0.0
Stress (MPa)
0.
100.
200.
300.
400.
500.
Arc Length

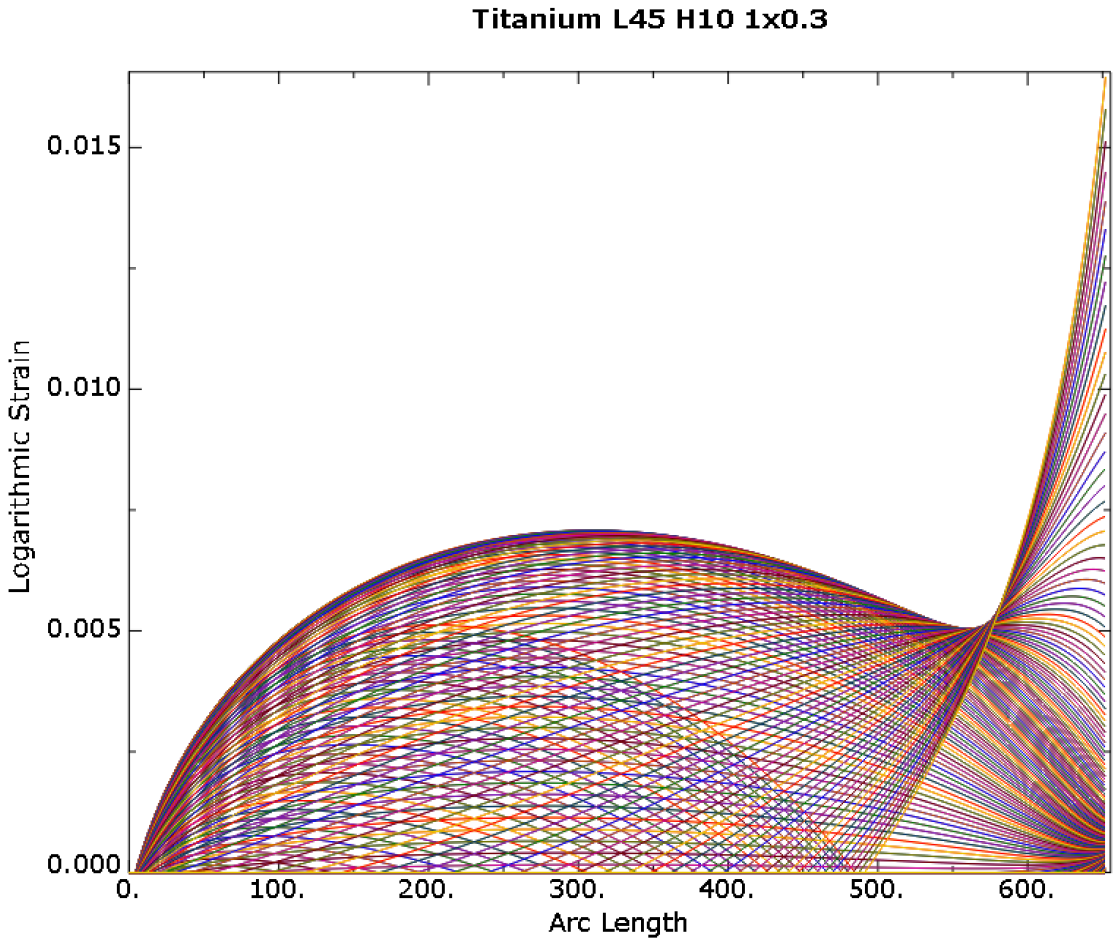

Titanium L42.5 H8.75 1x0.3
0.020
0.015
0.010
0.005
0.000
Logarithmic Strain
0.
100.
200.
300.
400.
500.
Arc Length

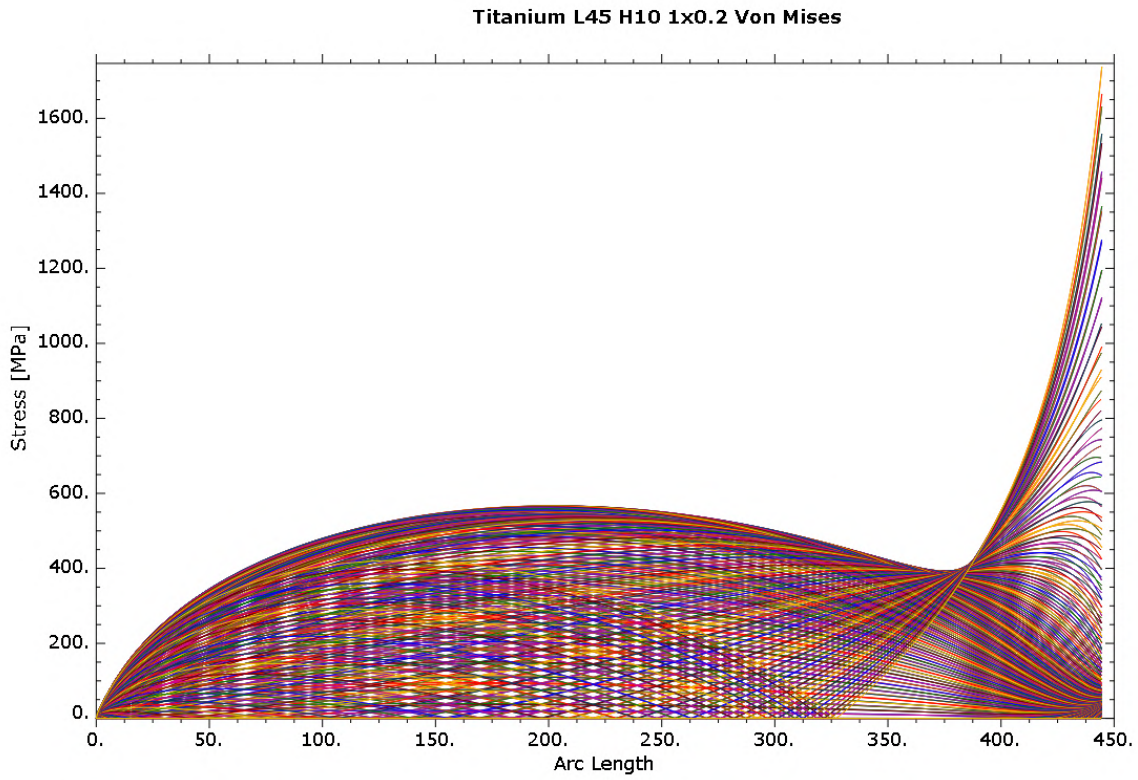
Titanium, Ti6Al4V – Long beam

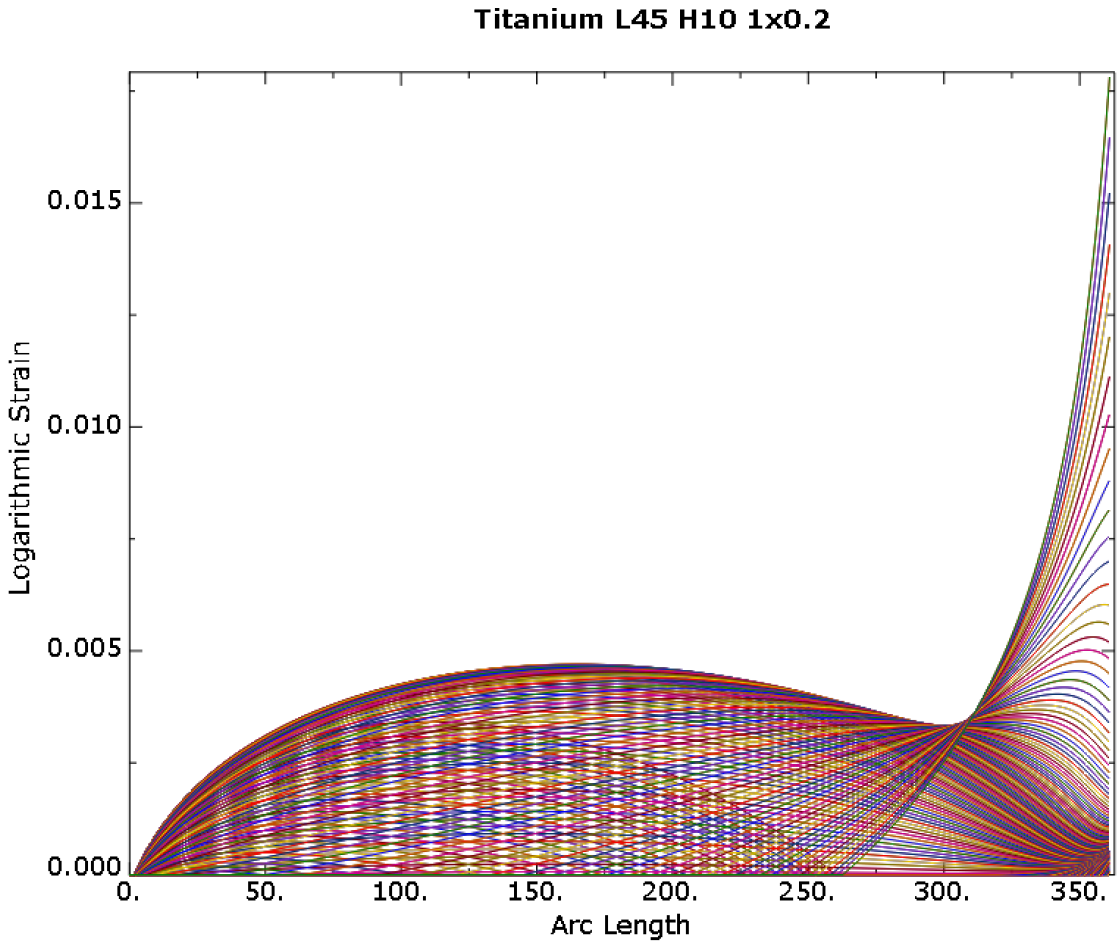


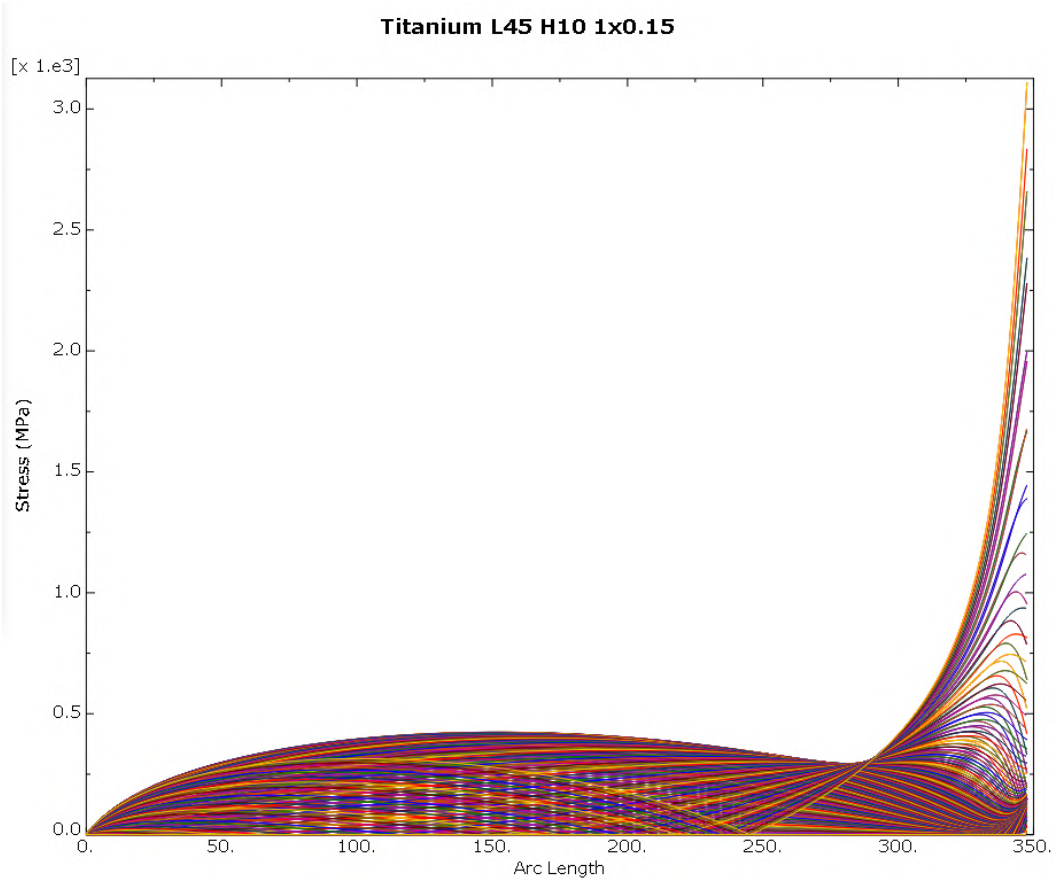


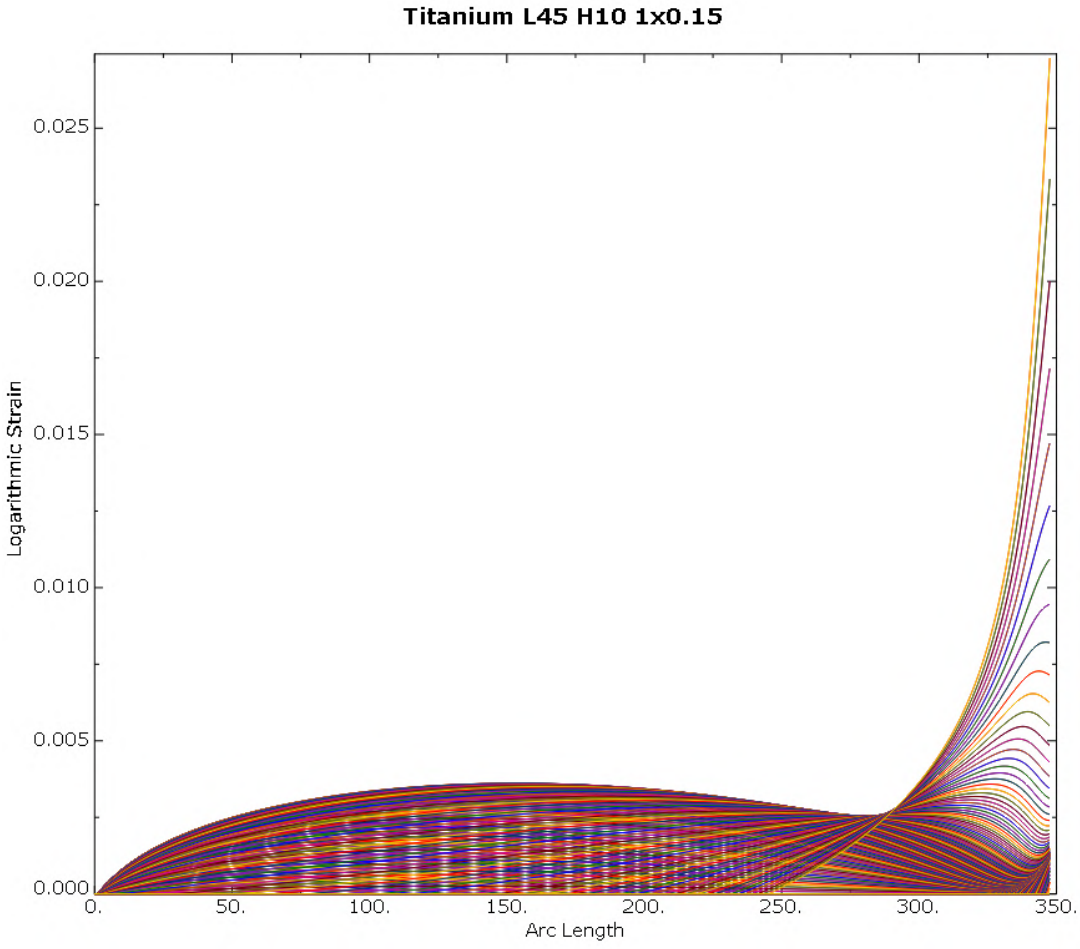

Titanium L45 H10 1x0.3 Von Mises
Stress [MPa]
1800.
1600.
1400.
1200.
1000.
800.
600.
400.
200.
0.
0.
100.
200.
300.
400.
500.
600.
Arc Length

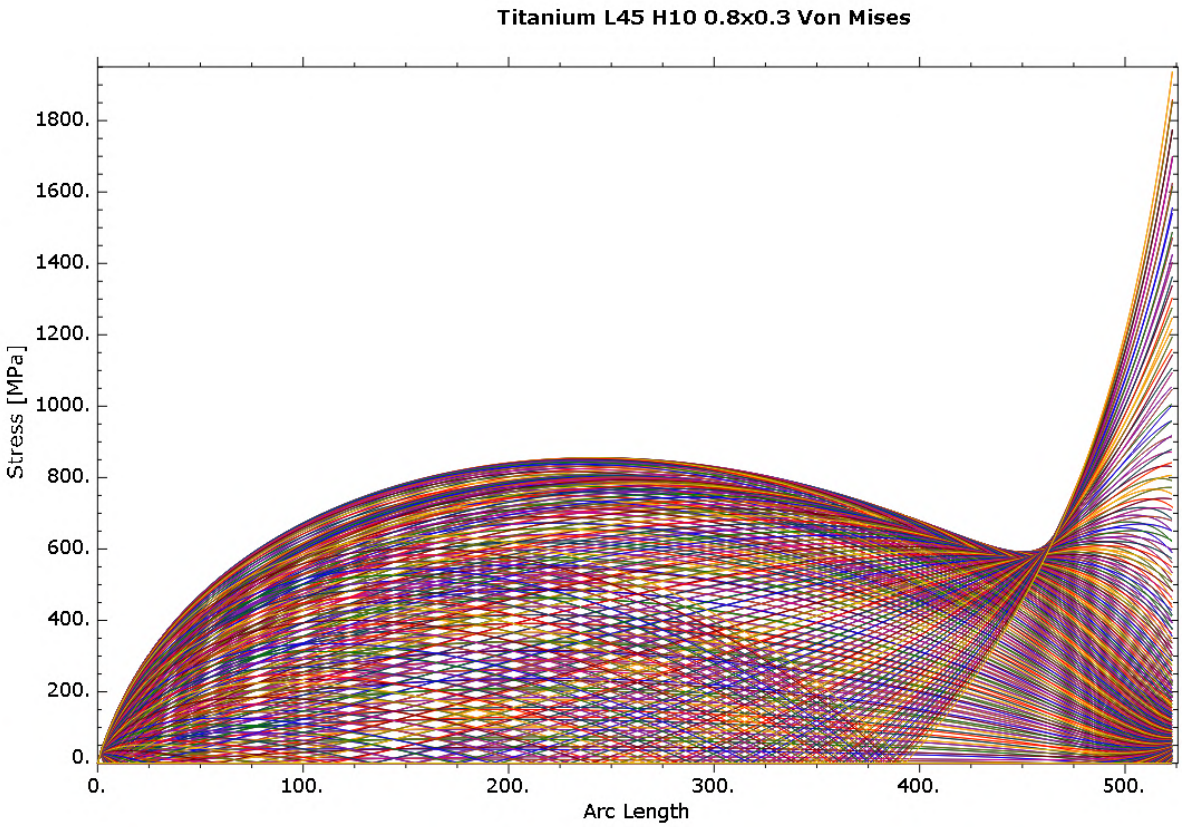

Titanium L45 H10 1x0.3
Logarithmic Strain
0.015
0.010
0.005
0.000
0.
100.
200.
300.
400.
500.
600.
Arc Length

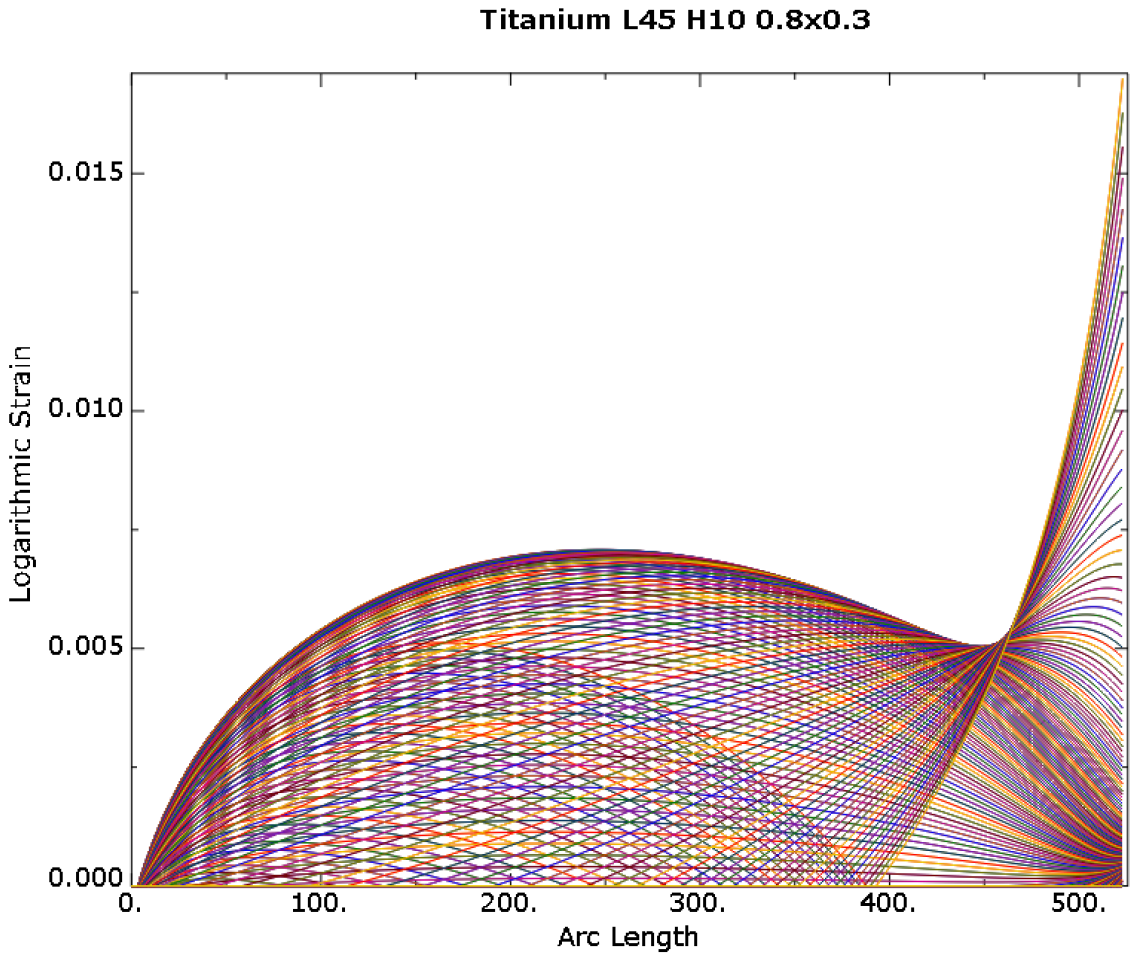

Titanium L45 H10 1x0.2 Von Mises
Stress [MPa]
1600.
1400.
1200.
1000.
800.
600.
400.
200.
0.
0.
50.
100.
150.
200.
250.
300.
350.
400.
450.
Arc Length

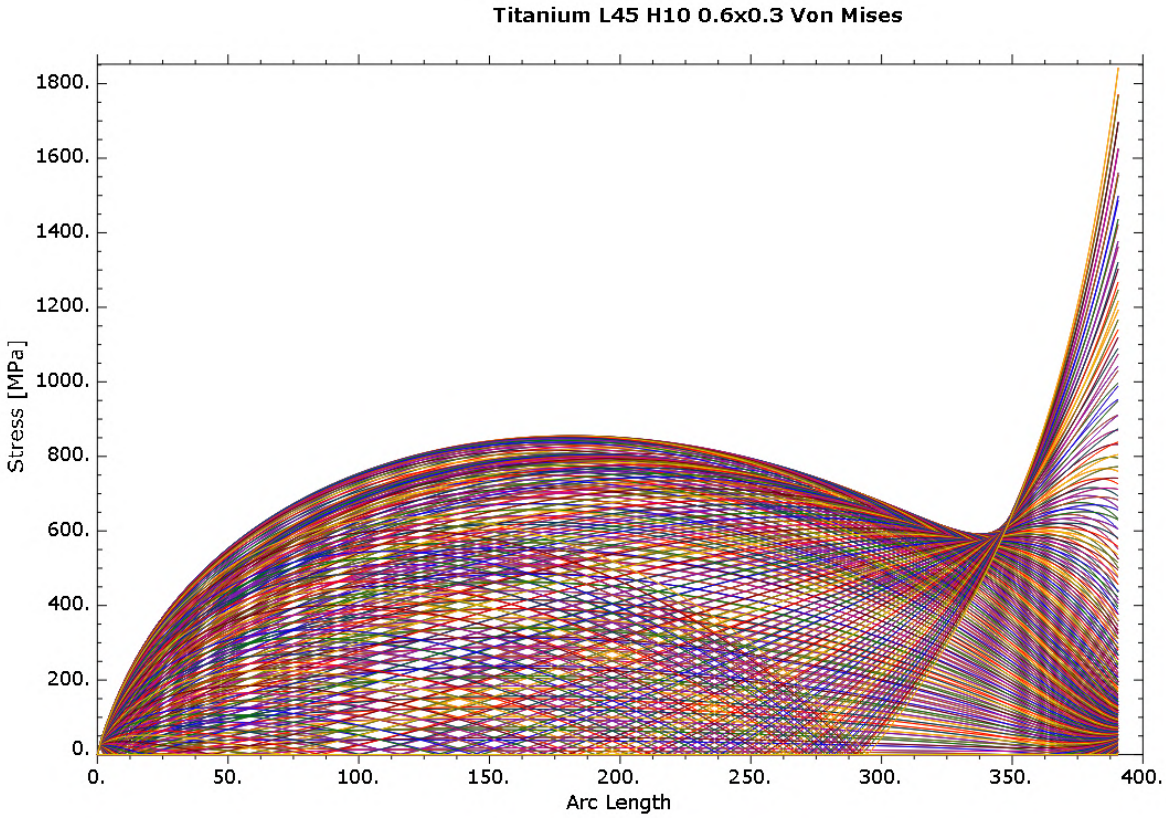

Titanium L45 H10 1x0.2
Logarithmic Strain
0.015
0.010
0.005
0.000
0.
50.
100.
150.
200.
250.
300.
350.
Arc Length

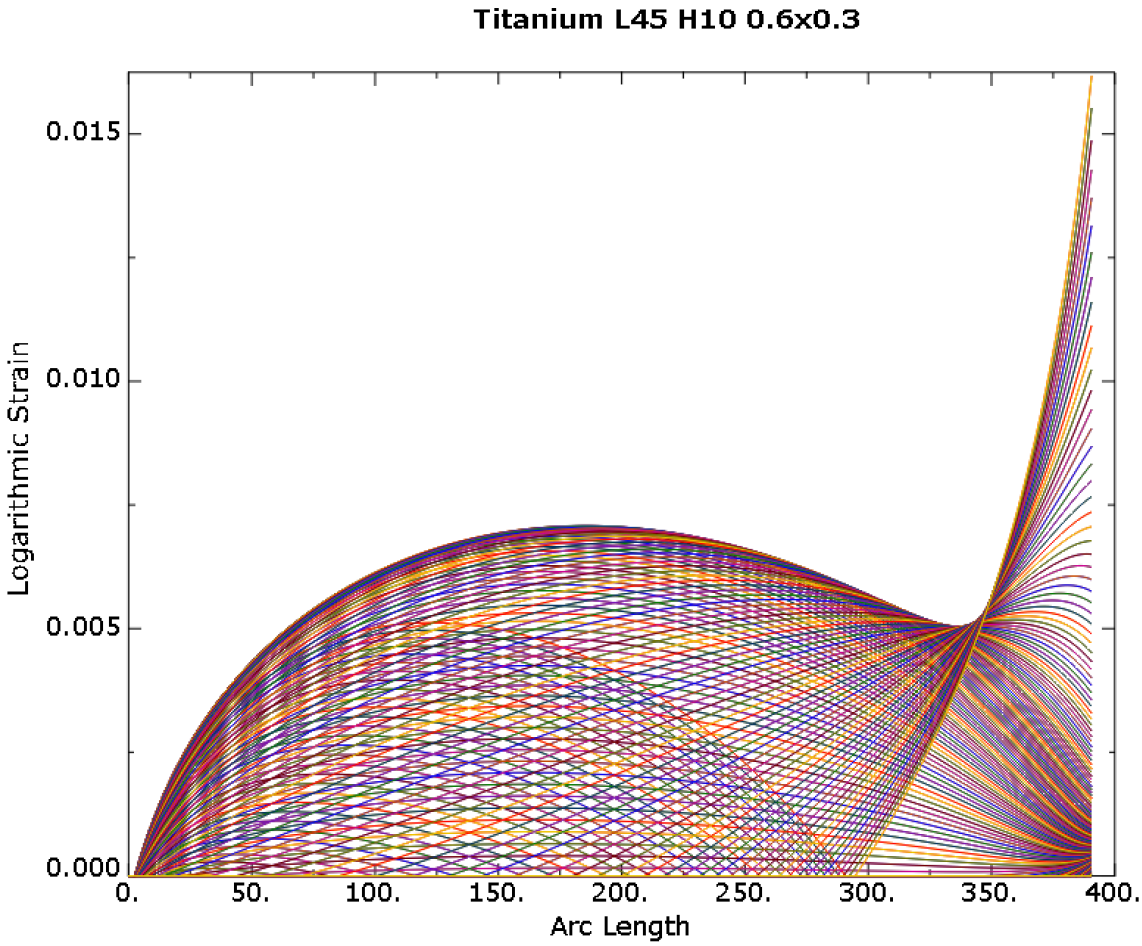

Titanium L45 H10 1x0.15
[x 1.e3]
3.0
2.5
2.0
1.5
1.0
0.5
0.0
Stress (MPa)
0.
50.
100.
150.
200.
250.
300.
350.
Arc Length


Titanium L45 H10 1x0.15
0.025
0.020
0.015
0.010
0.005
0.000
Logarithmic Strain
0.
50.
100.
150.
200.
250.
300.
350.
Arc Length

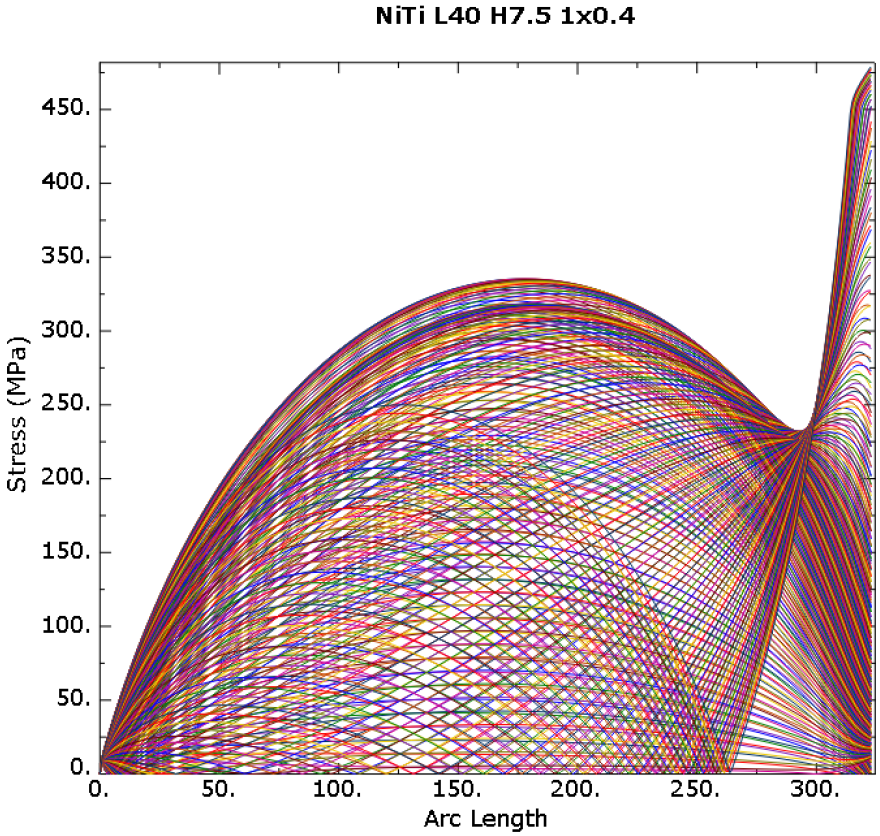

Titanium L45 H10 0.8x0.3 Von Mises
Stress [MPa]
1800.
1600.
1400.
1200.
1000.
800.
600.
400.
200.
0.
0.
100.
200.
300.
400.
500.
Arc Length

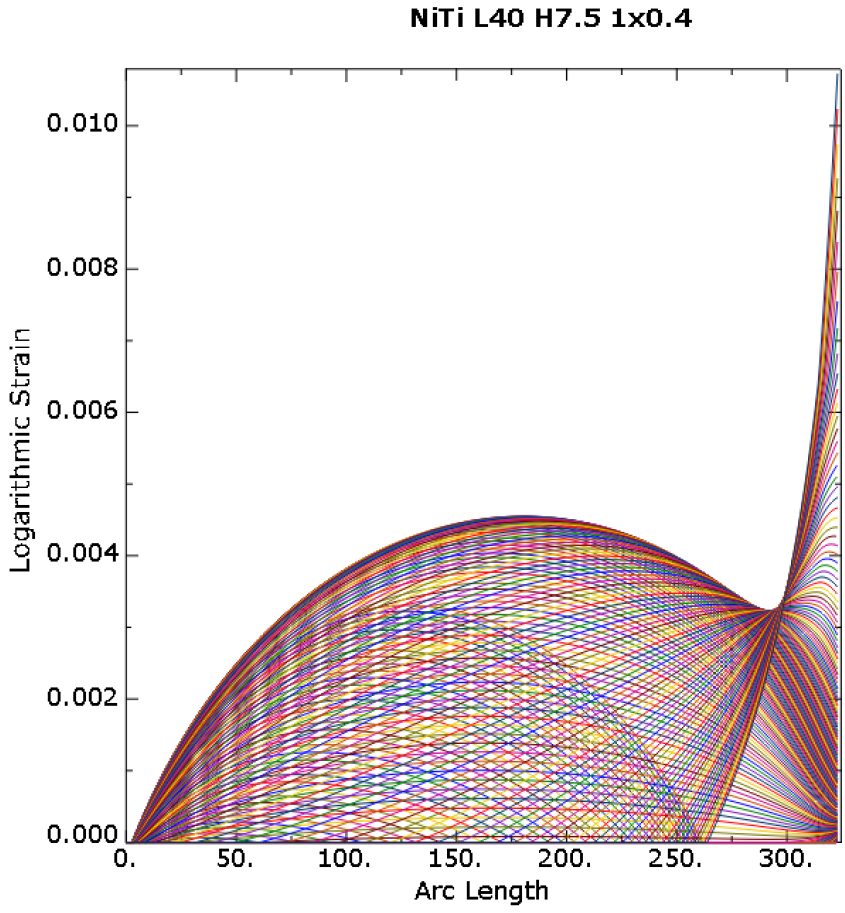

Titanium L45 H10 0.8x0.3
Logarithmic Strain
0.015
0.010
0.005
0.000
0.
100.
200.
300.
400.
500.
Arc Length

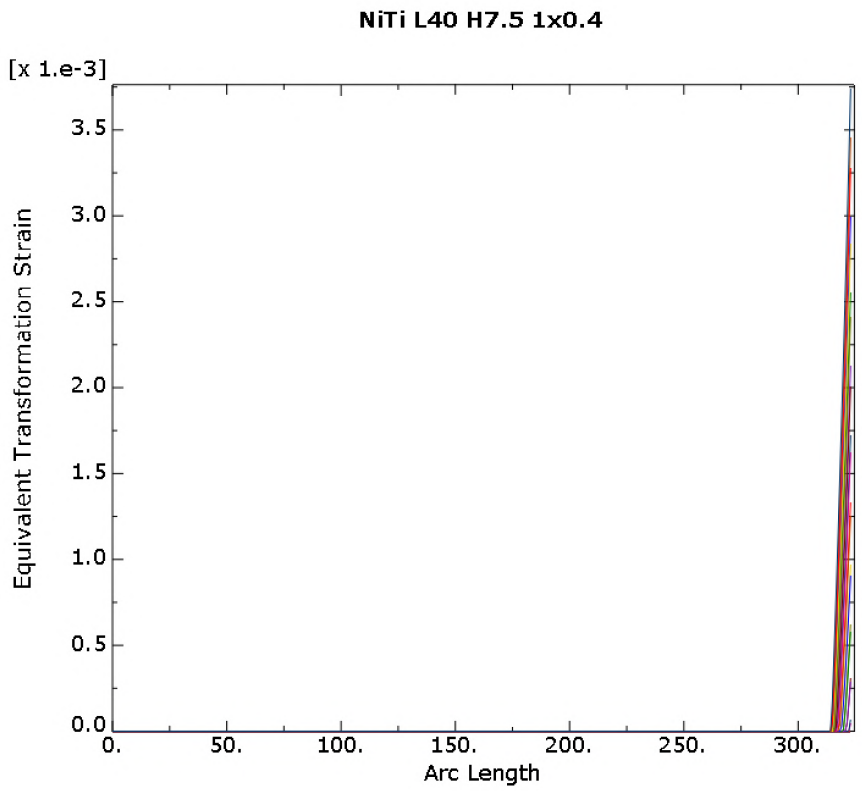

Titanium L45 H10 0.6x0.3 Von Mises
Stress [MPa]
1800.
1600.
1400.
1200.
1000.
800.
600.
400.
200.
0.
0.
50.
100.
150.
200.
250.
300.
350.
400.
Arc Length


Titanium L45 H10 0.6x0.3
Logarithmic Strain
0.015
0.010
0.005
0.000
0.
50.
100.
150.
200.
250.
300.
350.
400.
Arc Length

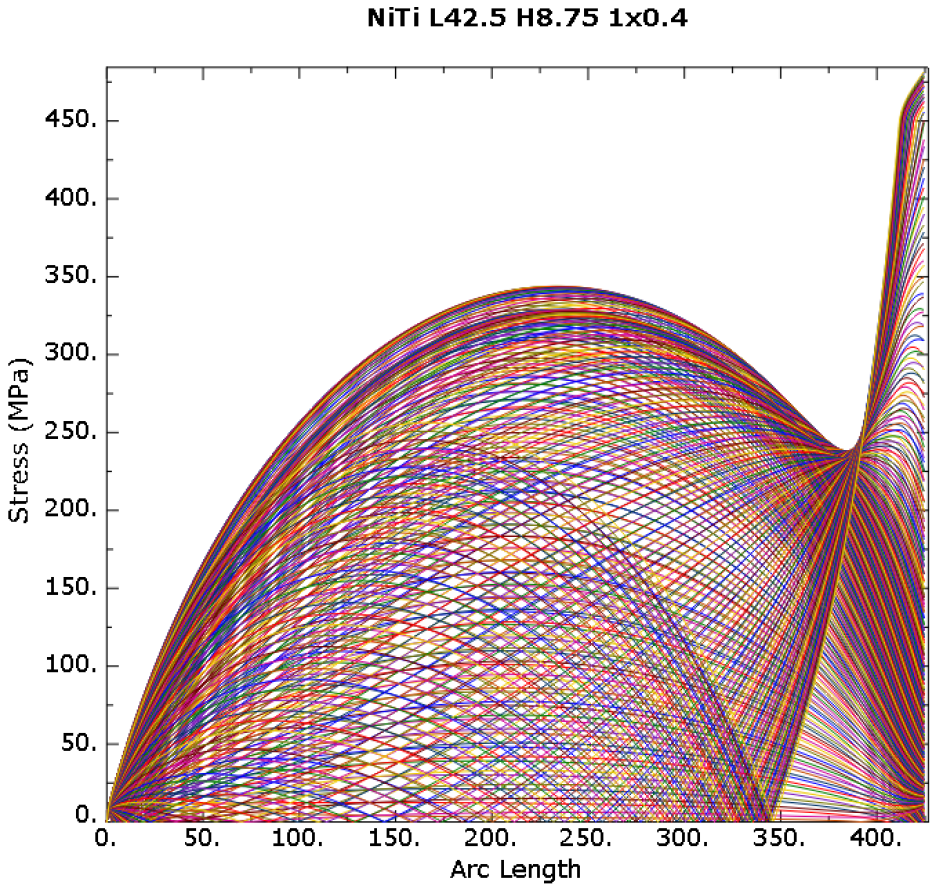
Nickel-titanium, NiTi – Short beam

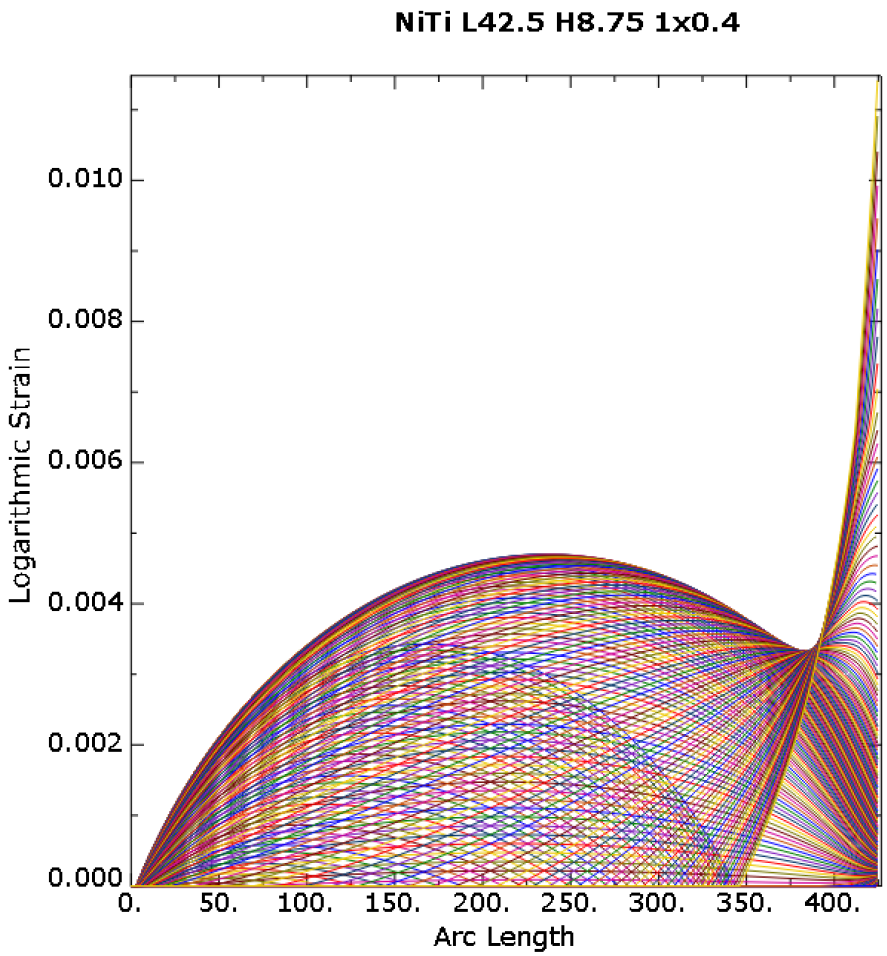


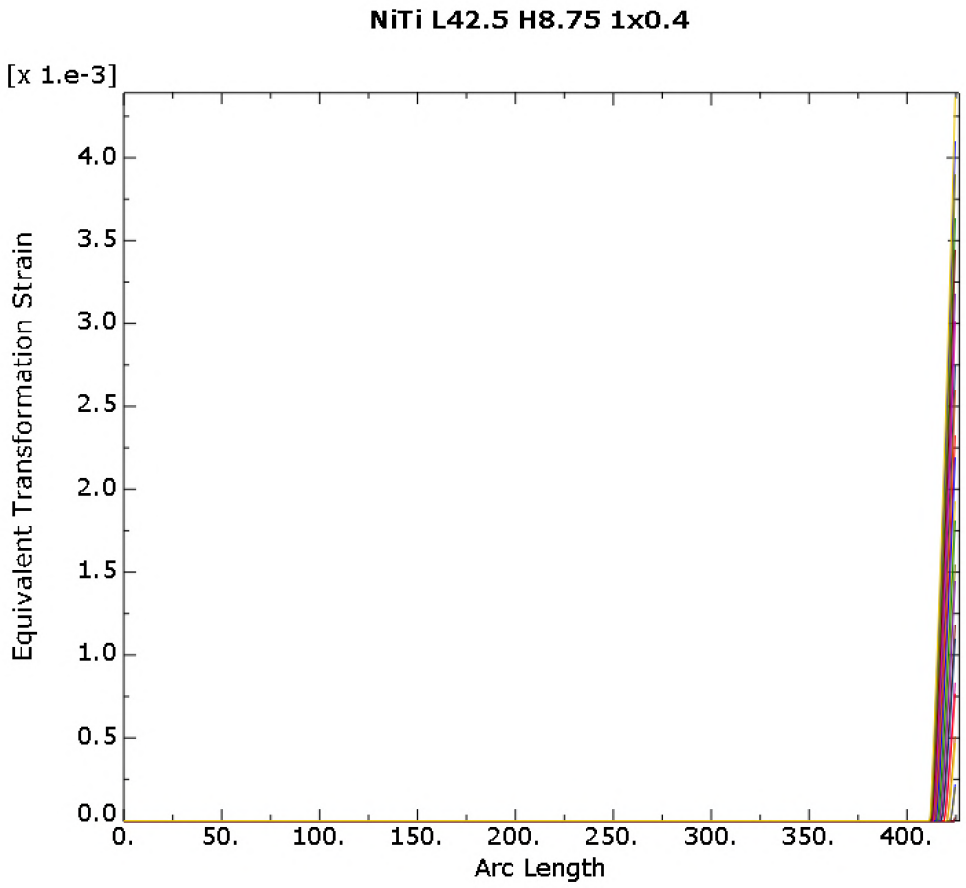


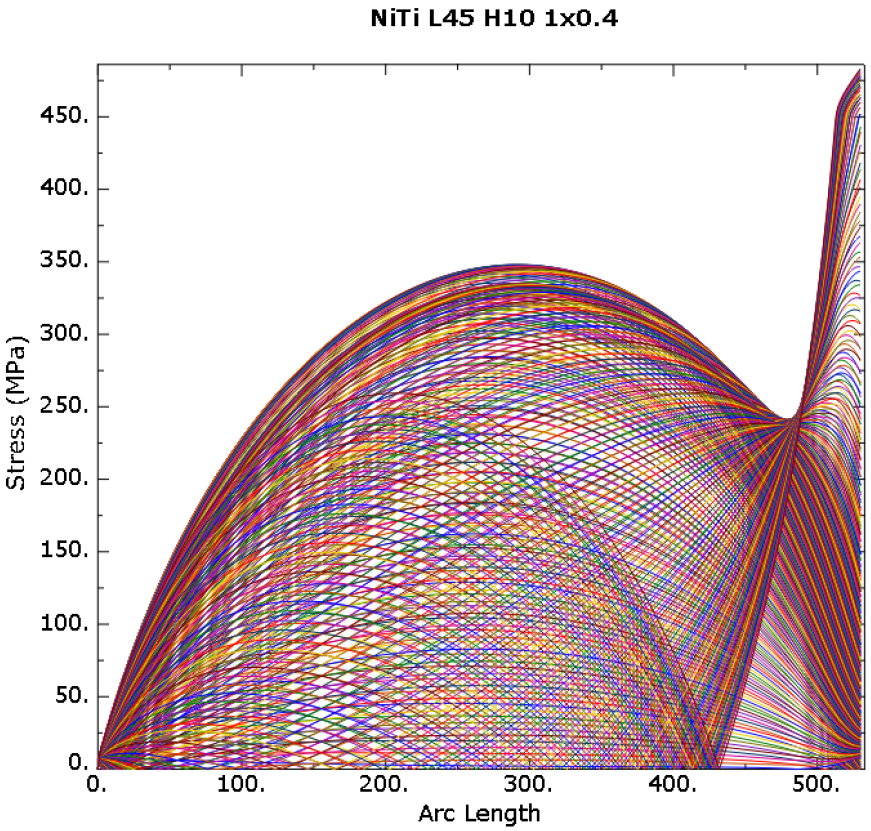


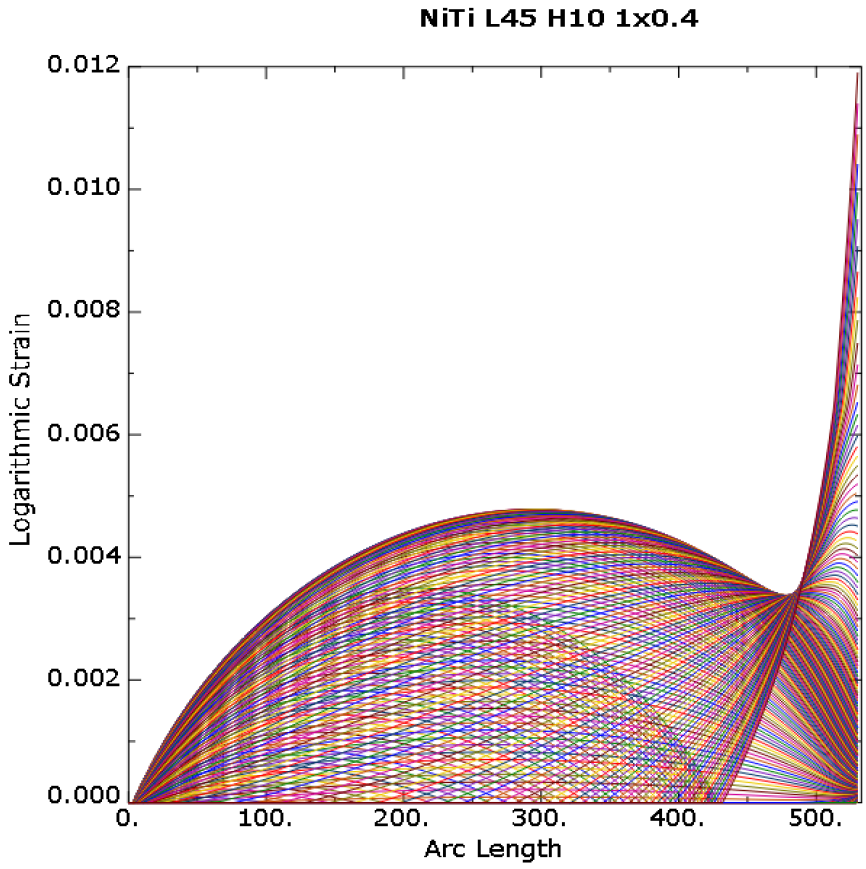
Nickel-titanium, NiTi – Average beam

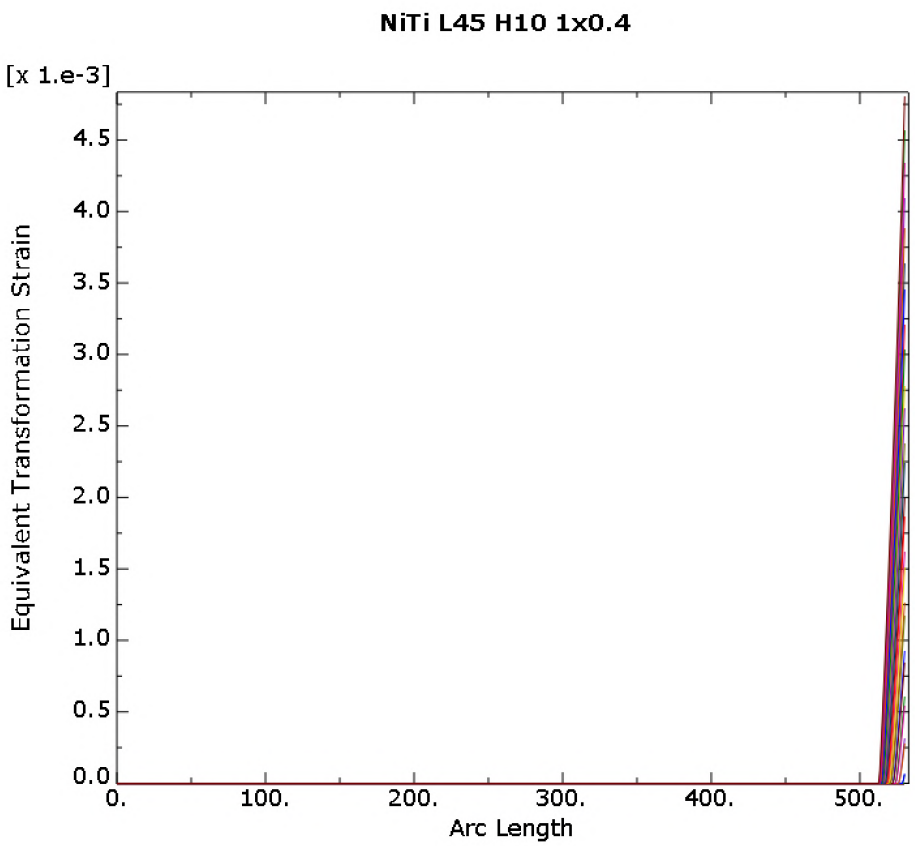



NiTi L42.5 H8.75 1x0.4
Logarithmic Strain
0.010
0.008
0.006
0.004
0.002
0.000
0.
50.
100.
150.
200.
250.
300.
350.
400.
Arc Length

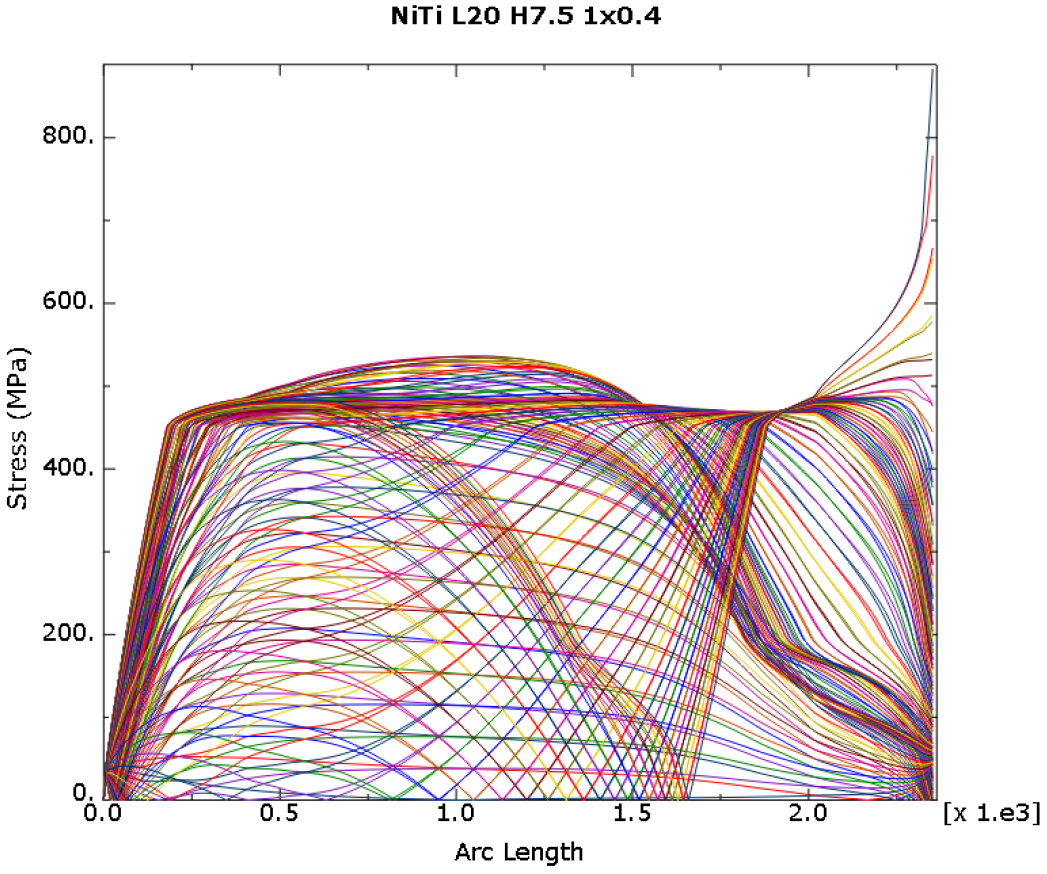

NiTi L42.5 H8.75 1x0.4
[x 1.e-3]
Equivalent Transformation Strain
4.0
3.5
3.0
2.5
2.0
1.5
1.0
0.5
0.0
0.
50.
100.
150.
200.
250.
300.
350.
400.
Arc Length

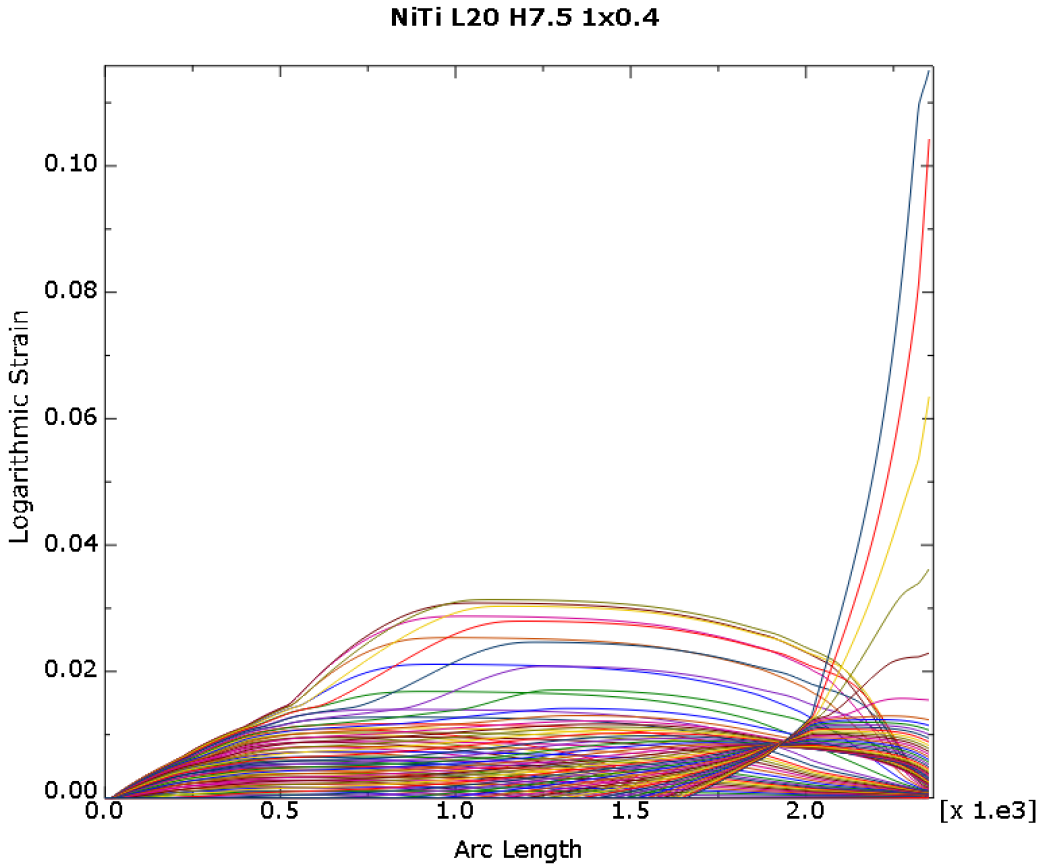

NiTi L45 H10 1x0.4
Stress (MPa)
450.
400.
350.
300.
250.
200.
150.
100.
50.
0.
0.
100.
200.
300.
400.
500.
Arc Length

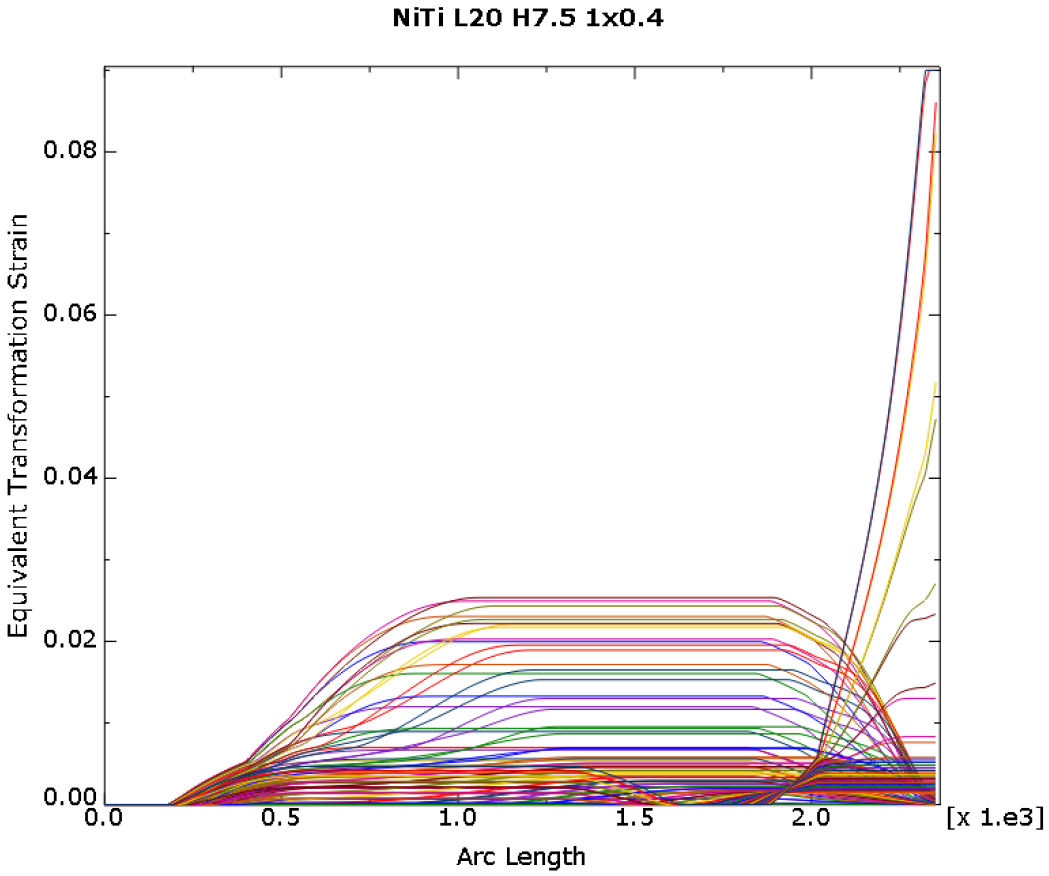

NiTi L45 H10 1x0.4
Logarithmic Strain
0.012
0.010
0.008
0.006
0.004
0.002
0.000
0.
100.
200.
300.
400.
500.
Arc Length



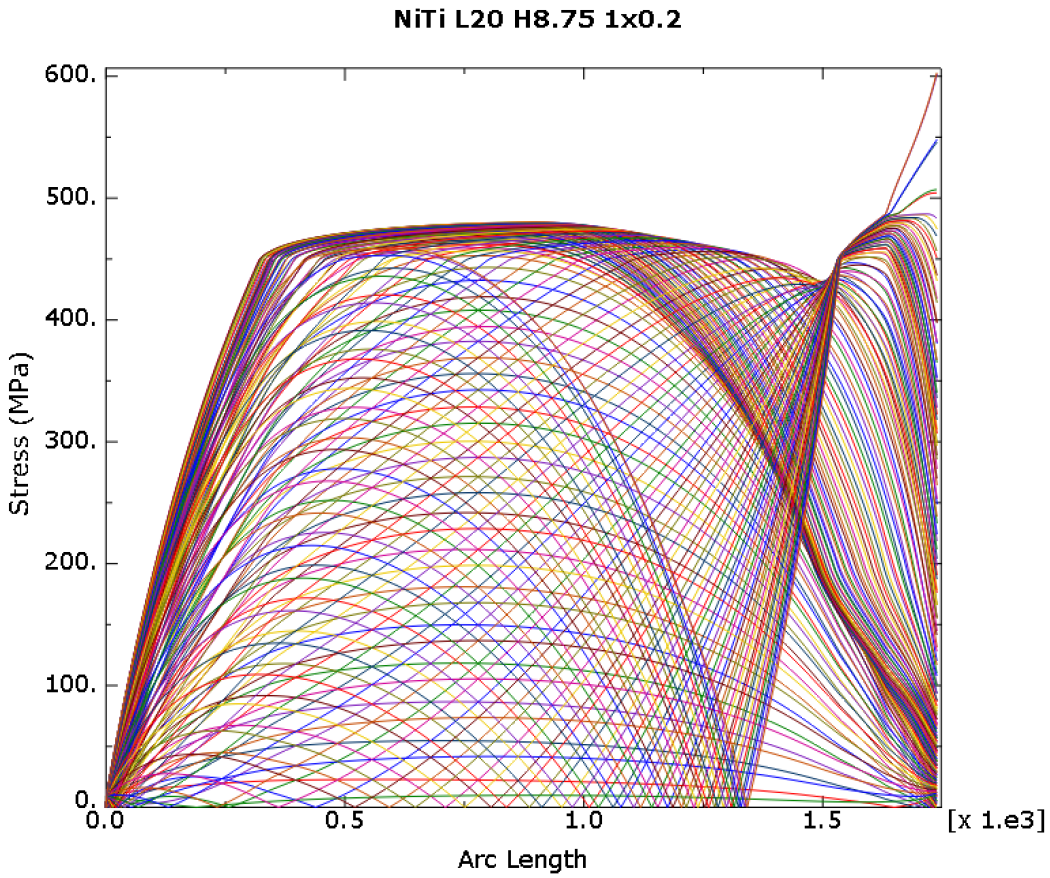
Nickel-titanium, NiTi – Shortest beam (with heigh 7.5)

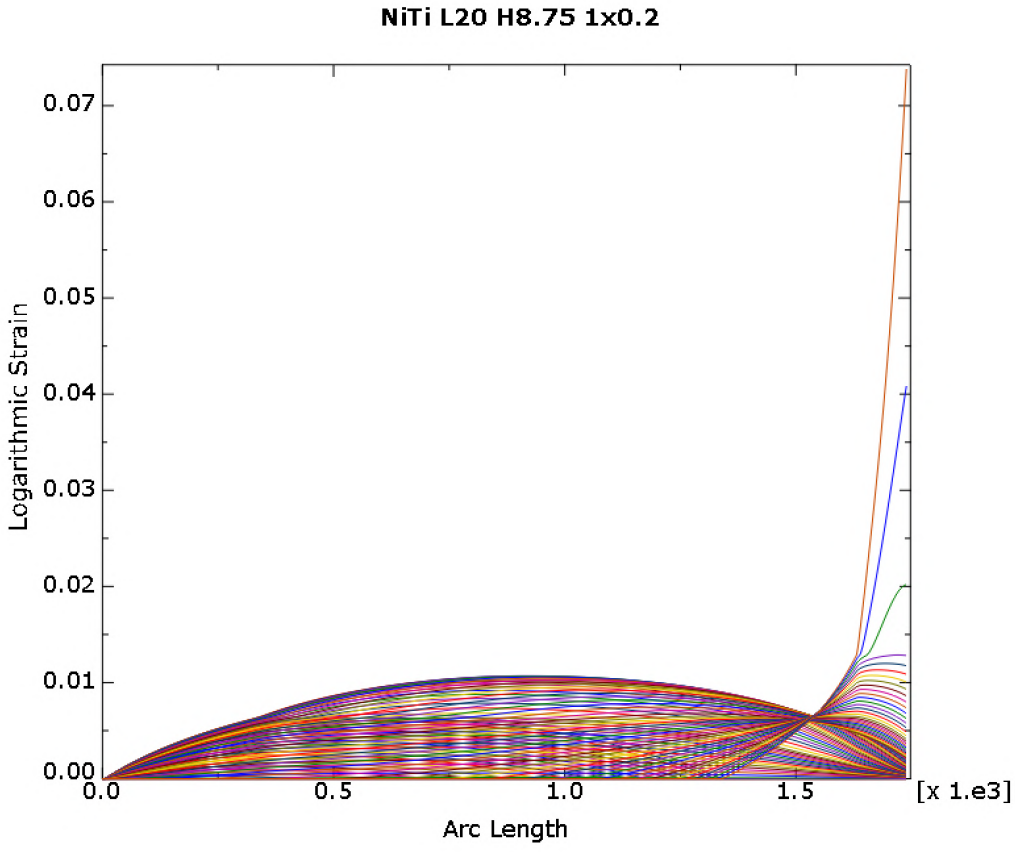


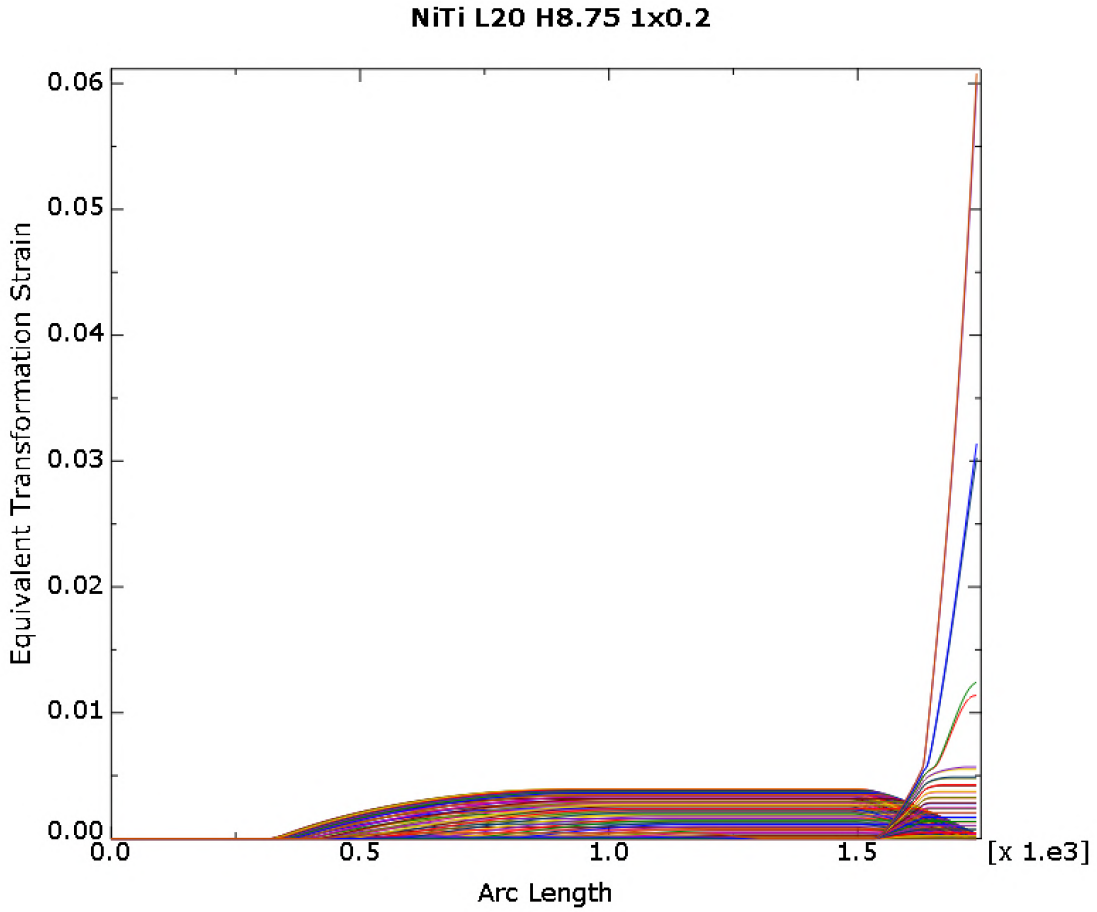

NiTi L20 H7.5 1x0.4
Logarithmic Strain
0.10
0.08
0.06
0.04
0.02
0.00
0.0
0.5
1.0
1.5
2.0
[x 1.e3]
Arc Length


NiTi L20 H7.5 1x0.4
Equivalent Transformation Strain
0.08
0.06
0.04
0.02
0.00
0.0
0.5
1.0
1.5
2.0
[x 1.e3]
Arc Length

Nickel-titanium, NiTi – Shortest beam (with heigh 8.75)







Appendix C – Python spring selection code

~/Desktop/springs.py

```python

def find_valid_spring_configs(L0, Lmin, k, Fmin=0.55, Fmax=2.0, travel=27):
    valid_configs = []

    for L_ext in range(1, 59):      # bush length
        L_con = L_ext - travel
        if L_con <= 0:
            continue

        for N in range(1, 26):     # springs in series

            # Length of single spring
            Ls_ext = L_ext / N
            Ls_con = L_con / N

            # Geometry limits
            if not (Lmin <= Ls_ext <= L0):
                continue
            if not (Lmin <= Ls_con <= L0):
                continue

            # Force
            F_ext = 2 * k * (L0 - Ls_ext)
            F_con = 2 * k * (L0 - Ls_con)

            if F_ext >= Fmin and F_con <= Fmax:
                valid_configs.append({
                    "N_series": N,
                    "L_ext": L_ext,
                    "L_con": L_con,
                    "L_spring_ext": Ls_ext,
                    "L_spring_con": Ls_con,
                    "F_ext": F_ext,
                    "F_con": F_con
                })

    if not valid_configs:
        return [], None, None

    min_force = min(min(c["F_ext"], c["F_con"]) for c in valid_configs)
    max_force = max(max(c["F_ext"], c["F_con"]) for c in valid_configs)

    return valid_configs, min_force, max_force


if __name__ == "__main__":
    L0 = 15   # free length of sigle spring
    Lmin = 6.3   # minimum compressed length
    k = 0.344   # spring constant
```

```
50
51      configs, minF, maxF = find_valid_spring_configs(L0, Lmin, k)
52
53      if configs:
54          print(f"Found {len(configs)} valid configurations")
55          print(f"Force range across all: {minF:.2f} N to {maxF:.2f} N\n")
56          for c in configs:
57              print(
58                  f"N={c['N_series']:2d} | "
59                  f"L_ext={c['L_ext']:2d} | "
60                  f"L_s_ext={c['L_spring_ext']:.2f} | "
61                  f"L_s_con={c['L_spring_con']:.2f} | "
62                  f"F_ext={c['F_ext']:.2f} N | "
63                  f"F_con={c['F_con']:.2f} N"
64              )
65      else:
66          print("No valid configurations found.")
```